TECHNICKÁ UNIVERZITA V LIBERCI

Faculty of Mechatronics, Informatics and Interdisciplinary Studies

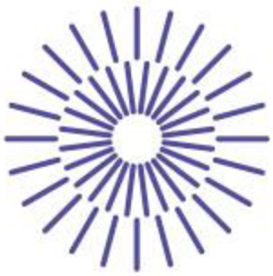

Transcriptomic and physiological response of environmental bacterium and green microalgae to engineered iron nanoparticles

Ph.D. Thesis

Liberec 2023 **Cheryl Soo Yean YEAP**

TECHNICKÁ UNIVERZITA V LIBERCI

Disertační práce

Transcriptomic and physiological response of environmental bacterium and green microalgae to engineered iron nanoparticles

Studijní program: P3942 Nanotechnologie
Studijní obor: Nanotechnologie

Autor práce: **Cheryl Soo Yean Yeap**
Školitel práce: RNDr. Alena Ševců, Ph.D.
Katedra biologie

Liberec 2023

Prohlášení

Prohlašuji, že svou disertační práci jsem vypracovala samostatně jako původní dílo s použitím uvedené literatury a na základě konzultací s vedoucím mé disertační práce a konzultantem.

Jsem si vědoma toho, že na mou disertační práci se plně vztahuje zákon č. 121/2000 Sb., o právu autorském, zejména § 60 – školní dílo.

Beru na vědomí, že Technická univerzita v Liberci nezasahuje do mých autorských práv užitím mé disertační práce pro vnitřní potřebu Technické univerzity v Liberci.

Užiji-li disertační práci nebo poskytnu-li licenci k jejímu využití, jsem si vědoma povinnosti informovat o této skutečnosti Technickou univerzitu v Liberci; v tomto případě má Technická univerzita v Liberci právo ode mne požadovat úhradu nákladů, které vynaložila na vytvoření díla, až do jejich skutečné výše.

Současně čestně prohlašuji, že text elektronické podoby práce vložený do IS/STAG se shoduje s textem tištěné podoby práce.

Beru na vědomí, že má disertační práce bude zveřejněna Technickou univerzitou v Liberci v souladu s § 47b zákona č. 111/1998 Sb., o vysokých školách a o změně a doplnění dalších zákonů (zákon o vysokých školách), ve znění pozdějších předpisů.

Jsem si vědoma následků, které podle zákona o vysokých školách mohou vyplývat z porušení tohoto prohlášení.

20. dubna 2023 Cheryl Soo Yean Yeap

Declaration

I hereby certify, I, myself, have written my dissertation as an original and primary work using the literature listed below and consulting it with my thesis supervisor. I acknowledge that my dissertation is fully governed by Act No. 121/2000 Coll., the Copyright Act, in particular Article 60 – School Work. I acknowledge that the Technical University of Liberec does not infringe my copyrights by using my dissertation for internal purposes of the Technical University of Liberec. I am aware of my obligation to inform the Technical University of Liberec on having used or granted license to use the results of my dissertation; in such a case the Technical University of Liberec may require reimbursement of the costs incurred for creating the result up to their actual amount. At the same time, I honestly declare that the text of the printed version of my dissertation is identical with the text of the electronic version uploaded into the IS STAG. I acknowledge that the Technical University of Liberec will make my dissertation public in accordance with paragraph 47b of Act No. 111/1998 Coll., on Higher Education Institutions and on Amendment to Other Acts (the Higher Education Act), as amended. I am aware of the consequences which may under the Higher Education Act result from a breach of this declaration.

20.4.2023 Mgr. Cheryl Soo Yean YEAP

Acknowledgement

I am are overwhelmed in all humbleness and gratefulness to acknowledge my depth to all those who have helped me to put these ideas, well above the level of simplicity and into something concrete. I cannot express enough thanks to my advisors Alena Sevcu, Nhung Nguyen, Olga Blifernez-Klassen, Victor Klassen, ChinChin Too, Jan Mussgnug, Tobias Busche, Daniel Wibberg, Jakub Riha, Franktisek Eichler, PeiSheng Liew, TzeHao Tan, Wachira Chaiworn, Duy Ngo, Benchaporn Lertanantawong, SuYin Lee, Prof. Miroslav Černík, and Prof. Olaf Kruse, for their continuous support, and I sincerely appreciate for the learning opportunities provided from institutes throughout my study and research.

Any attempt at any level can't be satisfactorily completed without the support of my parents, my dad, brother, sisters, and friends, Sue Fizell, Ana Cassuriaga, Deepali Dhruvanshi, Eva Skoura, Hadi Taghavian. Despite of their busy schedules, they are always supporting me and guiding me every difficult step for educating me and preparing me for my future. Thank you

5 years and 3 months, I have been living together with different flat-mates in total over 21 nationalities. They are wonderful people, each with unique culture from East to West which I will always value after my Ph.D. journey. We often said, Ph.D. made "permanent head down", and yes it obviously made me, and I would rather say, it is a goal should scare you a little and excite you A LOT.

Děkuji!
Danke!
Thank you!
Merci!
Grazie!
Gracias!

Research funding

My research was supported by the following projects:

a) Environmental fate, behavior and biological effects of engineered nanomaterials (PURE-20198003) by the Technical University of Liberec
b) German Academic Exchange Service short term grants DAAD, 2019 (57440917).
c) Research Infrastructures NanoEnviCz (Project No. LM2018124) supported by the MŠMT of the Czech Republic.

Thesis structure

The thesis is partly based on three scientific publications and one that will be submitted on this topic:

a) Yeap et al., 2022: Dissolved iron released from nanoscale zero-valent iron (nZVI) activates the defense system in bacterium *Pseudomonas putida*, leading to high tolerance to oxidative stress (DOI: 10.1016/j.jhazmat.2022.129627), (sections **4.1** – **4.4**)

b) Yeap et al., 2021: RNA extraction from soil bacterium *Pseudomonas putida* and green alga *Raphidocelis subcapitata* after exposure to nanoscale zero valent iron (DOI: https://doi.org/10.37904/nanocon.2020.3764), (sections **4.4.1** and **4.9.1**)

c) Yeap et al., 2022: Phenotypic responses of green alga *Chlamydomonas reinhardtii* after exposure to nanoscale zero valent iron**.** (https://www.confer.cz/nanocon/2022/4614-toxicity-assessment-of-nanoscale-zero-valent-iron-on-chlamydomonas-reinhardtii), (sections **4.10** – **4.12**).

d) Yeap et al: Adaptation of *Raphidocelis subcapitata* to nanoscale zero valent iron (nZVI): The DNA damage repair as sentinel response (sections **4.5**–**4.9**) to be submitted.

Abstract

Nanoscale zero-valent iron (nZVI) has increasingly been applied to remediate aquifers polluted by organochlorines or heavy metals and was also suggested for the elimination of harmful cyanobacterial blooms. As a result, microorganisms in the vicinity of the remediation can be stressed by the surplus of iron released from nZVI. To date, the toxicity of iron nanoparticles (NPs) has been evaluated on numerous microorganisms. Although different endpoints were measured, the regulation of gene expression related to iron stress defense pathways have not been described sufficiently.

This thesis, therefore, aimed to compare the biological effect of different forms of iron including reactive nZVI, non-reactive nFe_3O_4, and dissolved iron obtained from nZVI suspension on an environmental bacterium, and two green microalgae. *Pseudomonas putida* NCTC 10936 was exposed to 100 mg/L of nZVI, and 44.5 µg/L of iron released from 100 mg/L of nZVI. Green microalgae, *Raphidocelis subcapitata* ATCC 22662, and *Chlamydomonas reinhardtii* wild type CC-5325 were exposed to 100 mg/L of either nZVI or nFe_3O_4. The physiological endpoints (cell morphology and viability, photosynthetic activity, phytochrome content) provided a baseline of stress levels before transcriptomic studies were performed. The transcriptomic analysis required optimization of RNA extraction protocols that was challenging due to the presence of reactive nZVI and high polysaccharide content in microalgae. Sufficient RNA integrity was finally reached and transcriptomic analysis of *P. putida* was performed after 6 h and 24 h-exposure and *R. subcapitata* after 1 h and 4 h-exposure to iron NPs.

In the *P. putida* study, cell viability was neither affected by nZVI nor dissolved iron, although the dissolved iron caused stress that altered the cell physiology and caused the generation of smaller cells, whereas cells were elongated in the presence of nZVI. The transcriptomic analysis confirmed the observed stronger physiological effect caused by dissolved iron (in total 3839 differentially expressed genes [DEGs]) than by nZVI (945 DEGs). Dissolved iron (but not nZVI) activated genes involved

in oxidative stress-related pathways, antioxidant activity, carbohydrate, and energy metabolism, but downregulated genes associated with flagellar assembly proteins and two-component systems involved in sensing external stimuli. As a result, bacteria very effectively faced oxidative insults, and cell viability was not affected.

In the microalgae study, nZVI and nFe_3O_4 affected differently *R. subcapitata* and *C. reinhardtii*. *C. reinhardtii* displayed more decreased viability, as well as lower non-photochemical quenching (NPQ) than *R. subcapitata* upon the NPs exposure. NPs attachment on both microalgae was observed after 1 h which might later result in deformed cell morphology or leakage of cytosol in about 15% of *R. subcapitata* and 20–30% of *C. reinhardtii* cells within the first 24 h. Under a darker environment containing nFe_3O_4 and nZVI, the NPQ was lower (30% lower comparing to control after 1h) which corresponds to a decrease in gene expression related to energy transportation that was probably needed to increase photosynthesis efficiency. nZVI exposure triggered a more pronounced transcriptomic response than nFe_3O_4 in *R. subcapitata* after 1 h including DNA repair response, while such response diminished quickly later at 4 h indicating a fast adaptive response to stress insults. However, the inhibition effect was only temporary, *R. subcapitata* was able to recover thereafter due to a surplus of CO_2, generation of new cells, and oxidation of nZVI which then became less harmful.

Furthermore, oxidative stress-induced repair is often a multi-tiered process and energetically costly. Carbohydrate-energy metabolism was shown to be well regulated at different time points in *P. putida* and *R. subcapitata*, indicating their energy transferring in different stress phases and their robust ability to adapt to environmental stress.

Keywords: Zero-valent iron nanoparticles, magnetite nanoparticles, dissolved iron, toxicity, oxidative stress, bacteria, green algae, transcriptome, DNA damage and repair, carbohydrate metabolism, defense mechanism

Abstrakt

Nanočástice nulamocného železa (nZVI) se mohou využívat například k sanaci území znečištěných chlorovanými organickými sloučeninami nebo těžkými kovy a také na likvidaci sinicového vodního květu. Při sanačním zásahu jsou mikroorganizmy vystaveny vyšším koncentracím železa uvolněného z nZVI. Toxicita nanočástic železa byla hodnocena na mnohých mikroorganizmech, nicméně regulace exprese genů souvisejících s obrannými mechanizmy dosud úplně prostudována nebyla.

Cílem této práce proto bylo porovnat biologický účinek různých forem železa, včetně reaktivního nZVI, nereaktivního nFe_3O_4 a rozpuštěného železa získaného ze suspenze nZVI na bakterie a zelené řasy. *Pseudomonas putida* NCTC 10936 byla vystavena 100 mg/l nZVI a 44,5 µg/l železa uvolněného ze 100 mg/l nZVI. Zelené řasy, *Raphidocelis subcapitata* ATCC 22662 a *Chlamydomonas reinhardtii* CC-5325 byly vystaveny 100 mg/l buď nZVI nebo nFe_3O_4. Fyziologické parametry (morfologie a životaschopnost buněk, fotosyntetická aktivita, obsah fytochromů) poskytly výchozí hodnoty stresových hladin před provedením transkriptomických analýz. Transkriptomická analýza vyžadovala optimalizaci protokolu pro izolaci RNA, což bylo náročné kvůli přítomnosti reaktivního nZVI a vysokého obsahu polysacharidů v řasách. Po dosažení dostatečné kvality izolované RNA byla provedena analýza transkriptomu *P. putida* po 6 a 24-hodinové expozici a *R. subcapitata* po 1 h a 4-hodinové expozici nanočásticím.

Ve studii *P. putida* nebyla životaschopnost buněk ovlivněna ani nZVI, ani rozpuštěným železem, ačkoli rozpuštěné železo způsobovalo stres, který se projevoval tvorbou menších buněk, zatímco buňky byly naopak v přítomnosti nZVI prodloužené. Transkriptomická analýza potvrdila pozorovaný větší fyziologický účinek způsobený rozpuštěným železem (celkem 3839 rozdílně exprimovaných genů [DEG]) v porovnání s nZVI (945 DEG). Rozpuštěné železo (nikoli však nZVI) aktivovalo geny, které se podílejí na odpovědi na oxidační stres, antioxidační aktivitě, energetickém metabolizmu, na regulaci růstu bičíků a systémy podílejícími

se na vnímání vnějších podnětů. V důsledku toho bakterie velmi účinně čelily oxidačnímu stresu a životaschopnost buněk nebyla ovlivněna.

R. subcapitata a *C. reinhardtii* byly různě ovlivněné nZVI a nFe_3O_4. U *C. reinhardtii* došlo k snížení životaschopnosti buněk a také vykazovala nižší hodnoty nefotochemického zhášení (non-photochemical quenching, NPQ) než *R. subcapitata*. Na obou řasách byla pozorována adsorpce nanočástic po 1 hodině, což později mohlo mít za následek deformaci buněk nebo únik cytosolu u přibližně 15 % buněk *R. subcapitata* a 20–30 % buněk *C. reinhardtii* během prvních 24 hodin. V tmavším prostředí obsahujícím nFe_3O_4 a nZVI byla hodnota NPQ nižší (o 30 % ve srovnání s kontrolou po 1 h), což by mohlo odpovídat poklesu exprese genů souvisejících s transportem energie, která byla pravděpodobně využitá pro zvýšení účinnosti fotosyntézy. nZVI vyvolalo výraznější odpověď na úrovni exprese genů než nFe_3O_4 v *R. subcapitata* po 1 h, přičemž se exprese genů po 4 h rychle snížila, což naznačuje rychlou adaptivní reakci na oxidační stres. Účinek nZVI byl tedy pouze dočasný, kultura *R. subcapitata* se dokázala rychle zotavit díky nadbytku CO_2, tvorbě nových buněk a oxidaci nZVI, které se poté stalo méně škodlivým.

Obrana buněk vyvolaná oxidačním stresem je často vícestupňovým a tudíž energeticky nákladným procesem. Bylo prokázáno, že metabolizmus sacharidů a energetický metabolizmus je u *P. putida* a *R. subcapitata* dobře regulován v různých fázích stresu a přispívá k jejich vynikající schopnosti přizpůsobit se podmínkám v prostředí.

Klíčová slova: nanočástice nulamocného železa, nanočástice magnetitu, rozpuštěné železo, toxicita, oxidační stres, bakterie, zelené řasy, transkriptom, poškození a oprava DNA, metabolizmus sacharidů, obranný mechanizmus

Table of Contents

Abbreviations

ANOVA	Analysis of variance
BER	Base excision repair
bp	Base pair
CDC	Cell division cycle
cDNA	Complementary DNA
DCS	Differential centrifugal sedimentation
DNA	Deoxyribonucleic acid
EDS	Energy-dispersive X-ray spectroscopy
EDTA	Ethylene diamine tetra acetic acid
Eh	Reductive potential
HR	Homologous recombination
HSM	High salt Sueoka's medium
Kbp	Kilo base pair
KEGG	Kyoto Encyclopedia of Genes and Genomes
LHC	Light harvesting complex
MCM 2–7	Minichromosome maintenance protein 2–7
MMR	Mismatch repair
MW	Molecular weight
NER	Nucleotide excision repair
NPs	Nanoparticles
nFe_3O_4	Nano iron (II, III) oxide
NPQ	Non-photochemical quenching
nZVI	Nano-scale zero valent iron
OD	Optical density
ORP	Oxidative reduction potential
PCNA	Proliferating cell antigen

PCR	Polymerase chain reaction
PPI	Protein-protein interaction
PS II	Photosystem II
PVC	Polyvinyl chloride
RNA	Ribonucleic acid
RNA-seq	RNA sequencing
ROS	Reactive oxygen species
Rpm	Revolutions per minute
RT-qPCR	Reverse transcription Quantitative PCR
SEM	Scanning electron microscopy
SSA	Specific surface area
STAR	Spliced transcripts alignment to a reference

1. Introduction

Nanoscale zero-valent iron (nZVI) particles are often used to remediate polluted soil or groundwater (Lefevre et al., 2015; Mueller et al., 2012; Tratnyek and Johnson, 2006; Wang et al., 2019), nZVI can reduce certain pollutants such as chlorinated ethenes (Czinnerová et al., 2020; Semerád et al., 2021), heavy metals (Crane et al., 2011; Li et al., 2017; Liang et al., 2021, 2014; Němeček et al., 2015; Yuan et al., 2022), pesticides (El-Temsah et al., 2016), or chlorinated phenols (Long et al., 2020).

The release of nZVI into the environment containing oxygenated water results in the oxidation of nZVI which generates Fe^{2+} (Bae et al., 2018; R. Keenan and L. Sedlak, 2008; Schmid et al., 2014; Semerád et al., 2020). Fe^{2+} can be easily up taken by bacteria and other microorganisms, and if present in higher concentrations, it can cause overproduction of intracellular reactive oxygen species (ROS) leading to oxidative damage of lipids, proteins, and DNA (Auffan et al., 2008; J. Miller et al., 2010; Nel et al., 2006; Rivera-Araya et al., 2019; Rutkowski et al., 2007; Ševců et al., 2011).

The toxicity of nZVI has been evaluated in single bacterial cultures, bacterial communities in freshwater, contaminated groundwater (Crampon et al., 2019; L. Kirschling et al., 2010; Nguyen et al., 2018a), and heavy metal-contaminated soil (Fajardo et al., 2012). These studies indicated that the ecotoxicity of nZVI is dose- and species-dependent and its exposure duration is strongly affected by environmental conditions.

Furthermore, green algae are often used as an ecological indicator of the quality of an aquatic ecosystem. Numerous iron nanoparticles (NPs) such as nano-Fe_3O_4 increased the ROS levels in algal species at concentration of ($\geq$ 50 mg/L), including on *Chlamydomonas reinhardtii* and *Chlorella vulgaris*, which exacerbated the metabolic activity, cell division rate as well as their photosynthetic activity due to shading effect of the iron NPs (Hurtado-Gallego et al., 2020; Xiaoxiao et al., 2012). Furthermore, exposure of nZVI also affected the cell cycle and growth of *Raphidocelis subcapitata*, at concentration of ($\geq$ 0.05 mg/L) accompanied by DNA

damage via intracellular ROS formation (Gonzalo et al., 2014; Keller et al., 2012). The toxicity of nZVI was lower with increasing particle size (Lei et al., 2016).

Besides that, several nanotoxicity studies have also been performed to compare the interplay between the particle effect (nZVI) and ionic effect (Fe^{2+}) (Auffan et al., 2008; Lee et al., 2008; Yeon Kim et al., 2010). A low dose of nZVI (1.2–110 mg/L) showed to inhibit bacterial activities temporarily, as the physical contact of nZVI with microbial cell membranes could lead to cell membrane/wall disruption or increased oxidative stress (Auffan et al., 2008; Diao and Yao, 2009; Lee et al., 2008; Saccà et al., 2014; Yeon Kim et al., 2010). Two studies showed that Fe^{2+} treatment (<0.56 mg/L) in deaerated conditions significantly inactivated *Escherichia coli* within 1 h, suggesting that the inactivation was caused by transmembrane entry of Fe^{2+} into the cytoplasm (Lee et al., 2008; Yeon Kim et al., 2010). The toxicity of nZVI on two *Pseudomonas putida* strains after 1 h of exposure has also been reported, although in an unrealistically high nZVI concentrations (1,000 mg/L) (Chaithawiwat et al., 2016). In general, nZVI toxicity studies on *P. putida* were mostly based on phenotypic responses such as growth rate, cell viability, motility, and oxidative stress (Lv et al., 2017; Ortega-Calvo et al., 2016; Semerád et al., 2020; Shanbhogue et al., 2017).

Microorganisms are capable of regulating adaptive transcriptional responses to even modest ROS concentrations in their cells. Therefore, when exposed to nZVI, bacteria can swiftly activate genes involved in oxidative stress defense (Fajardo et al., 2013; Lefevre et al., 2015; Saccà et al., 2014). For example, *Pseudomonas stutzeri* exposed to 5 g/L of nZVI expressed genes functioning in detoxifying ROS, including catalase (*katB*) and superoxide dismutase (SOD, *sodB*) after 3 h (Saccà et al., 2014), indicating that nZVI increases ROS followed by the cell defense against oxidative stress (Saccà et al., 2014; Semerád et al., 2019). In most cases, studies into nZVI have been largely based on how the ROS production induces oxidative stress at the physiological level (Abdal Dayem et al., 2017) and how it triggers gene expression involving antioxidant activity to confer the toxic effects (Fajardo et al., 2013; Simon et al., 2013; Zheng et al., 2018). Transcriptomic studies on green alga *R. subcapitata* after the exposure to nZVI are scarce and can elucidate more details about cell defense. Exposure of *C. reinhardtii* to 1 mg/L of several metal oxide NPs (titanium oxide, zinc oxide or silver NPs) caused up-regulation of the carbohydrate-glucose metabolic process, redox

homeostasis, transmembrane transporter activity, metal ion binding, and ribosome protein synthesis (Simon et al., 2013). nZVI (100 mg/L) affected cytosolic free ATP ($MgATP^{2-}$) in higher plant, *Arabidopsis thaliana* (Zhang et al., 2018).

To the best of our knowledge, there is no comprehensive study besides (Yeap et al., 2022) that compares the biological effects of nZVI and dissolved iron released directly from the NPs on bacteria at the transcriptomic level using an RNA sequencing approach. Two previous transcriptomic studies described only one nZVI effect on microorganisms (Simon et al., 2013; Yan et al., 2020), and these studies were not able to distinguish between the "chemical" and "nano" effect. By unveiling the biological effects at the transcriptomic level, we aim to add an additional layer of understanding to the toxicological effect of nZVI that induces oxidant injury and cell defense mechanisms in bacteria and microalgae. The outcomes of our study are described in the section **4**.

Green alga *R. subcapitata*, is widely regarded as the OECD model organism used for toxicity studies (Hund-Rinke et al., 2022). Given that, standard endpoints have shown that nZVI mainly caused oxidative stress to *R. subcapitata* and *C. reinhardtii* (Gonzalo et al., 2014; Keller et al., 2012; Nguyen et al., 2018b), the transcriptomic causes that result from nZVI exposure are not completely known.

2. Objectives

The main objective was to describe effect of nZVI on prokaryotic (*P. putida*) and eukaryotic microorganisms (*R. subcapitata, C. reinhardtii*). Therefore, the main focus was on their transcriptomic response, while in *P. putida* we aimed to compare the effect of nZVI and dissolved iron released from nZVI and in green algae we aimed to compare the effect of nZVI and non-reactive nFe_3O_4 using RNA-sequencing. Unraveling the underlying regulatory circuit, our goal in this study was to describe how *P. putida* and *R. subcapitata* interlink their defense machineries caused by the exposure of nZVI, nFe_3O_4 and dissolved iron released from nZVI.

2.1 *Pseudomonas putida*

Specific objectives were:

- To characterize the nZVI particles in natural reservoir water
- To evaluate the toxicity effect in *P. putida* posed by 100 mg/L nZVI and iron dissolved from nZVI at physiological and transcriptomic level
- To identify and characterize the expression of different genes during the exposure of nZVI and dissolved iron
- To identify metabolic pathways changed after the exposure of nZVI and dissolved iron

2.2 *Raphidocelis subcapitata* and *Chlamydomonas reinhardtii*

Specific objectives were:

- To characterize the physiochemical properties of nZVI and nFe_3O_4 in algal growth medium
- To compare the phenotypic response of *R. subcapitata* and *C. reinhardtii* upon the exposure to 100 mg/L nZVI and nFe_3O_4.
- To evaluate the toxicity effect in *R. subcapitata* posed by 100 mg/L nZVI and nFe_3O_4 at physiological and transcriptomic level
- To identify and characterize the expression of different genes during the exposure of nZVI and nFe_3O_4
- To identify metabolic pathways changed after the exposure of nZVI and nFe_3O_4

3. Materials, methods, and experimental overview

3.1 nZVI, nFe_3O_4 and preparation of dissolved iron

The reactive Nanofer STAR powder (nZVI) and non-reactive nano-magnetite (nFe_3O_4) were chosen as the representative of iron-based NPs in this study. nZVI with an oxidic layer (CAS no. 7439-89-6, size: 59.8 ± 1.3 nm) and nFe_3O_4 (CAS No. 1317-61-9, size: 50–100 nm) were obtained from NANOIRON, (Czech Republic)

and Sigma Aldrich, Merck, Germany respectively. Activation of 20% nZVI and nFe_3O_4 suspension were activated using a PICO DS-8 homogenizer (Miccra, Germany) according to producer guidelines for 48 h (NANOFER STAR | NANOIRON). A summary of the relevant nZVI and nFe_3O_4 characteristics in the exposure medium [reservoir water and Sueoka's High Salt Medium (HSM)] can be found in **Table 3** and **Table 7**.

3.2 Study on *P. putida*

3.2.1 Bacterial strain

P. putida NCTC 10936 was obtained from the Czech Collection of Microorganisms (Brno, Czech Republic) and maintained in 80% tryptone soy media with 20% glycerol at −80°C. The bacterial stock was revived and incubated on tryptone soy agar (Himedia, India) for 16 h at 30°C. A single bacterial colony was then grown in 10 mL tryptone soy medium (7 h at 30°C, 150 rpm), to obtain the mid-log exponential growth phase of cells (approximately 3.3×10^8 cells/mL). The cells were subsequently harvested, pelleted down, and transferred to reservoir water as an exposure medium for the nZVI toxicity studies.

3.2.2 Reservoir water sampling and characterization

Natural reservoir water (NRW) from a local Harcov reservoir, Czechia (50.7702097N, 15.0755733E) was collected from a depth of 10 cm from a surface point in a spade on 18 November, 2018 (sampling event 1, SE1) and was used as the NP exposure medium. The sampling site was chosen to be the representative of semi-urban area with forest on one side, nearby houses, city center, and school. Sampled water was transported in sterile Duran bottle, five minutes away from laboratory. The pH of the sampled water was assessed immediately after the water collection and was filtered through 0.22 µm membrane filters (MF-Millipore, Germany). The filtrated water was then sterilized and stored at 4°C until further use.

3.2.3 Experimental design

P. putida was exposed to two different forms of iron: 100 mg/L of activated nZVI and 44.5 µg/L of dissolved iron obtained by high-speed centrifugation of 100 mg/L of activated nZVI. Unexposed *P. putida* served as the control. All samples were prepared in triplicate in 50 mL of exposure medium (25°C, 120 rpm) and baffled in respective 250-mL Erlenmeyer flasks in a cell incubator Innova 42 (New Brunswick Scientific, USA). At 0, 3, 6, and 24 h, all flasks were sampled for nZVI characterization, cell viability, RNA extraction for RNA sequencing, and gene expression analysis by qPCR. Additional time point (1 h) was included for measurement of pH, dissolved oxygen (DO) and redox potential (Eh).

3.2.4 Characterization of nZVI and dissolved iron

Characterization of nZVI and dissolved iron involved scanning electron microscopy (SEM) analysis, accompanied by elemental analysis using energy-dispersive X-ray spectroscopy (EDS), differential centrifugal sedimentation (DCS), and inductively coupled plasma optical emission spectrometry (ICP-OES), are detailed in the subsections from **3.2.5** to **3.2.7**.

Dissolved iron, obtained by either the high-speed centrifugal method or filtration through 3-kDa cutoff Amicon® Ultra-15 centrifugal filters (Merck Millipore, USA; see subsection **3.2.7** for details), was compared using 1,10–phenanthroline assay following the manufacturer's instructions.

3.2.5 SEM/EDS analysis

All samples tested on interaction between *P. putida* and nanoparticles were subjected to surface morphology imaging using a Zeiss Ultra Plus field-emission SEM (Zeiss, Germany). Each sample was fixed onto an aluminium stub using double-sided carbon tape and cleaned with RF plasma (Evactron) for 10 min before SEM analysis. SEM images were acquired at an accelerating voltage of 5 kV at low probe current (about

15 pA) using a 20 µm In-Lens secondary electron detector with SmartSEM software. Simultaneously, energy-dispersive X-ray spectroscopy (EDS) was performed at an accelerating voltage of 10 kV during the SEM observation by Oxford X-max 20 (Oxford Instruments, United Kingdom) for elemental mapping analysis of nZVI. The EDS data was then acquired and processed using Aztec 3.3 SP1.

3.2.6 DCS analysis

Medium samples were sampled following their nanoparticle spiking respectively at 0, 3, 6, 24 h for particle sizing studies by differential centrifugal sedimentation (DCS) running on a DC24000 disc centrifuge (CPS Instruments Inc., United Kingdom). The CPS disc centrifuge was set an operating speed at 2519 rpm and a series of sucrose densities gradient were constructed from a gravimetrically prepared sucrose solution (8% and 24% respectively) in purified water. In shielding the gradient density layers against any evaporation, a 0.5 mL of *n*-dodecane was injected on top of the sucrose gradient. The sucrose gradient was then left equilibrated stabilized for 20 min to achieve its close proximity of stable density and viscosity state. Each injected sample (0.1 mL) for particle size measurement was preceded by an internal standard using a 0.1 mL of polyvinyl chloride (PVC) calibrant in water (CPS Instruments Inc., United Kingdom) with nominal size 1.4 microns and density 1.385 g/cm^3.

3.2.7 Methods of separation to prepare dissolved iron

Two separation methods (centrifuge and filtrate through 3 kDa filter) were compared to obtain dissolved iron from 100 mg/L nZVI suspended in exposure medium. Total iron including dissolved Fe^{2+} and Fe^{3+} were analyzed directly by LCK 320 iron measuring kit (Hach Lange GmBH, Germany) following manufacturer's instructions using 1,10–phenanthroline colorimetric assay. The measurements were made following after the nZVI dissociation in exposure medium at 0 h (immediate sampling without prolonged nZVI incubation in exposure medium) and after 24 h (sampling after 24 h of nZVI incubation in exposure medium). Comparison of the separation methods can be found in (**Table 4**). Prior the optimization method to prepare the

dissolved iron from 100 mg/L nZVI suspension, the concentration of total iron in dissolved iron sample was determined by inductively coupled plasma optical emission spectrometry (ICP-OES) on an OPTIMA 2100 DV (Perkin Elmer) spectrophotometer measured at 0, 6, 24 h. Sterile exposure medium was used as the blank control in the ICP-OES analysis. ICP-OES analysis of dissolved iron can be found in (**Figure 3**).

3.2.8 Physicochemical analysis

pH, oxidative reduction potentials (ORPs), and DO were measured using a SenTix® 980 pH electrode, a SenTix® ORP-T 900 probe, and an FDO® 925 optical oxygen sensor (WTW Inolab, Germany), respectively. ORP values were converted to redox potentials (Eh). The full calculation of Eh – pH diagrams and the geochemical modelling of respective nZVI particles and dissolved iron were performed under the following conditions: with total iron concentration set at 0.04 mg/L and corresponding Fe^{2+} activity = 6.0^{-7} mol/kg, at 25°C, and pressure 0.1013 MPa calculated by PHREEQUE program (Parkhurst and Appelo, 2013). The geochemical model of respective nZVI and dissolved iron systems were generated based on the Eh – pH data using act2 program from Geochemist's Workbench software system (Bethke, 2007) and their progress reaction in both the systems were simulated. The stability of different iron species in both nZVI and dissolved iron systems were assessed using the thermodynamic database retrieved from The Nuclear Energy Agency's thermochemical database 2020. Total organic carbon in the freshly sampled exposure medium was analyzed using a MULTI N/C 2100S analyzer (Analytik Jena, Germany). Anions and cations were analyzed using a Dionex ICS-90 ion chromatographer (Thermo Fisher, USA) and an inductively coupled plasma mass spectrophotometer (OPTIMA 2100 DV, Perkin Elmer).

3.2.9 Cell morphology and viability

The bacterial cell morphology and viability were evaluated using a LIVE/DEAD® BacLight™ viability kit (Molecular Probes Life Technologies, USA). Equal amounts

of component A (SYTO9 green fluorescent dye, 3.34 mM) and component B (propidium iodide, 20 mM) were diluted following the manufacturer's protocol. Equal volumes (100 µL) of each pre-mixed dye and bacteria culture were mixed and incubated for 15 min in the dark at room temperature (25°C). The cells were then observed under an Axio Imager fluorescence microscope coupled with a AxioCam MRm camera and an EC Plan-Neofluar 63×/0.50 Ph 2 objective (Zeiss, Germany) with excitation at 470 nm and emission at 490 – 700 nm. Randomly selected areas ($n \geq 20$) were captured to obtain 300 total individual cells, and average live cell numbers were calculated and expressed as a percentage of the total cell count. Cell viability was additionally determined by cultivation method. All samples were diluted 10-fold with physiological solution (0.9% NaCl), and 1 mL of the diluted cell suspension was seeded onto agar plates (Plate Count Agar; Bio-Rad, France). Plates were then incubated at 27°C for 48 h. The total number of colony forming units (CFU) was expressed in $\log_{10}$ (CFU/mL).

3.2.10 Evaluation of different RNA extraction methods

Eight RNA extraction protocols from several manufacturers including TRI reagent, RNAzol (Molecular Research Center, United Kingdom), TRIzol (Invitrogen, USA), DirectZol, Quick DNA/RNA microprep (Zymo Research, USA), NucleoSpin RNA Plus, NucleoSpin miRNA (Macherey Nagel, Germany) and ISOLATE II RNA Mini (Bioline, Canada) were used for the comparison to extract the RNA in the samples exposed to 100 mg/L nZVI and 44.5 µg/mL dissolved iron. Subsequent RNA washing steps and DNA removal are detailed in subsection **3.2.11**.

3.2.11 Cell harvesting for RNA isolation and transcriptomics analysis

Samples treated with nZVI particles were removed by a KV-70-70-25-N dimensional nickel-plated block magnet (UNIMAGNET, Czechia) before RNA extraction. The RNA was harvested after 0, 3, 6, and 24 h from nZVI-exposed cells and after g0 and 24 h from dissolved iron-exposed cells using an Isolate II RNA Mini Kit (Bioline, Canada). Cell pellets were obtained through centrifugation at 21,000 × *g*, 4°C for 15

min and added immediately 1 mg/mL of lysozyme and incubated at 37°C for 10 min prior to the addition of RNA lysis buffer. The subsequent DNase treatments and RNA washing steps were then treated as described in a previous study (Yeap et al., 2021). The integrity of the total RNA (RIN) was determined with an Agilent RNA ScreenTape by 2200 TapeStation system (Agilent Technologies, Germany) and Qubit™ RNA Broad Range Assay Kit using Qubit 2.0 fluorometer (Life Technologies, USA) was for RNA concentration quantification.

3.2.12 Whole transcriptome sequencing and data analysis

To prepare for whole-transcriptome sequencing of the RNA-seq library, triplicate biological flasks containing starting material with at least 700 ng of total RNA (RIN > 7) were depleted of rRNA using a NEBNext rRNA depletion kit for bacteria (New England Biolabs, USA) following the manufacturer's instructions. Then, the RNA was prepared using a NEBNext® Ultra™ II RNA Library Prep kit for Illumina® (New England Biolabs). The resulting cDNA libraries were pooled and were sequenced using an Illumina NextSeq system with an 85-bases read length in the forward direction.

Approximately of 26 million reads were obtained respectively from each library (**Table 5**), the first 15 nucleotides of the reads of the adapters were trimmed, and the adapters were aligned to the *P. putida* KT2440 reference genome (GenBank Accession no. AE015451.2) using STAR aligner (Dobin et al., 2013) and accessed for transcripts level (ht-seq count). The differential gene expression for each condition was illustrated using the *relative log* expression function in the DESEQ2 (Love et al., 2014) package, and statistical analysis was performed through the *p.adjust* function in R software. Genes showing $\log_2$ (fold change) of ≥ 1.0 or ≤ -1.0 and adjusted P-value < 0.05 were considered to be significantly expressed. Clustering and visualization of the dissimilarity matrix was achieved using *pheatmap*. Principal component analysis was performed based on PCAtools package. Following the differential gene expression analysis, functional annotation of the expressed genes was conducted using *Pseudomonas* Genome Database (https://www.pseudomonas.com/) (Winsor et al., 2016). Genes clustering into

metabolic pathway subtypes were grouped using the KEGG database (https://www.kegg.jp/kegg) (Kanehisa and Goto, 2000) and BioCyc database collection (https://biocyc.org) (Karp et al., 2019). Additional data analysis, the differentially expressed genes were co-analyzed using protein-protein interaction (PPI) software to analyze for possible gene interactions and was performed using STRING version 11.0 (https://string-db.org/) (Szklarczyk et al., 2018) with *k*-means clustering and interaction score of (medium confidence > 0.4) as the cut off criterion. For every *p*-value presented in PPI analysis, the false discovery rate (FDR) was controlled using the Benjamini–Hochberg method (Benjamini and Hochberg, 1995). Construction and visualization of PPI network was performed using Cytoscape software version 3.8.2 (Shannon et al., 2003). The raw sequencing data of *P. putida* in response to nZVI NPs and dissolved iron of nZVI have been deposited into the NCBI GEO data bank (accession number GSE197899).

3.2.13 Validation of transcriptomics data by quantitative real time PCR

Quantitative real time gene expression analysis was performed using LightCycler 480 (Roche, Germany) and a Roche LightCycler® 480 SYBR Green I master. The gene expression of classical ROS detoxifying regulators such as *aphC*, *katA*, *sodB*, oxyR, and *finR* were compared in the RT-qPCR analysis. 100 ng of total RNA from all samples (*P. putida* + nZVI) and (*P. putida* + dissolved iron) including negative control (*P. putida*) were reverse transcribed into first-strand cDNA by using random hexamer as the priming strategy via SuperScript™ IV First-strand cDNA synthesis system (Invitrogen, USA) following the manufacturer's protocol. All primer pairs used in this study are listed in (**Table 1A and Table 1B**) and were used for cDNA real time PCR amplification. All PCR reactions were prepared in duplicate reactions. One microliter of reverse transcribed cDNA was used as a start-up template in PCR reaction prepared in Roche LightCycler® 480 SYBR Green I Master (Roche, Germany) with a total volume of 10 µL reaction and the quantitation of cDNA gene expression was performed using LightCycler 480 (Roche, Germany). The parameters of real time PCR amplifying protocol was set as follows: 5 minutes at 95°C, followed by 35 repeats of heating at 95°C for 30 seconds, and 30 seconds at 57.5°C. Plate read

was inserted at the end of the cycle while melt curve analysis was included after the repeating cycles setting at 65°C to 95°C, 0.5°C increment, 5 seconds per step to check if the predominant amplification product had a same melting temperature featuring with the expected cDNA sample. To determine genomic DNA (gDNA) carry-over from RNA isolation and contamination of the reagent used, using one primers pair from (**Table 1**), control reactions without RNA template serving as no template control (NTC) and another control reaction adding RNA template without reverse transcriptase serving as no enzyme control were compared along to the treatment signals. Real time PCR signal without cDNA amplification close to the baseline of NTC control were considered negative for gDNA contamination. The threshold cycles (C_t) of each sample resulting from the amount of amplified cDNA signals were acquired from LightCycler® 480 software Rel.1.5.1 (Roche) and the signals were set relative to a negative control condition without nanoparticle exposure (*P. putida*) and correct-normalized using single reference gene system (*gyrB* gene). Subsequently, the relative transcriptional changes were calculated using delta-delta C_t of the $2^{-\Delta\Delta Ct}$ method (Livak and Schmittgen, 2001) according to the three equations below and the final cDNA gene expression value is presented in Equation 3:

$$\Delta C_t = C_t(target\ gene) - C_t(reference\ gene) \quad (1)$$

$$\Delta\Delta C_t = \Delta C_t(treatment) - \Delta C_t(control) \quad (2)$$

$$Relative\ expression\ ratio = 2^{-\Delta\Delta Ct} \quad (3)$$

where C_t is the threshold cycle of the amplified cDNA signal that reached above baseline fluorescence level, (Eq. 1, ΔC_t) denotes differences in threshold cycle between the target genes and reference gene (*gyrB*), (Eq. 2, $\Delta\Delta C_t$) is the differences in Eq. 1 between the treatment samples (*P. putida* + nZVI) or (*P. putida* + dissolved iron) and negative control (*P. putida*).

Table 1A. Housekeeping gene used as a reference gene in real time PCR

Labels	Sequence (5'→3')	Genes	Reference
gyrB-F	GCCGTGGAACAGGAGATGAA	(DNA gyrase subunit B)	This study
gyrB-R	GGCTTTACGAGCTGCTTCAC	*gyrB*	

Table 1B. List of target genes used in real time PCR

Primers	Sequence (5'→3')	Genes	Reference
aphC-F	CGGTACCTTCGTGATCAACC	(NADH peroxidase)	This study
aphC-R	CTTCGCCTTCTTTCCACTTG	*aphC*	
finR-F	GCTGGAACACACTGAAGCAA	(Redox sensing)	This study
finR-R	AATAGAACTGGCGCATCAGG	*finR*	
katA-F	GCCGTCAAGTTCTACACCGA	(Catalase)	This study
katB-R	CATCTGGGCGTTCTTCAGGT	*katA*	
oxyR-F	CTACATCGTCACACTCGCCC	(redox sensing)	This study
oxyR-R	CTTCTTCACACCGACCGACA	*oxyR*	
sodB-F	GACCCTGGAAGAGATCGTCA	(Superoxide dismutase)	This study
sodB-R	CTTGTCGAAGGAACCGAAAG	*sodB*	

3.2.14 Statistical analysis

Statistical analysis was performed using Prism (GraphPad, USA). The mean differences of the treatment groups were compared against a *P. putida* control by two-way ANOVA and Dunnett's multiple comparison test. The comparisons were considered statistically significant at *P < 0.05, **P < 0.001, ***P < 0.0001.

3.3 Study on *R. subcapitata* and *C. reinhardtii*

Experiments involving the algae *R. subcapitata* were similar as *P. putida*'s study, including a detailed physiological and transcriptomic analysis using RNA-seq as described in the subsection **4.2**. Experiments involving algae *C. reinhardtii* covered only the physiological endpoints such as cell morphology under light microscope, chlorophyll fluorescence, total viable cell count using hemocytometer, and phytochrome content.

3.3.1 Algal strains and culturing conditions

Raphidocelis subcapitata ATCC 22662 (formerly known as *Pseudokirchneriella subcapitata)* was obtained from the Culture Collection of Autotrophic Organisms (CCALA, Czech Republic) and maintained in Bold's Basal Medium (BBM) at 24°C. *Chlamydomonas reinhardtii* wild type CC-5325 was obtained from *Chlamydomonas* Resource Center, St. Paul, University of Minnesota (USA) and maintained in Tris-acetate-phosphate media (TAP) (Harris et al., 2009) at 24°C. For NPs experiments, they were cultivated in Sueoka's high salt medium (HSM) (Sueoka, 1960), with gentle mixture of 1% CO_2 and air bubbling supply under a 130 µmol photons$\cdot m^{-2}\cdot s^{-1}$ of constant white light illumination at room temperature (24°C). The algae in mid-log exponential phase were harvested after 48 h at an initial cell density of 1.575×10^7 cells/mL for *R. subcapitata* and 6.026×10^6 cells/mL for *C. reinhardtii*, and then added to a flask containing NPs.

3.3.2 Experimental design

R. subcapitata and *C. reinhardtii* were exposed to two different forms of activated iron NPs (100 mg/L of nZVI and nFe_3O_4 respectively), while NP-free samples served as a control. Three replicates for each condition were conducted in 550 mL of HSM, starting with 45 mL of pre-grown algal culture. 15 mL of the culture was sampled every 24 h before NPs exposure (up to 48 h) and after the start of NPs exposure at 0, 1, 4 h and thereafter every 24 h up to 120 h. Subsamples were taken for physicochemical analysis, microscopic imaging, determination of algal cell numbers,

chlorophyll fluorescence, and phytochrome measurement (total chlorophyll and carotenoid contents). In addition to these analyses, cultures (35 mL) were sampled after NPs exposure at 1 and 4 h for RNA extraction. All the measurements were recorded in three technical replicates per biological sample for each time point and averaged prior to data analysis.

3.3.3 Characterization of nZVI and nFe_3O_4

Characterization of nZVI and nFe_3O_4 will be as similar to the experiments performed for *P. putida*. The experiments include SEM/EDS, DCS, and ICP-OES analyses, are detailed in the subsections from **3.2.5** to **3.2.8**.

Total dissolved iron of nZVI and nFe_3O_4, were derived from the respective aqueous phase of 100 mg/L nZVI and nFe_3O_4 suspension dispersed in HSM. Their aqueous phase was recovered and obtained by high-speed centrifugation at 12, 500 × *g* for 20 min per cycle and the sedimented insoluble nZVI and nFe_3O_4 particles were discarded. A second similar centrifugation cycle was repeated again to obtain the total dissolved iron of nZVI and nFe_3O_4 in order to determine the total dissolved iron in the suspension by ICP-MS.

3.3.4 Physicochemical analysis

The physicochemical analysis included pH, DO and ORP measurements. Details of these analyses (pH, DO, and ORP) follow subsection **3.2.8**. ORP values were converted to redox potentials (Eh). Eh–pH and geochemical modelling were also included in the *R. subcapitata* samples exposed to nZVI and nFe_3O_4. The full calculation of Eh – pH and the geochemical modelling of respective nZVI particles and nFe_3O_4 were performed under the following conditions: at the thermodynamic equilibrium state in between the phases of Fe^{2+} ↔ FeOOH with total iron concentration set at 1.489×10^{-7} mg/L and corresponding Fe^{2+} activity = 2.667×10^{-12} mol/kg, at 25°C, and pressure 0.1013 MPa calculated by PHREEQUE program (Parkhurst and Appelo, 2013). The phase activity was calculated at $[Fe^{2+}] = 1 \times 10^{-3}$ m, pH = 7, $\log f_{CO_2\,(g)} = -1.854$ and Eh = 0.3 V. The geochemical model of respective

nZVI and nFe_3O_4 systems were generated based on the Eh – pH data using *act2* program from Geochemist's Workbench software system (Bethke et al., 2021) and their progress reaction in both the systems were simulated. The stability of different iron species in both nZVI and nFe_3O_4 systems were assessed using the thermodynamic databases retrieved from The *GWB* and *PHREEQC* Modifications thermo datasets 2021.

3.3.5 Microscopy imaging and viable cell count

Algae cell distribution was imaged under optical microscopy (Motic BA310, Motic, China) to assess the substantial physical interaction, NPs aggregation and calculation of total cell number. The cell number was determined by manual cell counting using a Neubauer hemocytometer (Superior Marienfeld, Germany). The autofluorescence intensity and of viable cells number were observed under an AxioImager microscope coupled with AxioCam 705 mono camera and an EC Plan-Neofluar 5×/0.16 M27 objective (Zeiss, Germany) with excitation at 455 – 495 nm and emission at 505 – 555 nm. Randomly chosen areas were captured ($n \geq 20$) to obtain 300 total individual cells and average live numbers were calculated and expressed in percentage.

3.3.6 Chlorophyll fluorescence analyses

Chlorophyll fluorescence was measured in a 48-well flat bottom plate using a closed FluorCam FC 800-C Video Imager (Photon Systems Instruments, Brno, Czech Republic). Before the measurement, samples were dark-adapted for at least 15 min. The evaluation of fluorescence parameters [Maximum PSII yield (F_v/F_m), non-photochemical quenching (NPQ), effective PSII yield (Φ PSII)] were calculated as described (Maxwell and Johnson, 2000; Murchie and Lawson, 2013).

3.3.7 Measurement of phytochrome content

The phytochrome concentrations (total chlorophyll and carotenoids) were determined by 90% methanol as described previously (Lichtenthaler, 1987) and calculated

according to (Wellburn, 1994). All spectral analysis was performed using UV/vis photo spectrometer (Genesys 10S, Thermo Scientific) where deionized water was used as a blank against the whole culture reading.

3.3.8 Performance evaluation of different RNA extraction methods

RNA isolation of microalgae *R. subcapitata* involved two major steps: the cell lysis and then the RNA extraction procedure. Several cell lysis methods were first compared using cell ribolization on a ribolizer, liquid nitrogen grinding, and overnight cell lyophilization at –30°C to effectively lyse the cell walls while releasing the cellular components. To compare different cell lysis method used, the disintegration of the microalgae cell membranes was then imaged under optical microscopy (Motic BA310, Motic, China). Four RNA extraction protocols from several manufacturers including ISOLATE II RNA Plant mini (Bioline, Canada), Quick-RNA™ Miniprep kit (Zymo Research, U.S.A), RNeasy Plant Mini kit (Qiagen, Germany), and phenol–chloroform extraction (Chomczynski and Sacchi, 2006) were used for the comparison to extract the RNA in the samples exposed to 100 mg/L nZVI and nFe_3O_4 respectively. Optimization of these extraction methods have been explained in a previous work from (Yeap et al., 2021).

3.3.9 Cell harvesting for RNA isolation and transcriptomics analysis

RNA was harvested from three biological replicates after 1 and 4 h from *R. subcapitata* exposed with nZVI and nFe_3O_4 respectively. Cell pellets were obtained through centrifugation at 10,000 × *g*, 4°C for 2 min, followed by overnight cell lyophilization and phenol-chloroform extraction method adapted from a previous work (Yeap et al., 2021). The integrity and concentration of the RNA extracts were determined with an Agilent 2100 Bioanalyzer system (Agilent Technologies, Germany) and Nanodrop (Thermo Scientific, USA) was for RNA concentration quantification. All electropherogram of ribosomal RNA peaks were computed and analyzed by 2100 Expert software (Agilent Technologies, Germany). To prepare for whole transcriptome sequencing of the directional RNA-seq library, up to 1 µg of

total RNA (RIN > 6) was used with a TruSeq® stranded mRNA Library Prep kit (Illumina Inc., USA) after capturing poly-adenylated transcripts and mRNA fragmentation. The resulting cDNA libraries were pooled and sequenced in paired-end mode (2 × 79 bp) on an Illumina NextSeq 500/550 High Output v2 platform.

3.3.10 Genome completeness assessment

Completeness assessment for the *R. subcapitata* ATCC 22662 genome (GenBank Accession number: BDRX01000001.1) was performed using BUSCO (Benchmarking Universal Single-Copy Orthologs) v3.0.2 with the chlorophyta_odb10 database and default settings (Simão et al., 2015). In addition, by means of mapping the transcriptome data to the *R. subcapitata* genome by applying bwa-mem v0.7.10 (Li and Durbin, 2009), the correctness of the consensus sequence in coding regions was controlled.

3.3.11 Sequencing data analysis, and visualization

Approximately five million 2 × 79-bp paired end reads were generated respectively from each library (**Table 8**) by the means of Illumina sequencing on a NextSeq 500/550 High Output v2 platform. The Illumina TruSeq adapter sequences (34 nucleotides) were then clipped by *Illumina bcl2fastq2* Conversion Software v2.19.1 using standard parameters. The FASTQ files were first trimmed (minimum quality 3, minimum read length to be kept 36 bp) using the Trimmomatic tool (http://www.usadellab.org/cms/?page=trimmomatic) (Bolger et al., 2014). The processed sequence reads were then mapped to *R. subcapitata* ATCC 22662 reference genome (GenBank Accession number: BDRX01000001.1) (Suzuki et al., 2018) using *HISAT2* (Kim et al., 2019). *SAMtools* (Danecek et al., 2021) was then applied to access the transcripts level in order to get quantitative assignments and to generate the BAM files. After that, BAM files were selected for the determination of read counts and identification of differentially expressed genes (DEGs). To define the transcripts abundance, read counts for each BAM file were determined by bedtools v2.27.1 and its option multicov (Quinlan and Hall, 2010). The established read count table was then imported into idep 1.0 (Ge et al., 2018). Then, the gene

expression level in counts per million (CPMs) were calculated and visualized in box and PCA plot. To identify DEGs, the BAM files were loaded and processed in *R* using *Rsamtools* package (Morgan et al., 2022). Prior than that, gene models were imported and queried using *GenomicFeatures* (Lawrence et al., 2013) package and followed by using *GenomicAlignments* (Lawrence et al., 2013) package to create the Summarized Experiment object that contains the fragment counts for each gene and sample. Differential gene expression for each condition was illustrated using relative log expression function of the *DESEQ2* (Love et al., 2014) package and statistical analysis was through the function *p.adjust* in *R*. Venn diagrams were plotted by *VennDiagram* (Chen and Boutros, 2011) package. Genes showing $\log_2$(fold change) ≥ 1.5 and ≤ -1.5, and adjusted *p*-value less than 0.05 were considered to be significantly expressed. Furthermore, a $\log_2$(fold change) ≥ 1.5 and ≤ -1.8 cutoff was applied only to the sample T1nZVI (nZVI exposure at 1 h) versus T1neg (control at 1 h), due to high number of DEGs. Clustering and visualization of the dissimilarity matrix was achieved using *ClustVis* – a web tool for visualizing clustering of multivariate data (http://biit.cs.ut.ee/clustvis/) (Metsalu and Vilo, 2015) and *pheatmap* packages. The heatmap function was applied with default setting (Manhattan distance and average linkage were used). Principal component analysis was performed based on PCAtools package. Following the differential gene expression analysis, functional annotation and genes classification into metabolic pathway subtypes were grouped using the KEGG database (https://www.kegg.jp/kegg/) (Kanehisa and Goto, 2000) and JGI Algal Genome Portal PhycoCosm (https://phycocosm.jgi.doe.gov) (Grigoriev et al., 2021; Nordberg et al., 2014). Annotation improvement was further performed using alpha version of protein sequence observation service (PSOS) (https://psos-staging.computational.bio/) and UniProtKB database (https://www.uniprot.org/) (Bateman et al., 2022). Additional data analysis, the differentially expressed genes were co-analyzed using protein-protein interaction (PPI) software to analyze for possible gene interactions and was performed using STRING online database version 11.5 (https://string-db.org/) (Szklarczyk et al., 2021) with *k*-means clustering and interaction score of (medium confidence > 0.4) as the cut off criterion. For every *p*-value presented in PPI analysis, the false discovery rate (FDR) was controlled using

the Benjamini–Hochberg method (Benjamini and Hochberg, 1995). Construction and visualization of PPI network was performed using Cytoscape software version 3.9.1 (Shannon et al., 2003) with Cytoscape stringApp 2.0 installed in the software (Doncheva et al., 2022).

3.3.12 Statistical analysis

All statistical analysis was performed using Prism (GraphPad, USA). The mean differences of the treatment groups were compared against a *R. subcapitata* control and *C. reinhardtii* control respectively by two-way ANOVA and Dunnett's multiple comparison test. The differences were considered statistically significant at *P < 0.05, **P < 0.001, ***P < 0.0001.

4. Results and discussions

Our study demonstrates the presence of an overlooked trade-off between energy consumption and oxidative stress caused by the exposure of nZVI and dissolved iron. RNA sequencing revealed a spectrum of repair pathways in the transcriptome of *P. putida* and *R. subcapitata* that require high energetic cost such as ATP, NADPH.

I. *P. putida*

Application of nZVI for remediation purposes in polluted aquifers inevitably leads to contact with indigenous microorganisms such as the common bacterium, *P. putida* (Mueller et al., 2012). High throughput analyses were undertaken to explore the biological effects of nZVI and dissolved iron on *P. putida* over 24 h, and the enriched biological pathways related to differentially expressed genes (DEGs) were identified.

4.1 Properties of nZVI and dissolved iron in exposure medium

This section describes the characterization of nZVI and dissolved iron before exposure to *P. putida* including SEM/EDS, DCS, and ICP-OES analysis.

The exposure medium used in the study was natural reservoir water. In the water sampling event, the pH value of the reservoir water was near to neutral (pH 7.11 ± 0.01) and common anions and cations concentrations ranged from 10.8 up to 26.5 mg/L; **Table 2**). nZVI used in this study had an average particle diameter 59.8 ± 1.3 nm in its dry powder form and the properties of nZVI is shown in **Table 3**.

Table 2. Natural reservoir water properties

Parameter		
pH		7.11 ± 0.01
Total organic carbon (mg/L)[a]		3.4
Total elements (mg/L)[b]	Mg	2.1
	Ca	11.0
	Na	10.8
	K	0.81
	Fe	N/D
	Mn	0.01
Total anions (mg/L)[c]	Cl^{-1}	26.5
	NO_2^-	N/D
	NO_3^-	6.7
	SO_4^{2-}	23.6
	F^{-1}	0.27

[a] Measurement by TOC analyzer. The detection limit for the analysis was 1 mg/L. [b] Measurement by inductively coupled plasma mass spectrometry (ICP-MS). The detection limit for all the tested elements were ranging from 5 µg/L to 1 mg/L. [c] Measurement by ion chromatograph. The detection limits were 2 mg/L for sulphates and chlorides, while 0.05 mg/L for nitrites, nitrates and fluorides. N/D- Non-detectable

Table 3. Summary of the nZVI physicochemical characteristics in reservoir water

Parameter	
Product no.	7439-89-6 *NANOFER STAR*
Short description	nZVI stabilized with oxidic layer
Primary particle size (nm)[a*]	Diameter: 59.8 ± 1.3, Oxide layer thickness: 4.3 ± 0.53
Hydrodynamic size (nm) [b]	771 ± 65
MW (g/mol) [a]	55.85
SSA (m^2/g) [a]	> 25
Purity (wt.%) [a]	Fe ≥ 65−80, Fe_3O_4 ≤ 35−20
Phase [a]	α−Fe: 74%, FeO: 8%, Fe_3O_4: 18%

ORP (mV)[c] in EM	234.4 ± 1.1
ORP (mV)[c] in 0.9% sodium chloride	144.6 ± 9.6

[a] Reported by the manufacturer, [a*] Determined by Transmission electron microscopy (TEM). [b] Measurement by DCS from immediate and up to 24 h after dispersion in EM (**Figure 1**). [c] Measurement using SenTix® ORP-T 900 probe (WTW Inolab, Germany) immediately after spiking in EM. MW- molecular weight; SSA- specific surface area; ORP- oxidative reductive potential; nZVI- nano zero valent iron; EM- exposure medium sourced from natural reservoir water.

When suspended in exposure medium, the hydrodynamic size distribution of nZVI ranged between 675–858 nm up to 24 h (**Figure 1**).

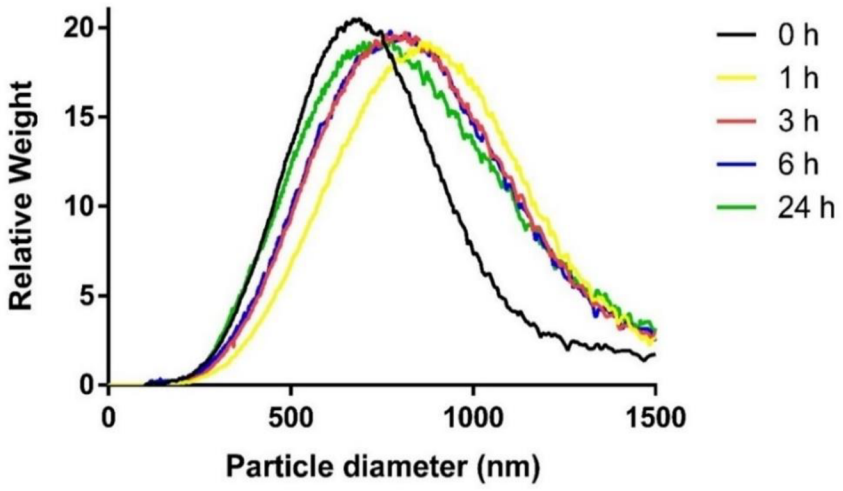

Figure 1. Size distribution of 100 mg/L nZVI dispersed in exposure medium up to 24 h. Values were presented in (nm) determined by differential centrifugal sedimentation (DCS). Analysis at 0 h indicated immediate exposure and instant sampling of the samples. Pristine nZVI had an approximate particle diameter of 59.8 ± 1.3 nm in dry powder. When suspended in exposure medium, the hydrodynamic size distribution of nZVI ranged between 675 and 858 nm up to 24 h.

Furthermore, elemental mapping was performed using energy-dispersive X-ray spectroscopy (EDS). The result shown a correlation with the chemical constituents present in reservoir water (**Figure 2**). **Table 2**, shows the component analysis of exposure medium analyzed by ICP-OES, consisted mostly the Na, Cl^-, and SO_4^{2-} in the exposure medium corresponds to the EDS mapping. The surface morphology of nZVI which determined by SEM after dispersion in exposure medium showed a

rough spherical form and aggregated into chains, which could be attributed to the magnetic interaction between particles (Zhang and Manthiram, 1997). Elemental mapping (EDS) of nZVI when dispersed in exposure medium showed that the nanoparticles surfaces were enriched with the chemical constituents present in natural reservoir water, with the latter Fe element detected in EDS mapping belongs to nZVI particle, since Fe was undetectable in natural reservoir water.

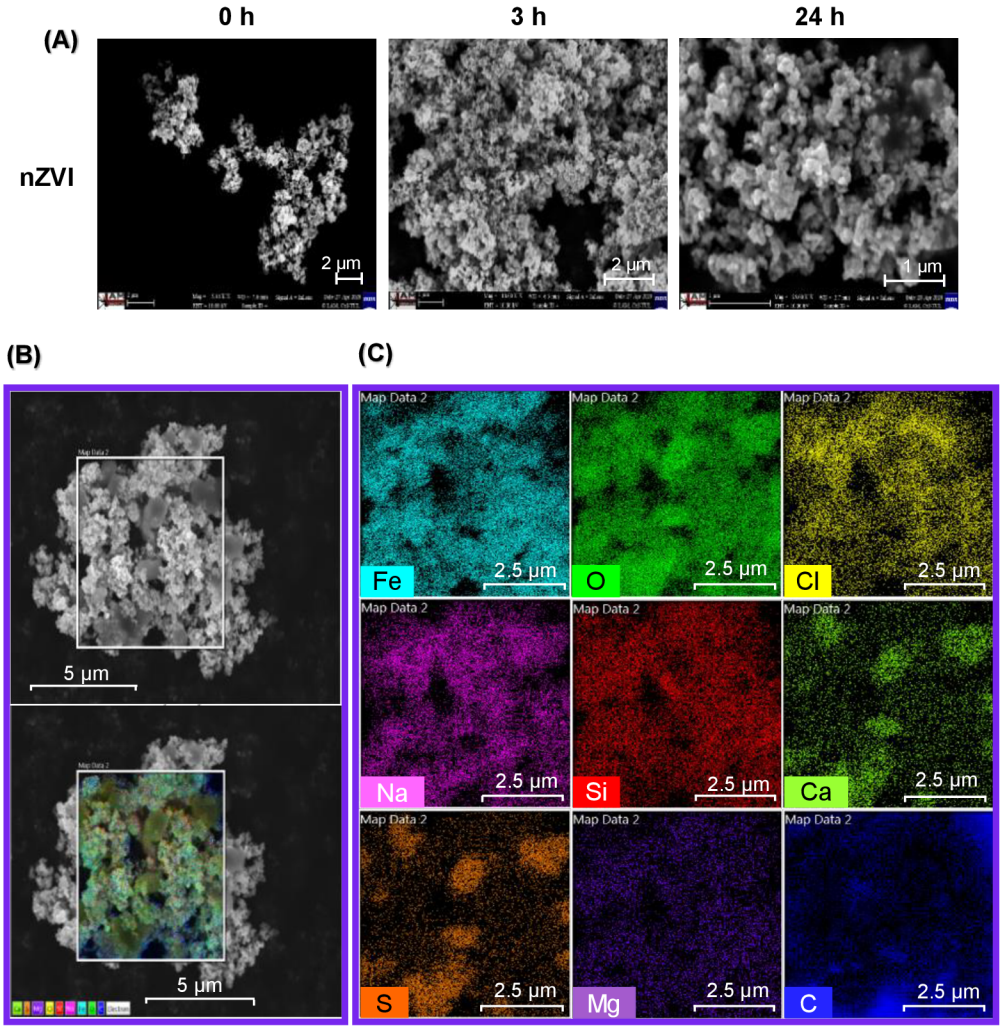

Figure 2. SEM images and EDS chemical hypermaps of pristine nZVI dispersed in exposure medium. (A) SEM imaging of nZVI dispersed in exposure medium at 0, 3 and 24 h. (B) SEM images showing hetero-aggregation between nZVI and salt components from exposure medium at 3 h. (C) SEM/EDS elemental overlay of iron and oxide (Fe and O) from nZVI, chloride, sodium, silicon, calcium, sulfur, magnesium and carbon (Cl, Na, Si, Ca, S, Mg, C) from exposure medium at 3 h. The chemical mapping shows chloride and sodium (yellow

and purple colors) were mostly absorbed to iron and oxide (cyan and green colors) on nZVI surfaces. Scale bars = as indicated in the pictures.

Dissolved iron/ was prepared and compared by i.) high-speed centrifugation method or ii) filtration through 3 kDa filter). Both methods showed similar Fe^{2+}/Fe^{3+} concentrations in exposure medium (**Table 4**). Concerning the large volume of dissolved iron used for gene expression analysis (approximately 150 mL for all biological replicates), preparation of the dissolved iron forms through the standard 3 kDa cut off filter could be laborious since maximum filtrate capacity is 15 mL. Our study showed that, by high-speed centrifugation (twice at 12,500 × *g*), we were able to obtain the dissolved iron in comparable concentrations as after 3 kDa filtration (**Table 4**). Corresponding SEM image confirmed the complete removal of nZVI particles residue (**Figure 8I**). Therefore, high-speed centrifugation was further used to obtain dissolved iron from nZVI. The total iron concentration was consistent up to 24 h (**Figure 3**). Overall, the concentration of dissolved iron in this study was slightly lower compared to previously reported (Nguyen et al., 2018a).

Table 4. Evaluation of separation method to prepare dissolved iron

Centrifugal methods	Units	Dissociation in EM at 0 h	Dissociation in EM after 24 h
(A.) centrifugation twice at 12,500 × *g* for 20min			
(i) Ferrous, Fe^{2+}	µg/L	130 ± 0.00	120 ± 0.00
(ii) Ferric, Fe^{3+}		0.00 ± 0.00	0.00 ± 0.00
(iii) ORP	mV	238.24 ± 7.92	226.39 ± 36.23
(B.) Amicon Ultra centrifugal filter (MWCO = 3 kDa)			
(i) Ferrous, Fe^{2+}	µg/L	120 ± 0.00	120 ± 0.01
(ii) Ferric, Fe^{3+}		0.00 ± 0.00	0.00 ± 0.01
(iii) ORP	mV	248.63 ± 33.48	236.78 ± 22.07

Centrifugal methods used to compare different filtration efficiencies in order to obtain dissolved iron species released from 100 mg/L nZVI suspended in exposure medium: (A) Separation by high-speed centrifugation twice at 12, 500 × *g* for 20 min and (B) separation by Amicon ultra centrifugal filter with a 3 kDa cutoff. The (i) Ferrous iron, Fe^{2+} and (ii) ferric iron, Fe^{3+} were determined using Fe^{2+}/Fe^{3+} colorimetric 1,10–phenanthroline assay. (iii)

ORP- oxidative reductive potential (mean ± SD; n = 3). Note: The analysis was performed in a medium without *P. putida*.

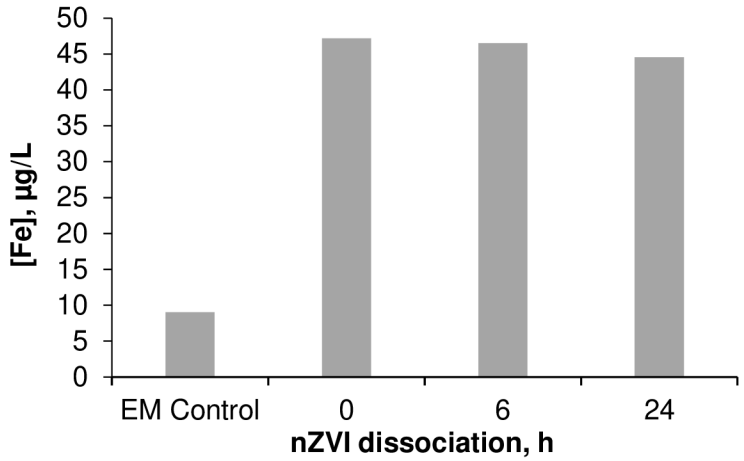

Figure 3. Total iron (Fe^{2+} and Fe^{3+}) released from 100 mg/L nZVI determined by ICP-OES. EM control: untreated exposure medium. Note: analysis was performed in a condition without *P. putida* and separation of the solid particle of nZVI was centrifuged at 12,500 × *g* for 20 min. Second centrifugation cycle was repeated to obtain dissolved iron which is used for exposure studies. Analysis at 0 h indicated immediate exposure and instant sampling of the samples. Exposure condition used for transcriptomic studies with *P. putida*

4.2 Physicochemical parameters of nZVI and dissolved iron during exposure

The physicochemical parameters (pH, dissolved oxygen [DO], and oxidative/reductive otential [Eh]) of the different exposure conditions are presented in **Figure 4**. Conditions without *P. putida* remained stable throughout the 24-h experiment. Following the addition of both forms of iron along with *P. putida* in the exposure medium, the pH, DO, and Eh evolved differently. The initial pH value was 6.8, whereas the introduction of nZVI into the medium with *P. putida* increased the pH to 7.3 after 24 h of exposure (**Figure 4A**). This increase in the pH of the medium after the addition of nZVI has also been observed in other studies (Nguyen et al., 2018a). However, the significant increase reported in previous studies was not observed in our system; this was probably due to the presence of DO. Notably, the medium containing *P. putida* and dissolved iron showed lower pH profile compared

to other conditions, reaching to its lowest point after 3 h (pH 6.2; $P < 0.0001$) and recovering slowly to the initial value (6.8) after 24 h. The addition of nZVI and dissolved iron to the exposure medium containing *P. putida* resulted in lower DO profiles throughout the exposure hours (**Figure 4B**), particularly after 6 h (5.2 mg/L; $P < 0.001$ and 4.8 mg/L; $P < 0.0001$, respectively). The DO levels returned to their original values (5.0 – 5.7 mg/L) within 24 h.

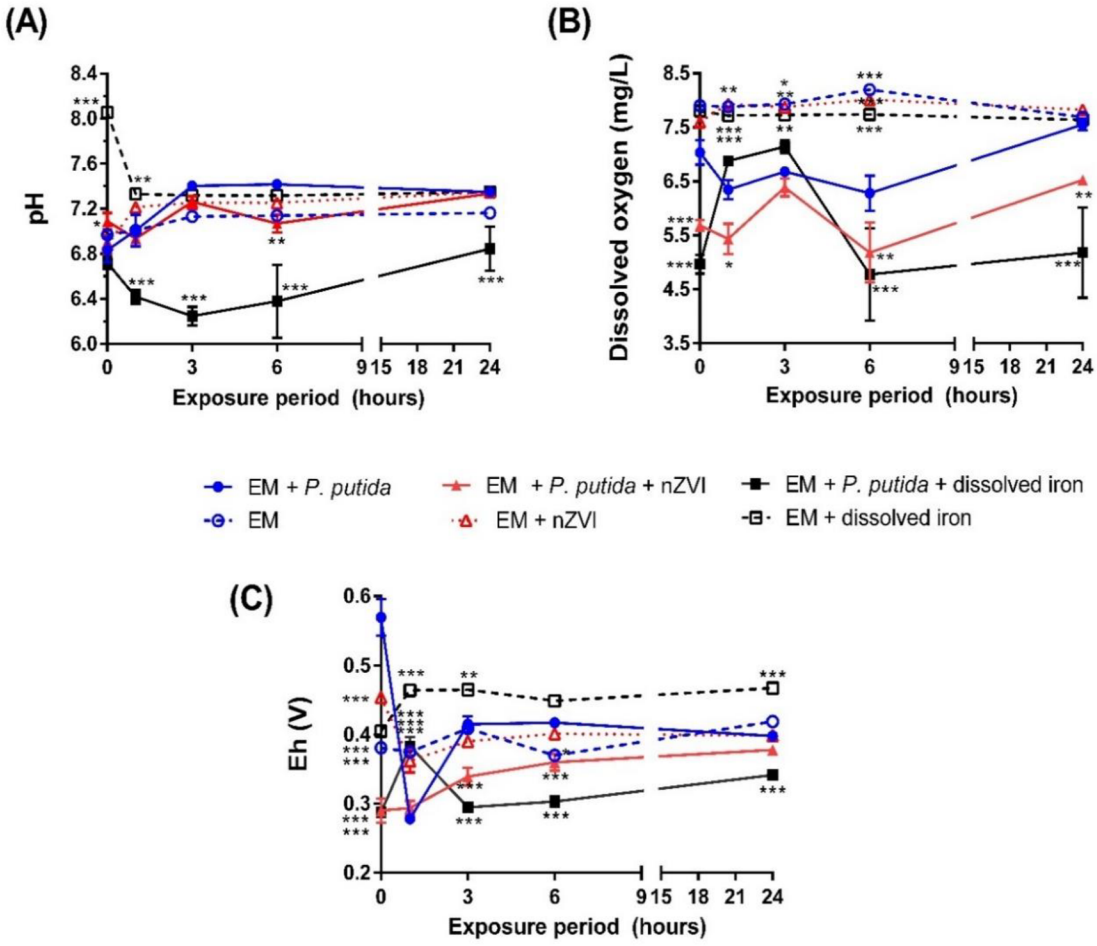

Figure 4. Physicochemical parameters of *P. putida* in the exposure medium treated with nZVI and dissolved iron at 0, 1, 3, 6, and 24 h. (A) pH, (B) dissolved oxygen level, and (C) redox potential. Four negative controls contained exposure medium, *P. putida*, nZVI, and dissolved iron. nZVI and dissolved iron were added to the exposure medium containing *P. putida* (mean ± SD; n = 3). Two-way ANOVA and Dunnett's test were used to calculate the statistical differences between the treated (nZVI, dissolved iron) and untreated media

containing *P. putida* (*P < 0.05, **P < 0.001, ***P < 0.0001). Note: Different scales for the *y*-axis.

Overall Eh fluctuation was observed in the time span between 0 and 3 h and stabilized after 3 h until the end of the exposure, returning to their initial values within 24 h (**Figure 4**C). The addition of nZVI in previous studies instantly reduced the Eh (Barnes et al., 2010; Nguyen et al., 2018); however, higher concentrations were applied. In the medium containing *P. putida*, nZVI did not cause a reduction in Eh; instead, the Eh increased steadily over 24 h. *P. putida* treated with dissolved iron showed the lowest Eh levels in most of the exposure period around 0.3 V ($P < 0.0001$). Simultaneously, the geochemical modeling showed the most probable elemental forms of iron in the system under certain Eh–pH values (**Figure 5**).

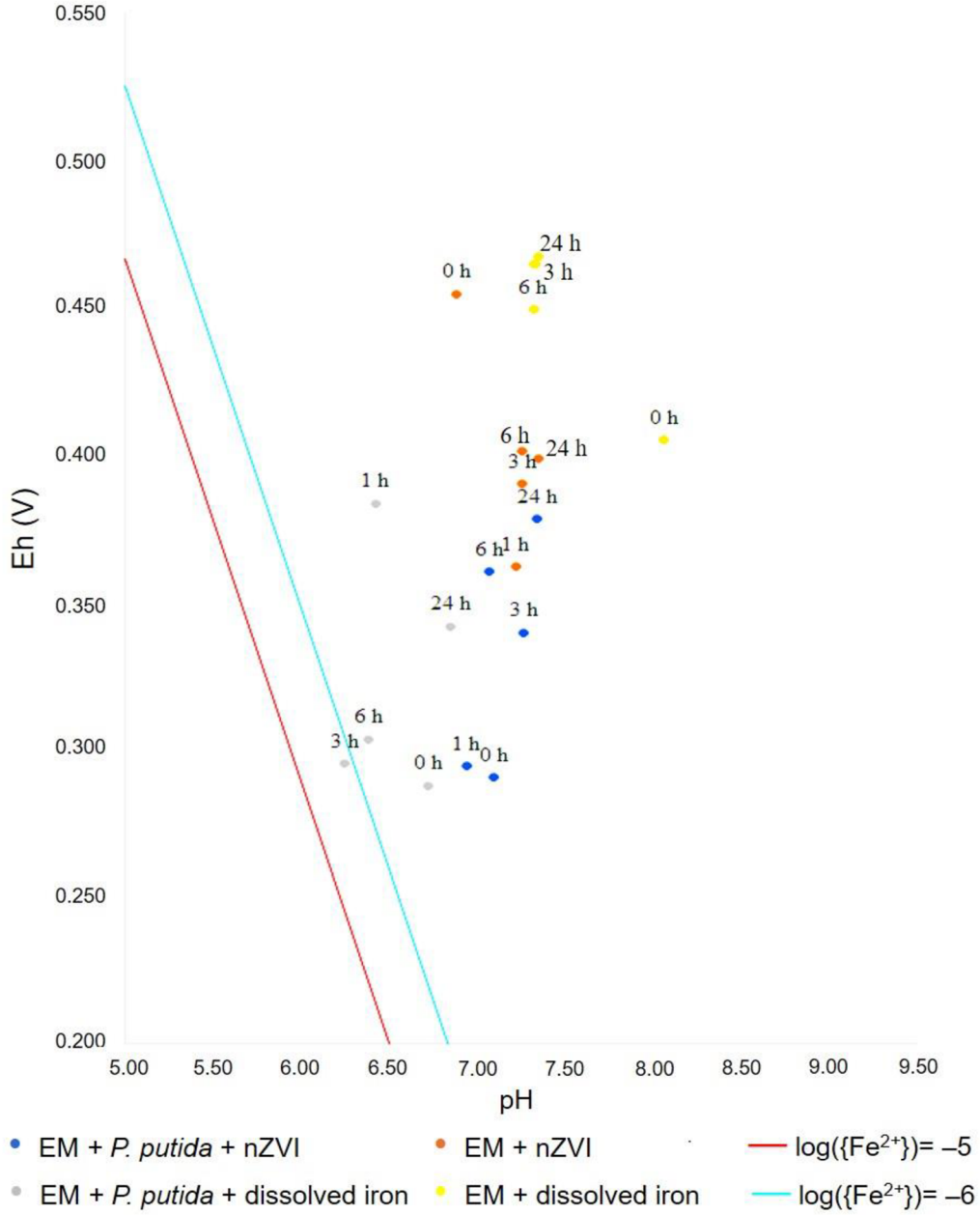

Figure 5. Overview of the Eh–pH values with all the treatments conditions plotted in the graph. Colors of the dots represent a different treatment condition: (i) (Blue dots- EM + *P. putida* + nZVI): *P. putida* exposed to 100 mg/L nZVI in exposure medium, (ii) (orange dots- EM + nZVI): contains only 100 mg/L nZVI in exposure medium, (iii) (Grey dots- EM + *P. putida* + dissolved iron): *P. putida* exposed to 44.5 µg/L dissolved iron in exposure medium, (iv) (yellow dots- EM + dissolved iron): contains only 44.5 µg/L dissolved iron in exposure medium. The solid lines define the dependence of the equilibrium state in between the solid and liquid phases of $Fe(OH)_3$ crystallization for the logarithm of the Fe^{2+} activity, $\log\{Fe^{2+}\} = -5$ (red line) and $\log\{Fe^{2+}\} = -6$ (blue line). These identified values were also identical for

the equilibrium state in between the solid and liquid phases of goethite FeOOH crystallization. The *x* axis shows the pH values, the *y* axis as the redox potential (Eh) values presented in Volts. EM denotes exposure medium sourced from natural reservoir water.

These models simulated the evolution of iron speciation during the experiment and suggested a higher presence of reactive species in the samples that contained dissolved iron (**Figure 6, Figure 7**). In the presence of nZVI, the pH of the exposure medium ranged from 6.88 to 7.35, and the Eh values ranged from 0.290 to 0.454 V. Based on the Eh–pH diagram, nZVI largely formed the insoluble iron categories that predominated the goethite at higher Eh levels (**Figure 6**), a result that was consistent with the findings of a previous study (Kumar et al., 2014; Liu et al., 2017). Conversely, the pH of the medium containing dissolved iron ranged from 6.25 to 8.06, and the Eh values ranged from 0.287 to 0.467 V. In the Eh–pH diagram, it could be seen that there were no insoluble iron categories. Most of the dissolved iron was present as $Fe(OH)_3$ (aq) and only a small portion as either Fe^{2+} or $Fe(OH)_2^+$ (**Figure 7**).

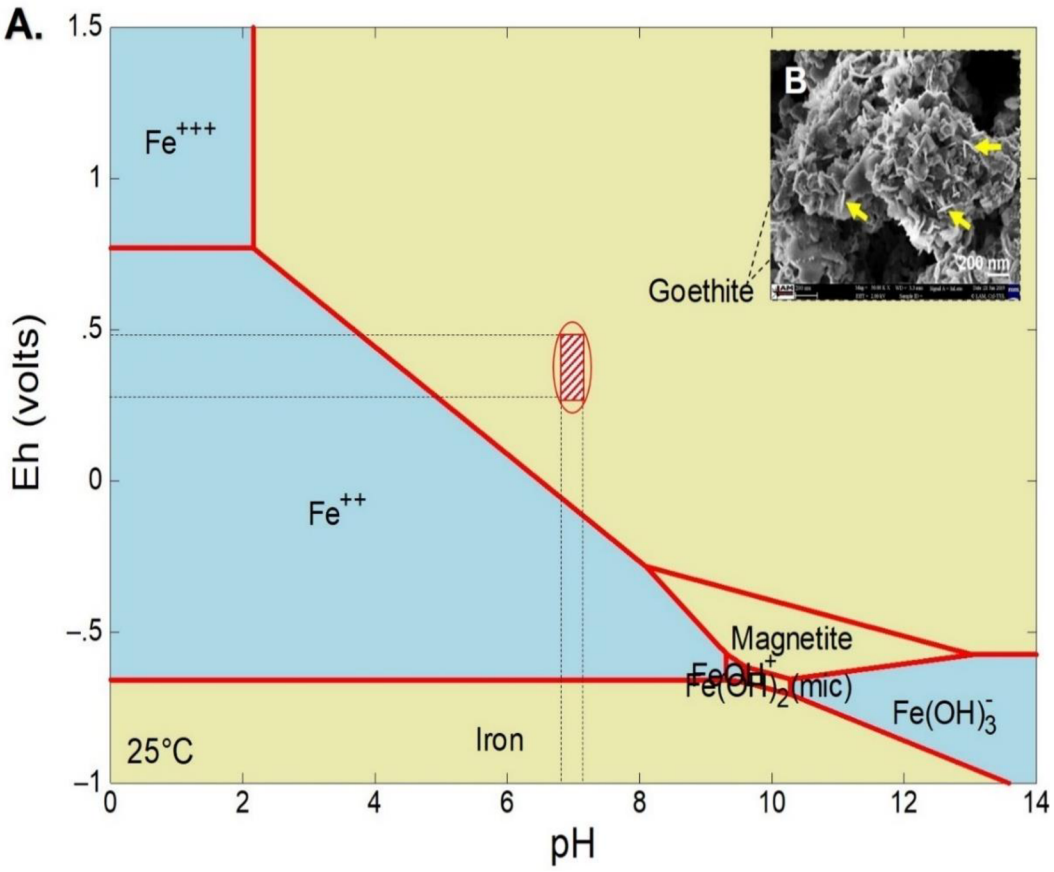

Figure 6. (A) Eh–pH diagram of 100 mg/L pristine nZVI at 25°C. Different color of the regions represents the solubility of its Fe components: brown color-solid; blue color-liquid, and gas phases; in its Fe–H_2O thermodynamic system. The *x* axis shows the pH values, the *y* axis as the redox potential (Eh) values presented in Volts. The activity of Eh–pH solubility diagram of the Fe components was plotted without limiting the lower and upper limits of water stability. The red shaded region indicates the evolutionary state of nZVI in current study. The intersection of the lines (red circle) were intersected based on the calculated Eh–pH. (B) SEM image of nZVI showing presence of goethite as indicated by the yellow arrows.

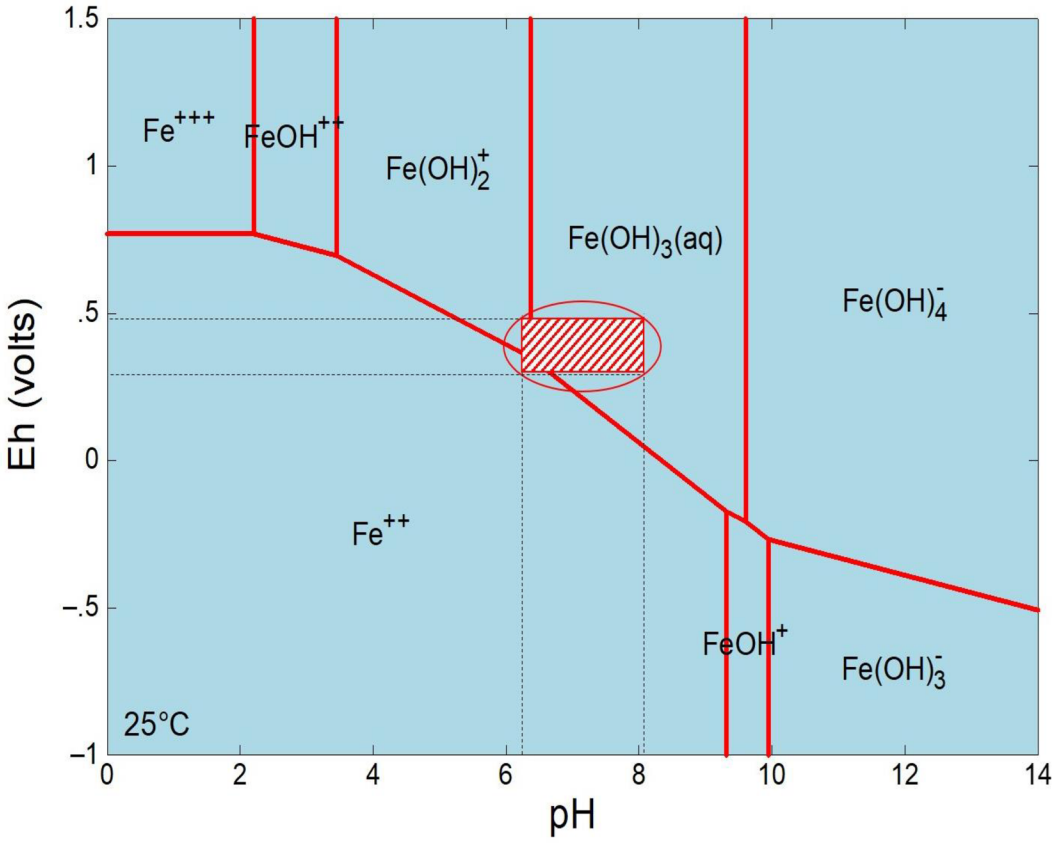

Figure 7. Eh–pH diagram of 44.5 µg/L dissolved iron at 25°C. Blue color of the regions represents the solubility of its Fe components only in liquid phase in its Fe–H_2O thermodynamic system. The *x* axis shows the pH values, the *y* axis as the redox potential (Eh) values presented in Volts. The activity Eh–pH solubility diagram of the Fe components was plotted without limiting the lower and upper limits of water stability. The red shaded region indicates the evolutionary state of dissolved iron dispersed in exposure medium. The intersection of the lines (red circle) was intersected based on the calculated Eh–pH. Such evolutionary of the iron species could be explained by the lowest pH which dissolved iron has exhibited in the experiment, that Fe may be actively hydrated into $Fe(OH)_3$ when dispersed in water, it may seemed that the stability of Fe^{2+} and $Fe(OH)_2^+$ are rather unstable in the dissolved iron system since, the final Eh–pH values lie at the borders of these Fe^{2+} and $Fe(OH)_2^+$.

4.3 Physiological effect of nZVI and dissolved iron on *P. putida*

4.3.1 nZVI and dissolved iron affect cell morphology but not viability

Overall, the surface of the *P. putida* cells was clean and smooth in the control samples (without nZVI; **Figure 8A**–**Figure 8**C), while particles were attached to the cell surface up to 3 h and later showed lower accumulation on the cells in the nZVI samples (**Figure 8D–Figure 8F**), a result that is comparable to that of the previous investigation (Kotchaplai et al., 2017). Notably, cells treated with dissolved iron formed shorter rods after 24 h (**Figure 8I**) than cells in the initial sample (**Figure 8G**).

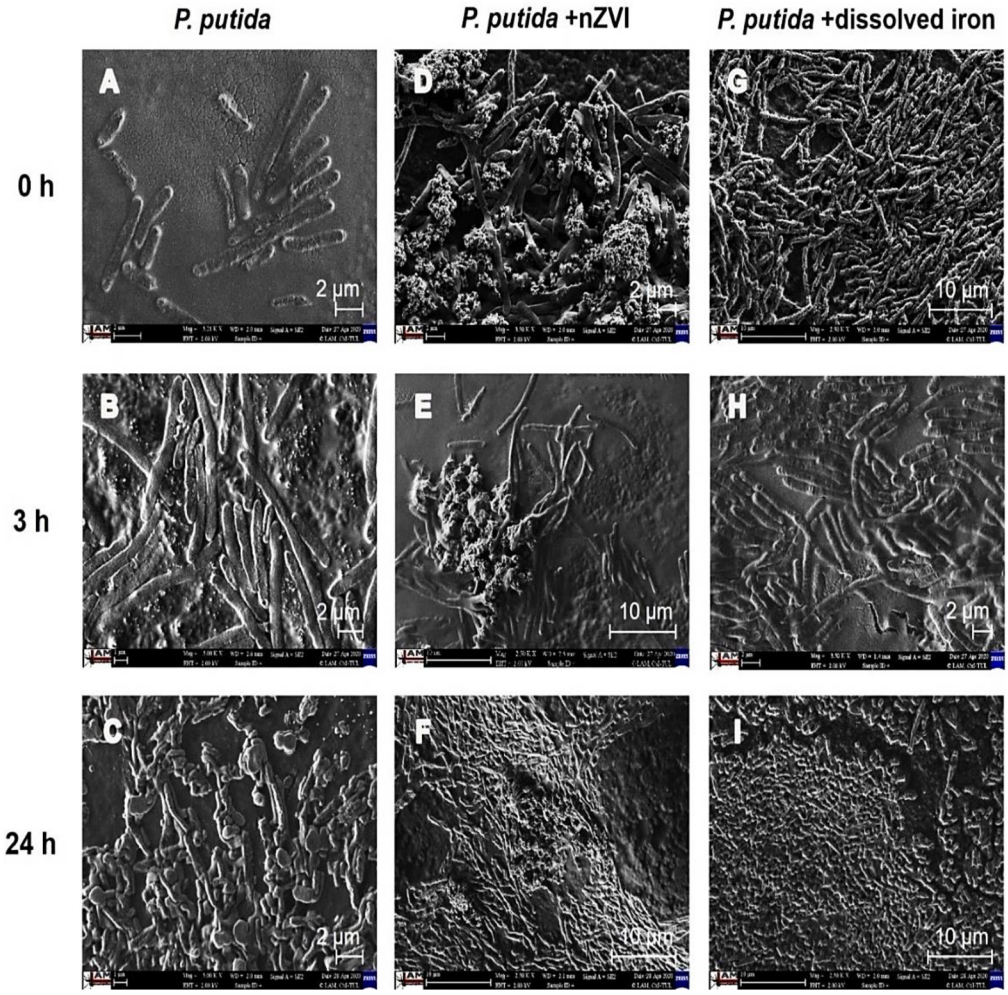

Figure 8. Scanning electron microscopy (SEM) imaging of P. putida treated with nZVI and dissolved iron at 0, 3 and 24 h in exposure medium. Negative control was (A–C) P. putida:

untreated exposure medium contains only P. putida. The control was compared to two respective treatment flasks which were (D–F) P. putida + nZVI: contains both the P. putida and nZVI in exposure medium, (G–I) P. putida + dissolved iron: contains both the P. putida and total dissolved iron obtained by nZVI dissociation in exposure medium up to 24 h. Scale bar = as indicated in the pictures.

This observation was also in agreement with the epifluorescence microscopy results, where shorter rods were clearly visible and sometimes displayed multiple mini-sectors marking the divisions between the tails of the colony edges (**Figure 9K–L**, indicated by the arrow). The nZVI treatment caused an increased number of elongated cells after 6 h (**Figure 9G**), which were at least twice the diameter compared to cells in the initial culture (**Figure 9E**).

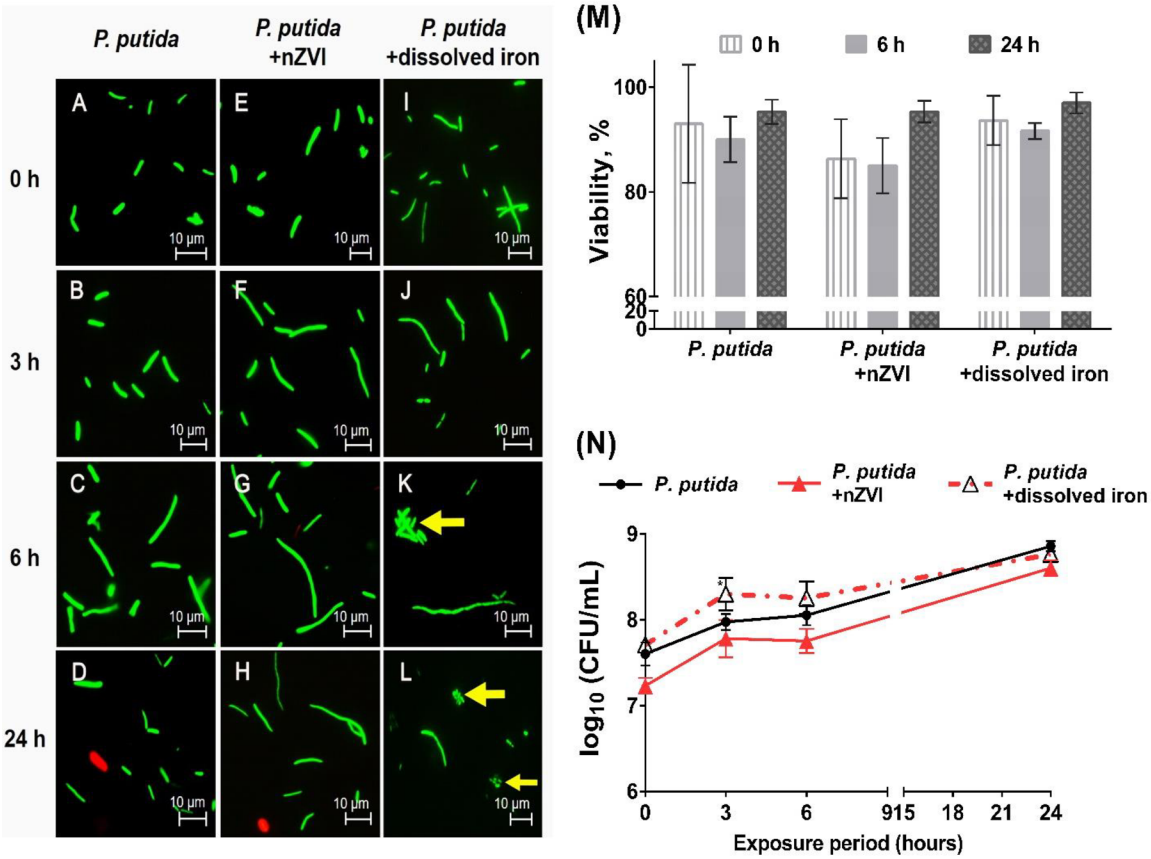

Figure 9. Viability effect and morphological changes of *P. putida* treated with nZVI and dissolved iron at 0, 3, 6, and 24 h. (A–L) Live and dead cells imaging of *P. putida* stained with SYTO9 (green) and propidium iodide (red). Yellow arrows indicate smaller cells after exposure to dissolved iron. Scale bar: 10 µm. (M) Total viable cell count determined using

fluorescence microscopy based on total count of 300 individual cells. (N) Colony forming units (CFUs) of bacteria (mean ± SD; n = 3).

A previous report showed that repetitive nZVI exposure (up to 3 cycles) induced the formation of small bacteria colonies and more rigid cells, however did not refer about the cell length (Kotchaplai et al., 2017). Comparing the physicochemical parameters in different treatments, we could determine the baseline of stress level to further explain the changes in cell morphology. Specifically, the overall pH in the exposure medium containing *P. putida* and dissolved iron was distinctly lower than other treatments. To access the potential effect of lower pH on cell morphology, the original exposure medium of pH 7.1 was acidified to pH 6.5 (as detected in the medium with dissolved iron), and then *P. putida* was again exposed for 6 and 24 h. No changes in the cell morphology were found (**Figure 10**). Transcriptomics results related to cell morphology are discussed below in the section **4.4**.

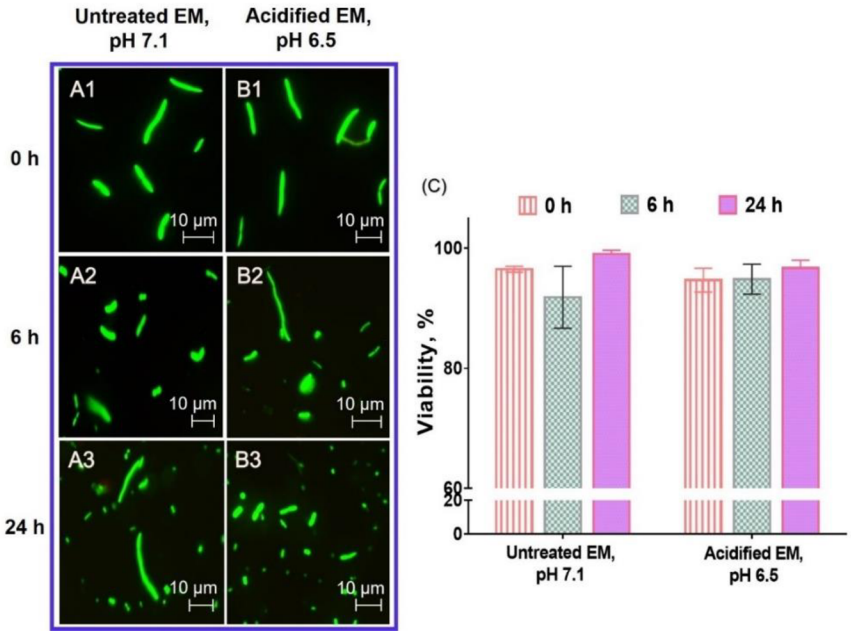

Figure 10. Viability effect and morphological changes of *P. putida* in response to reduced pH condition at 0, 6 and 24 h exposed in exposure medium. (A–C) Live & dead cell imaging of *P. putida* stained with SYTO9 (green) and propidium iodide (PI, red). (A) Untreated EM, pH 7.1: EM sampled from local reservoir without pH adjustment, (B) Acidified EM, pH 6.5: Sampled EM and pH was then adjusted by hydrochloric acid, Scale bar = as indicated in the pictures. (C) Total viable fluorescence, determined by fluorescence staining (SYTO9/PI) and

counting using fluorescence microscopy based on total fluorescence count of 300 individual cells. Value was expressed in viability percentage (mean ± SD; n = 2). EM denotes exposure medium sourced from natural reservoir water.

Viability (SYTO9/propidium iodide [PI] staining) and bacterial CFU count showed overall similar abundance profiles (**Figure 9M, N, Figure 10C**). Although the initial bacterial CFU counts increased following both the nZVI and dissolved iron treatments from 0 to 3 h, there was an overall reduction in cell numbers at 6 h, especially under nZVI treatment, which slightly reduced cell viability to 85% (SYTO9/PI). Previous studies have shown that the toxicity of the frequently used NPs, such as $AgNO_3$ or ZnO, was mostly caused by the release of metal ions into the aqueous medium (Kittler et al., 2010; Xia et al., 2008). However, dissolved iron treatment in our system did not substantially reduce the bacterial CFU and viability count (SYTO9/PI), which is consistent with previous results when *E. coli* was exposed to 100 mg/L Fe^{2+} under aerobic conditions (Kotchaplai et al., 2017). However, another study performed under anaerobic conditions showed significant inactivation of *E. coli* after treatment with 5.6 mg/L of Fe^{2+} (Lee et al., 2008). Cell numbers in all exposure conditions recovered to equivalent to initial values after 24 h, with viability counts (SYTO9/PI 16 staining) showing 95%–97% cell viability and CFU counts ranging between 8.6 and 8.9 $\log_{10}$ CFU/mL.

4.4 Transcriptomic response of *P. putida* to nZVI and dissolved iron

4.4.1 Performance evaluation of different RNA extraction methods

Eight different extraction protocols have been compared including on-column and phenol-chloroform extractions. RNA extraction by the phenol-chloroform method was able to recover both small and large fractions of RNA (**Figure 11A–D**) while RNA extraction using most of the commercial column kits were often unable to elute both the RNA types in a single elution (**Figure 11E–H**). Phenol extraction using RNAzol and on-column extraction using Bioline ISOLATE II RNA mini kit exhibited the highest extraction efficiency with the RNA integrity number (RIN^e) and RNA concentrations shown in **Figure 11**. Each of these extraction methods (RNAzol and Bioline RNA mini) in general yield a similar RIN^e value in comparison to the

untreated control and nZVI spiked samples which can be seen in their RIN^e from RNAzol extraction ($RIN_{control}$: 7.7; RIN_{nZVI}: 7.9), (**Figure 11C**) and RIN^e from Bioline ISOLATE II RNA mini kit ($RIN_{control}$: 9.0; RIN_{nZVI}: 8.9), (**Figure 11G**). In general, Bioline ISOLATE II RNA mini kit has been chosen for our following analysis of the *P. putida*-nZVI spiked

The RNA extraction efficiency by Bioline ISOLATE II RNA mini kit isolated from control, dissolved iron and nZVI spiked samples is shown in **Figure 12A**. The representative electropherogram peaks of the control, dissolved iron and nZVI clearly showed the intact 16S and 23S peaks (**Figure 12C–E**). Based on our experience, optimizing a suitable RNA extraction method for such difficult samples could be a daunting process at the beginning, especially when the information on the sample/organisms are still scarce. The consistency of the RIN^e obtained is important when selecting a suitable extraction assay fitting to the biological properties of the samples, especially when working with many treatment conditions in parallel and a huge number of samples.

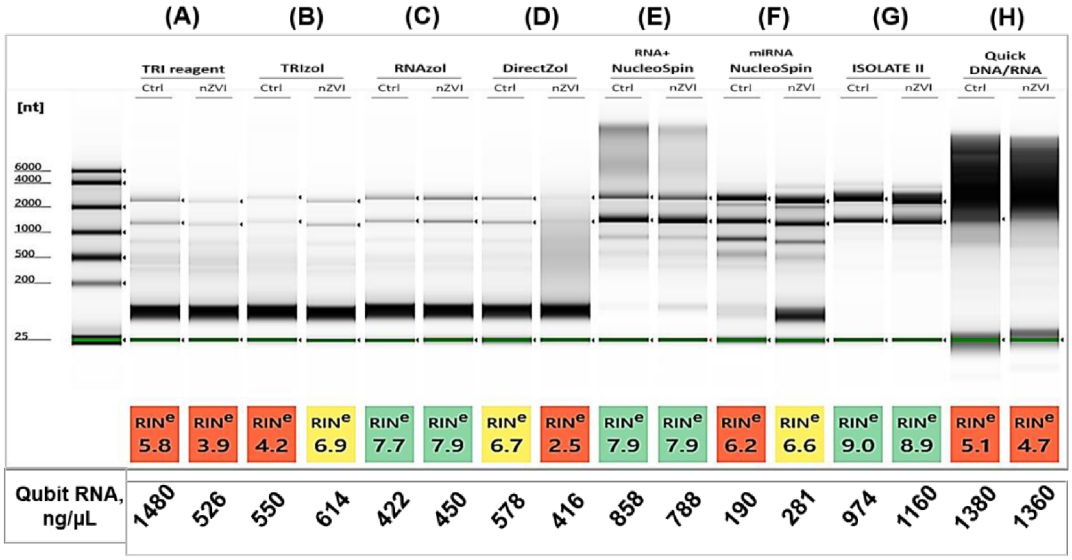

Figure 11. Comparison of RNA extraction methods performed on *P. putida*-nZVI samples in carbonate buffer (pH 8.0) on a TapeStation system based on RNA integrity number (RIN^e) and RNA concentrations are shown in the bottom line. Ctrl: condition without nZVI, nZVI: with nZVI. Different RNA extraction methods used were: (A) TRI reagent, (B) TRIzol, (C)

RNAzol, (D) DirectZol, (E) RNA Plus NucleoSpin, (F) miRNA NucleoSpin, (G) ISOLATE II, (H) Quick DNA/RNA

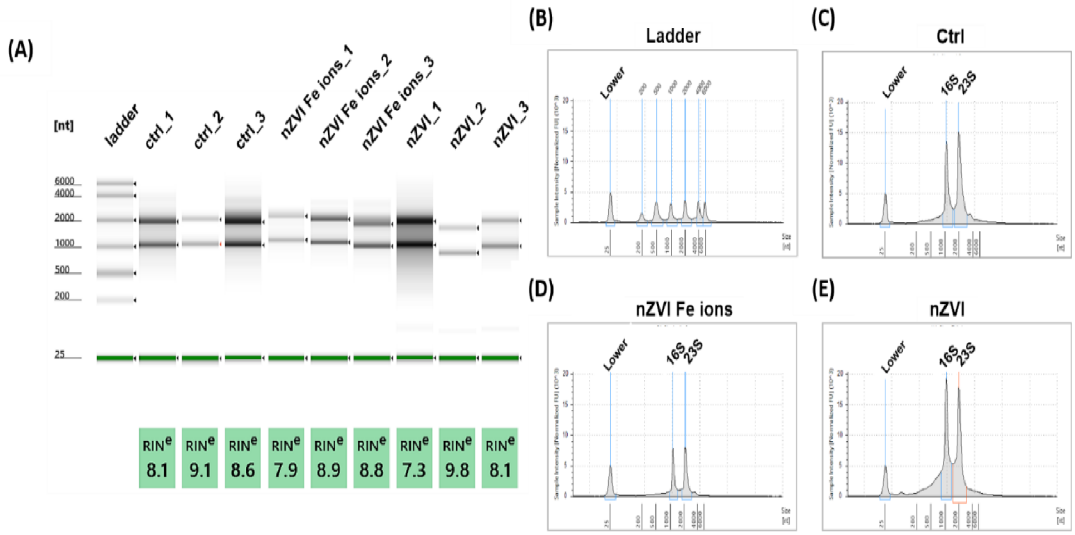

Figure 12. RNA integrity numbers of all isolated RNA from *P. putida* samples exposed to nZVI Fe ions and nZVI compared on a TapeStation system (A), and electropherograms of rRNA peaks of RNA ladder (B), control (C), nZVI Fe ions (D), nZVI (E) using Bioline ISOLATE II RNA mini kit

4.4.2 Clustering of transcriptional data

When the cells were exposed to nZVI, a higher number of DEGs were identified at the earlier time point of 6 h (1,579 genes) compared to the later time point of 24 h (945 genes), indicating the changes in transcriptomic response during the exposure to nZVI. Meanwhile, dissolved iron changed the expression of 3,839 genes after 24 h. These groups overlapped considerably, sharing 390 mutual genes among the three conditions tested (**Figure 13A**). A similar trend was reported in a previous study for *Pseudomonas aeruginosa* when 3.12 mg/L of ionic Ag+ caused 2,458 DEGs, whereas Ag NPs affected 1,599 DEGs after 6 h of exposure (Singh et al., 2019). These results suggest that ion-specific exposure generally leads to a much more pronounced response in gene expression level than particle-specific exposure, findings that are in agreement with previous studies that involved physiological, morphological, and viability responses (Moore et al., 2017; Singh et al., 2019), where ion-specific treatment revealed mechanistic pathways that were distinct from those upregulated by NP exposure (Guo et al., 2020; Piersanti et al., 2021).

A high proportion of DEGs fell under unknown categories encoding hypothetical proteins, and these were the most pronounced DEGs in all exposure conditions. In a previous study where sulfate-reducing bacterium were exposed to 50 and 250 mg/L of CuO NPs, a similar observation was also reported; huge numbers of hypothetical proteins were reported to be differentially expressed (Chen et al., 2019). Principal component analysis (PCA) of the RNA-seq data confirmed the gene expression consistency among biological replicates and its clear dissimilarities between treatment profiles and exposure hours (**Figure 13B**). The total number of RNA sequencing raw reads from each biological sample can be found in **Table 5**. In agreement with the PCA map, three major clusters (C1, C2, and C3) were identified in the heatmap (**Figure 14**). *P. putida* exposed to dissolved iron exhibited a completely different expression profile compared to *P. putida* exposed to nZVI. The DEGs were mostly associated with flagellar assembly (*flgH, flgF, flgG, flgI, flgJ, flgK, flgA, flgL, flgE, flgC, flgD, and fliS*), approximately 50% of the top 30 DEGs in the heatmap, as well as genes involved in the tricarboxylic acid (TCA) cycle (*sdhA, sdhB, sdhC, and sdhD*)

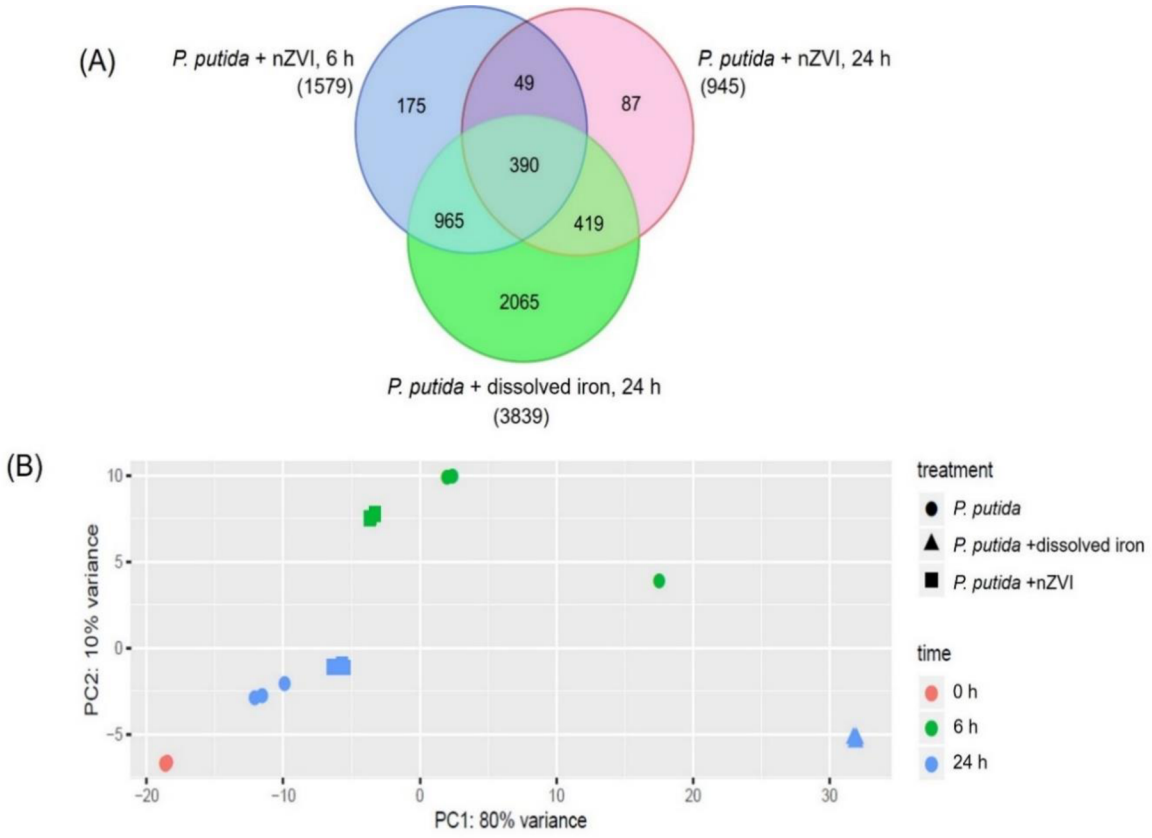

Figure 13. Expression profiling of *P. putida*. (A) Venn diagram of DEGs in *P. putida* + nZVI and *P. putida* + dissolved iron conditions compared to control at 6 and 24 h. Each treatment was compared to the *P. putida* control. (B) Principal component analysis of the RNA-seq data. The first principal component (PC1) is shown on the *x* axis, whereas the second principal component (PC2) is shown on the *y* axis. Treatment types are represented by different shapes, and exposure hours are represented by different colors.

Table 5. Total number of RNA sequencing reads obtained from respective sample

Sample, exposure period	Replicate	Total clean reads (million)	Total mapped reads (%)
P. putida -nanoparticle free (0 h)	1	23.04	75.62
	2	25.35	75.56
	3	21.88	75.63
P. putida -nanoparticle free (6 h)	1	24.68	75.46
	2	24.63	76.37
	3	27.36	75.10
P. putida -nanoparticle free (24 h)	1	24.89	74.36
	2	21.89	74.73
	3	30.27	77.12
P. putida exposed to 100 mg/L nZVI (6 h)	1	27.77	74.63
	2	24.97	74.60
	3	25.88	74.64
P. putida exposed to 100 mg/L nZVI (24 h)	1	26.65	78.25
	2	26.08	74.97
	3	25.41	76.73
P. putida exposed to 44.5 µg/L dissolved iron (24 h)	1	30.30	79.45
	2	29.70	79.69
	3	23.51	78.51

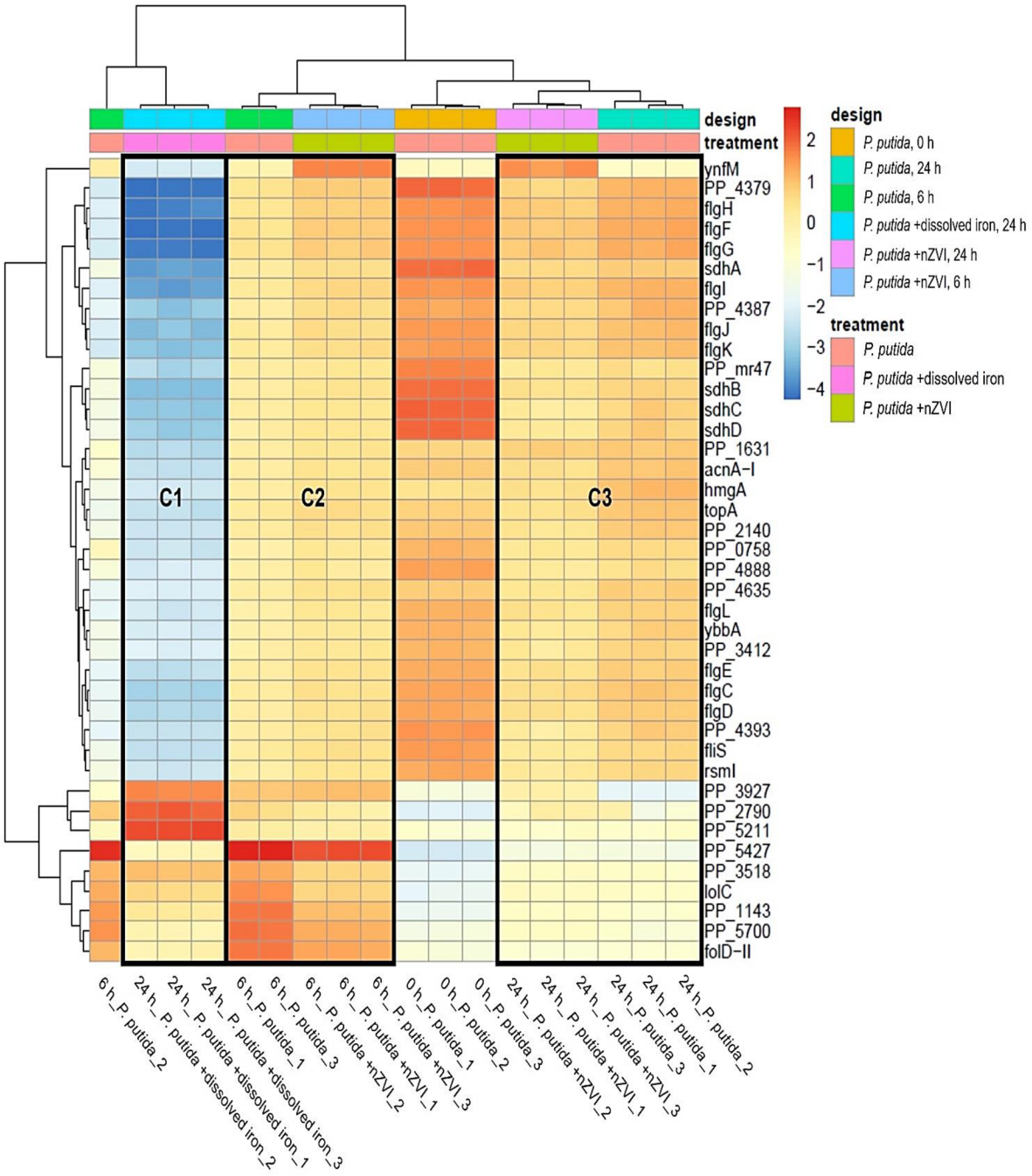

Figure 14. Heatmap of the top 30 DEGs in different exposure conditions. Hierarchical clustering of genes was based on the $\log_2$-fold change, and the adjusted P-value was based on the 95% confidence interval. Cluster C1 contained the samples exclusively from *P. putida* in dissolved iron treatment at 24 h; cluster C2 represented the *P. putida* in nZVI treatment at 6 h, whereas cluster C3 consisted of the samples of *P. putida* in nZVI at 24 h. Relative gene expression is indicated by the color scales: elevated gene expression higher than zero indicates upregulation in control (red), reduced gene expression, shown in blue, less than

zero indicates upregulation in treatment conditions (*P. putida* with nZVI or dissolved iron). Control contains *P. putida* only. Darker hue of the color indicates higher gene expression value.

4.4.3 Dissolved iron downregulates genes involved in flagellar assembly and iron transportation functions

Genes encoding in the following metabolic pathways were mostly downregulated in the dissolved iron system: flagellar assembly (16 genes, at least 3.4-fold change compared to control), iron transporters (4 genes) and iron regulation (2 genes), quorum sensing (7 genes), bacterial chemotaxis (4 genes), and two-component system, partly related to transmembrane entry and flagellar system (3 genes) (**Figure 15, Table 6**). Of these pathways, most downregulated genes were involved in heme–iron transportation/binding, electron transfer, transmembrane efflux pump function in ionic exchange, and cell motility. These downregulation patterns were similar to those detected in previous exposure studies using nZVI and CuO NPs (Chen et al., 2019; Fajardo et al., 2013). In addition, a disruptive motility had been demonstrated in *P. putida* exposed to nZVI, characterized by the abrupt changes and more frequent turning directions (Ortega-Calvo et al., 2016). Environmental stressors, including surplus of dissolved iron, could induce changes in gene transcription to control the influx of heavy metal ions to minimize unwanted osmolality pressure/oxidative stress (Fernández-Piñar et al., 2008; Liu et al., 2015; McCarter, 2006).

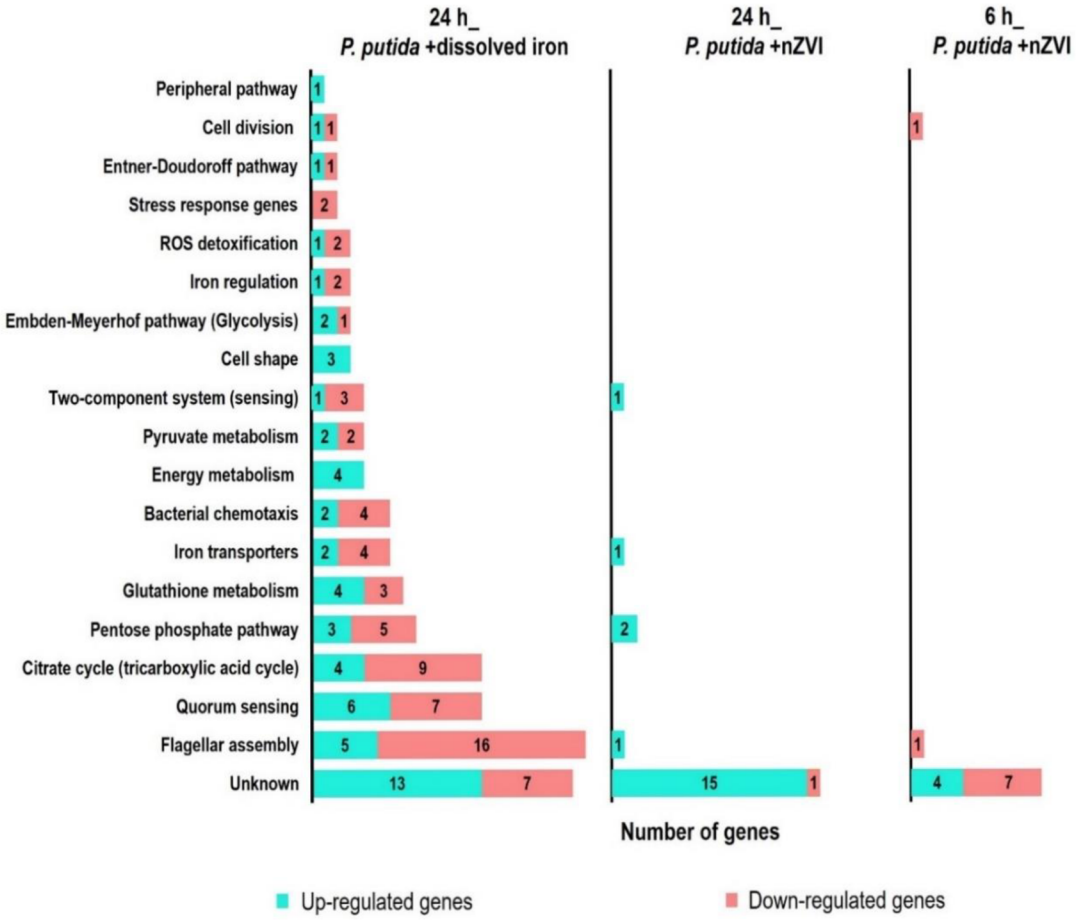

Figure 15. An overview numbers of differentially expressed genes (log_2 [fold change] ≥ 1.0 or ≤ -1.0) ($P < 0.05$) in *P. putida* exposed to nZVI or dissolved iron versus the *P. putida* control classified by metabolic pathways and functional groups using both KEGG and BioCyc databases (data from **Table 6**).

Table 6. A summary of genes grouped by metabolic pathways and by functional classification using KEGG and BioCyc databases, identified as differentially expressed [$\log_2$(fold change) ≥ 1.0 or ≤ −1.0], ($p < 0.05$) upon *P. putida* exposure treatment with (*P. putida* + nZVI) or (*P. putida* + dissolved iron) respectively at 6 h and 24 h. Fold change was calculated relative to unexposed control (Love et al., 2014). Elevated gene expression higher than zero indicates up-regulation in control condition (blue), reduced gene expression less than zero indicates up-regulation in treatment conditions in either (*P. putida* + nZVI) or (*P. putida* + dissolved iron), (red). NOTE: control = *P. putida* without nanoparticle exposure. Color with a darker hue indicates higher gene expression value in the treatments condition.

KEGG module/ functional classification	Locus tag	Gene name	Function	$\log_2$ (fold change) gene expression by treatment type		
				6 h	24 h	
				P. putida + nZVI	*P. putida* + nZVI	*P. putida* + dissolved iron
Two-component system	PP_3585	*mdtA*	transmembrane transporter activity	-	-	1.24
	PP_5320	*phoB*	phosphate ion transport	-	-	1.08
	PP_1430		proteolysis/ protein binding	-	-	−1.30
	PP_1437		signal transduction/heavy metal sensor	-	-	2.52
	PP_2664		transferase activity	-	−1.58	-
Quorum sensing	PP_3080	*aroF-II*	aromatic amino acid family biosynthetic process/catalytic activity	-	-	1.29
	PP_4453	*gsiA*	peptide transport/ATPase activity/ ATP binding	-	-	−1.35
	PP_4455	*gsiC*	transmembrane transport	-	-	−1.19
	PP_4894	*hfq*	RNA binding	-	-	−1.45
	PP_0441	*secE*	intracellular protein transport/protein secretion	-	-	−2.30
	PP_1486	*ydcS*	polyamine transport and binding	-	-	1.99
	PP_1484	*ydcT*	transmembrane transport/ATPase activity/ ATP binding	-	-	1.25
	PP_1483	*ydcU*	transmembrane transport	-	-	1.73
	PP_1482	*ydcV*		-	-	1.71
	PP_0119	-	DNA-binding transcription factor activity/ zinc uptake	-	-	−1.59
	PP_1722	-	ATPase activity/ATP binding	-	-	1.70
	PP_2748	-		-	-	−1.61

	PP_3220	-		-	-	1.02
Iron transporters	PP_2594	*fatD*	transmembrane transporter activity	-	−1.02	-
	PP_5196	*fbpA*	Ferric binding protein	-	-	1.17
	PP_0272	-	siderophore transport/signaling receptor activity	-	-	−1.07
	PP_0535	-		-	-	−1.29
	PP_1847	-		-	-	1.32
	PP_2417	-	transmembrane transporter activity	-	-	1.19
	PP_5195	-	transmembrane transport	-	-	1.14
Iron regulation	PP_0433	*erpA*	iron-sulfur cluster binding/ protein maturation by iron-sulfur cluster transfer	-	-	3.00
	PP_4730	*fur*	Ferric uptake regulator family	-	-	1.19
	PP_5212	-	oxidation-reduction process/iron-sulfur cluster binding/electron transfer activity	-	-	−1.22
Stress response genes	PP_0089	*osmC*	response to oxidative stress/peroxidase activity	-	-	1.23
	PP_2877	*yfeH*	osmotic pressure-regulated transporter	-	-	1.07
Glutathione metabolism	PP_4659	*ggt*	glutathione catabolic process/glutathione hydrolase activity	-	-	1.43
	PP_1821	-	glutathione transferase	-	-	2.89
	PP_4011	*icd*	tricarboxylic acid cycle/isocitrate dehydrogenase (NADP+) activity /magnesium ion binding	-	-	−1.17
	PP_4012	*idh*	tricarboxylic acid cycle/isocitrate dehydrogenase (NADP+) activity	-	-	−1.17
	PP_1022	*zwfA*	glucose–6–phosphate dehydrogenase activity/Pentose phosphate pathway	-	-	−1.46
	PP_1686	-	response to oxidative stress/glutathione peroxidase activity	-	-	1.58
	PP_5211	-	Tricarboxylic acid cycle/isocitrate dehydrogenase (NADP+) activity	-	-	−3.29
Peripheral pathway	PP_3378	*kguK*	phosphotransferase activity	-	-	−1.26
Pentose phosphate pathway	PP_1777	*cpsG*	magnesium ion binding/phosphotransferases	-	−1.34	-
	PP_1261	*ghrB*	oxidation-reduction process	-	-	−1.79

	PP_0722	*prs*	magnesium ion binding/ribose phosphate diphosphokinase activity	-	-	−1.71
	PP_2458	*rbsK*	phosphotransferase activity/kinase activity	-	-	1.08
	PP_5150	*rpiA*	ribose–5–phosphate isomerase activity	-	−1.50	1.13
	PP_2168	*tal*	pentose-phosphate shunt/catalytic activity	-	-	1.58
	PP_4300	*ttuD*	Transferases activity	-	-	2.22
	PP_1022	*zwfA*	glucose–6–phosphate dehydrogenase activity	-	-	−1.46
	PP_3443	-	oxidation-reduction process	-	-	1.04
Embden–Meyerhof pathway (Glycolysis)	PP_1612	*eno*	phosphopyruvate hydratase activity/magnesium ion binding	-	-	−1.24
	PP_4301	*pyk*	pyruvate kinase activity/magnesium and potassium ion binding	-	-	1.85
	PP_1362	*pykA*		-	-	−1.10
Entner–Doudoroff pathway	PP_1024	*eda*	catalytic activity/lyase activity	-	-	−1.01
	PP_1021	*hexR*	carbohydrate derivative binding/DNA-binding transcription factor activity	-	-	1.22
Citrate cycle (tricarboxylic acid cycle)	PP_2112	*acnA-I*	Carbon-oxygen lyases	-	-	3.50
	PP_0944	*fumC-I*	fumarate metabolic process/catalytic activity	-	-	1.35
	PP_0356	*glcB*	catalytic activity/malate synthase activity	-	-	−1.15
	PP_4011	*icd*	isocitrate dehydrogenase (NADP+) activity/magnesium ion binding/Glutathione metabolism	-	-	−1.17
	PP_4012	*idh*	isocitrate dehydrogenase (NADP+) activity/Glutathione metabolism	-	-	−1.17
	PP_5366	*lpd*	cell redox homeostasis/electron transfer activity	-	-	−1.16
	PP_4187	*lpdG*		-	-	1.00
	PP_0751	*mqo–I*	malate dehydrogenase (quinone) activity	-	-	1.16
	PP_4191	*sdhA*	electron transport chain	-	-	4.69
	PP_4190	*sdhB*	iron-sulfur cluster binding	-	-	4.26
	PP_4193	*sdhC*	succinate dehydrogenase activity/electron transfer activity	-	-	4.51
	PP_4192	*sdhD*	oxidoreductase activity/succinate dehydrogenase activity/heme binding	-	-	4.63
	PP_4189	*sucA*	oxoglutarate dehydrogenase (succinyl-transferring) activity	-	-	2.30

Pyruvate metabolism	PP_3766	*gloA*	Lactoyl glutathione lyase activity/ metal ion binding	-	-	1.53
	PP_4144	*gloB*	Hydroxyacyl glutathione hydrolase activity	-	-	−1.53
	PP_0774	*pta*	phosphate acetyltransferase activity	-	-	1.12
	PP_1389	-	catalytic activity	-	-	−1.06
energy metabolism	PP_5419	*atpB*	ATP synthesis coupled proton transport	-	-	−1.10
	PP_5412	*atpC*		-	-	−1.16
	PP_541	*atpD*	ATP synthesis coupled proton transport/ATP metabolic process	-	-	−1.11
	PP_0847	*fdx*	2 iron, 2 sulfur cluster binding/ iron–sulfur cluster binding/electron transfer activity	-	-	−1.05
bacterial chemotaxis	PP_4392	*cheR*	-	-	-	2.87
	PP_4340	*cheY*	Response regulator receiver domain	-	-	−1.21
	PP_2454	*rbsB*	periplasmic binding protein domain/Saccharide, polyol, lipid and ribose transporter	-	-	2.20
	PP_2111	-	transmembrane signaling receptor activity	-	-	3.06
	PP_3414	-		-	-	−1.33
	PP_4393	-	signaling and cellular processes	-	-	3.93
flagellar assembly	PP_4378	*fliC*	bacterial-type flagellum filament	-	-	2.92
	PP_4370	*fliE*	Flagellar hook-basal body complex protein FliE.	-	-	1.19
	PP_4365	*fliJ*	motor activity	-	-	−1.02
	PP_4355	*fliP*	protein secretion	-	-	−1.59
	PP_4354	*fliQ*	integral component of membrane	-	−1.12	−2.55
	PP_4353	*fliR*	protein targeting/integral component of membrane	1.18	-	−1.00
	PP_4375	*fliS*	-	-	-	3.37
	PP_4374	*fliT*	bacterial-type flagellum-dependent cell motility	-	-	−2.11
	PP_0227	*fliY*	ligand-gated ion channel activity/Bacterial extracellular solute-binding proteins	-	-	1.59
	PP_4391	*flgB*	Flagella basal body rod protein	-	-	1.46
	PP_4390	*flgC*		-	-	4.78
	PP_4389	*flgD*	Flagellar hook capping protein	-	-	4.20
	PP_4388	*flgE*		-	-	3.92

	PP_4386	*flgF*	Flagella basal body rod protein	-	-	6.33
	PP_4385	*flgG*	flagellar hook-basal body protein	-	-	6.22
	PP_4384	*flgH*	bacterial-type flagellum basal body, motor activity	-	-	6.25
	PP_4383	*flgI*		-	-	5.14
	PP_4382	*flgJ*	hydrolase activity/flagellar rod assembly protein	-	-	4.55
	PP_4381	*flgK*	Flagella basal body rod protein	-	-	4.29
	PP_4380	*flgL*	Flagellar assembly Rod and hook proteins	-	-	3.43
	PP_4905	*motA*	flagellar motor stator protein	-	-	1.24
ROS Detoxification	PP_0115	*katE*	hydrogen peroxide catabolic process/response to oxidative stress/heme binding	-	-	1.79
	PP_0946	*sodA*	superoxide dismutase activity/metal ion binding	-	-	1.40
	PP_0915	*sodB*		-	-	−1.14
cell division	PP_1613	*ftsB*	Septum formation initiator	-	-	1.24
	PP_1732	*minE*	regulation of division septum assembly/ cell division	1.00	-	-
	PP_2142	*sulA*	negative regulation of cell division/SOS response	-	-	−1.88
cell shape	PP_0933	*mreB*	Cell morphogenesis/Bacterial cell shape determinant MreB	-	-	−1.60
	PP_0934	*mreC*	regulation of cell shape/rod shape-determining protein MreC	-	-	−1.54
	PP_0935	*mreD*	regulation of cell shape	-	-	−1.11
Unknown	PP_1305	*Imm*	Toxic substance binding	2.97	-	-
	PP_2681	*pqqD-II*	Quinone binding	-	−3.64	−3.08
	PP_1320	*sspA*	stringent starvation protein A	-	-	3.32
	PP_1321	*sspB*	-	-	-	3.77
	PP_5072	*ynfM*	transmembrane transporter activity	−1.78	−2.18	2.06
	PP_0758	hypothetical protein	-	-	-	3.87
	PP_1174	hypothetical protein	-	-	−1.57	-
	PP_1548	hypothetical protein	-	-	−1.53	−1.54
	PP_1928	-	-	−1.49	−1.88	-
	PP_2491	-	-	1.48	-	-
	PP_2987	hypothetical protein	-	2.38	-	-

PP_3005	hypothetical protein	-	-	−1.57	−1.80
PP_3049	hypothetical protein	-	−1.00	−4.55	−2.75
PP_3333	hypothetical protein	-	-	−1.10	−2.25
PP_3434	hypothetical protein	-	-	1.01	-
PP_3927	-	-	-	−2.05	−3.77
PP_3965	-	-	-	−1.49	−1.98
PP_4387	hypothetical protein	-	-	-	7.59
PP_4618	hypothetical protein	-	1.47	−1.13	-
PP_4816	-	integral component of membrane	−1.61	−1.20	2.02
PP_5240	-	-	-	−1.35	−2.86
PP_5430	hypothetical protein	-	1.40	−1.88	−2.02
PP_5523	hypothetical protein	-	1.44	-	−1.45
PP_5529	-	-	-	-	−2.95
PP_5541	hypothetical protein	-	-	−3.66	−3.14
PP_5549	hypothetical protein	-	-	-	2.95
PP_5691	hypothetical protein	-	1.59	-	−2.02

4.4.4 Dissolved iron activates genes in oxidative stress-related pathways, carbohydrate metabolism, and energy metabolism

The antioxidant response pathways affected by dissolved iron included ROS detoxification (one upregulated, two downregulated genes), glutathione metabolism (four upregulated, three downregulated genes), and stress response genes (all downregulated) (**Figure 15**, **Table 6**). Among the five upregulated genes, four had

dual function in both glutathione and carbohydrate metabolism (*icd, idh, zwfA, PP_5211*), and one gene was involved in the oxidative stress response (SOD subunit B [*sodB*]).

The expression of SOD and genes in the glutathione pathway is thought to be the first line of defense against oxidative stress (Arnér and Holmgren, 2000; Polle, 2001). The activation of two glutathione enzymes (glutathione peroxidase and glutathione reductase) in *P. putida* is mediated by the transcripts encoding glutathione peroxidase activity (*PP_0777* and *PP_1686*) and glutathione-disulfide reductase activity (*gor*) (Kanehisa and Goto, 2000) (**Figure 16**).

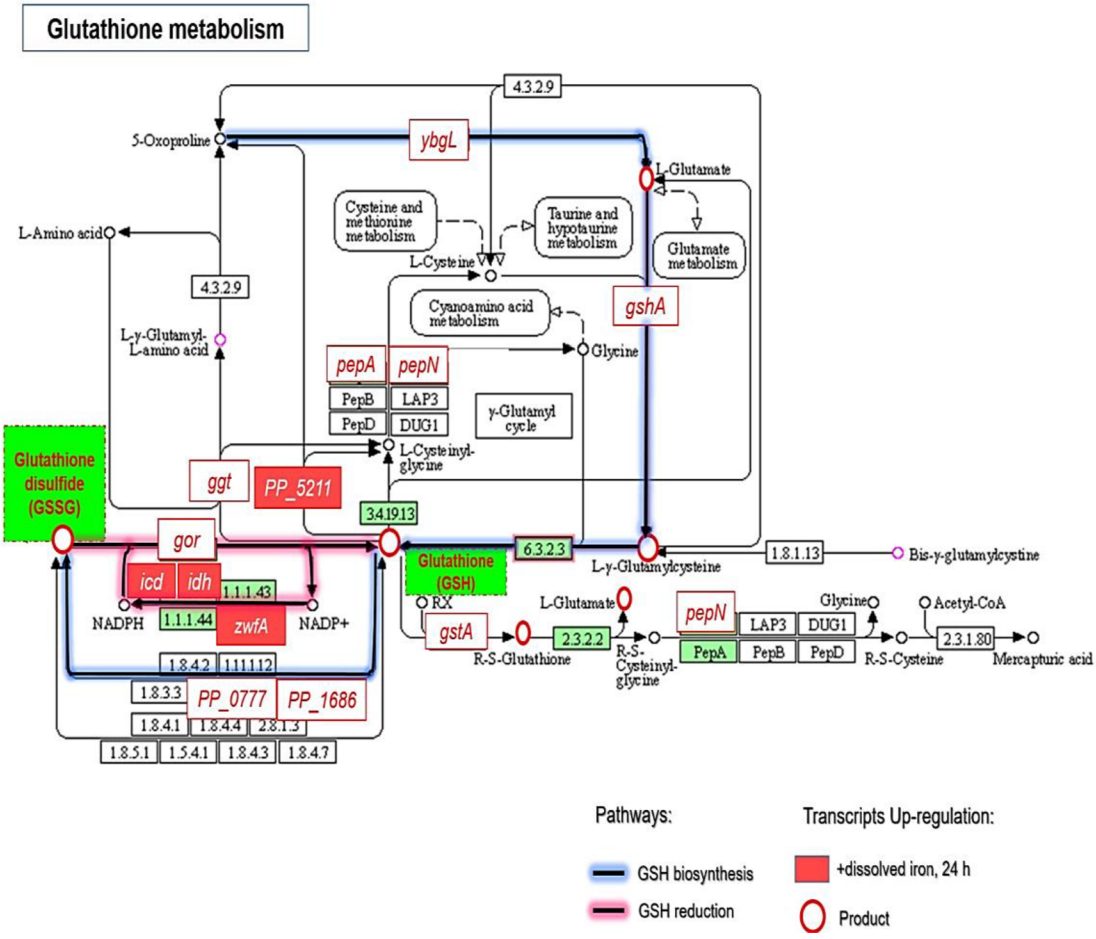

Figure 16. KEGG pathway map of *P. putida* (glutathione metabolic pathway involved the molecular interaction of various genes upon 24 h exposure in dissolved iron condition. The map was retrieved from https://www.genome.jp/kegg-bin/show_pathway?ppun00480+M00118#. The highlighted lines: (blue line) showed the direct biosynthesis pathway for glutathione (GSH) and glutathione disulfide (GSSG)

compounds; (pink line) show the reduction of GSH and NADP+, which function as antioxidants when oxidative stress is detected in cells. The red colored boxes show the up-regulation of transcripts in dissolved iron treatment. NOTE: Green boxes and map without coloring are the original version retrieved from the KEGG database.

Among these genes, *PP_1686* was downregulated in the dissolved iron system, and the regulation of other genes was either undetected or insignificant (**Table 6**). Under oxidative stress, including the stress-related to NP exposure, *P. putida* is able to dual-regulate glutathione and central carbohydrate metabolism simultaneously to route the production of essential energy fuels or reducing cofactors such as ATP, NADPH, NADH, and glucose–6–phosphate dehydrogenase (G6PDH) (Chavarría et al., 2013; Ma et al., 2011; MacLean et al., 2020; Nguyen et al., 2021; Volke et al., 2021). Carbohydrate metabolism is subdivided into the peripheral pathway, pentose phosphate (PP) shunt, glycolysis, TCA cycle, the Entner–Doudoroff (ED) pathway, and the Embden–Meyerhof–Parnas (EMP) pathway (Kanehisa and Goto, 2000). It has been reported previously that the production of these energy currencies or reducing factors is mainly mediated by the *zwfA* transcript (*PP_1022*), and that these currencies are then pumped through the PP pathway, or a combination of the ED and EMP pathways, to fuel the antioxidant defense system (glutathione) and to thwart the intracellular ROS milieu (**Figure 17**) (Meister, 1988; Nikel et al., 2021; Stincone et al., 2015; Volke et al., 2021). This theory agrees with the gene expression pattern observed in our system that transcripts from peripheral pathways (*kguK*), the PP shunt (*zwfA*), TCA cycle (*icd* and *idh*), SOD (*sodB*), glutathione metabolism (*PP_5211*), EMP pathway (*pykA* and *eno*), and ED pathway (*eda*) were highly upregulated in the dissolved iron system (**Table 6**), suggesting that the oxidative stress environment in the dissolved iron system activated stress-related genes. Similarly, the upregulation of proteins functioning in general stress responses and the TCA cycle was also detected in *Bacillus cereus* when exposed to nZVI in a previous study (Fajardo et al., 2013). All four transcripts regulated under energy metabolism, for example, *atpB*, *atpC*, and *atpD*, which function in ATP synthesis, and *fdx*, which functions in iron–sulfur binding, were upregulated in the dissolved iron system (**Figure 15**, **Table 6**). Upregulation of *atp* genes was clearly seen by the demand for ATP utilization to increase ATP production, while mitochondria is an efficient antioxidant defense

system capable of scavenging a large number of ROS (Starkov, 2008). Previous CuO NPs (Chen et al., 2019)and TiO_2 NPs (Planchon et al., 2017) exposure studies on prokaryotic models also demonstrated a similar trend regarding the increase in energy metabolism. However, energy metabolism in eukaryotic models was interrupted by exposure to TiO_2 NPs or Ag NPs (Jin et al., 2013; Ma et al., 2011).

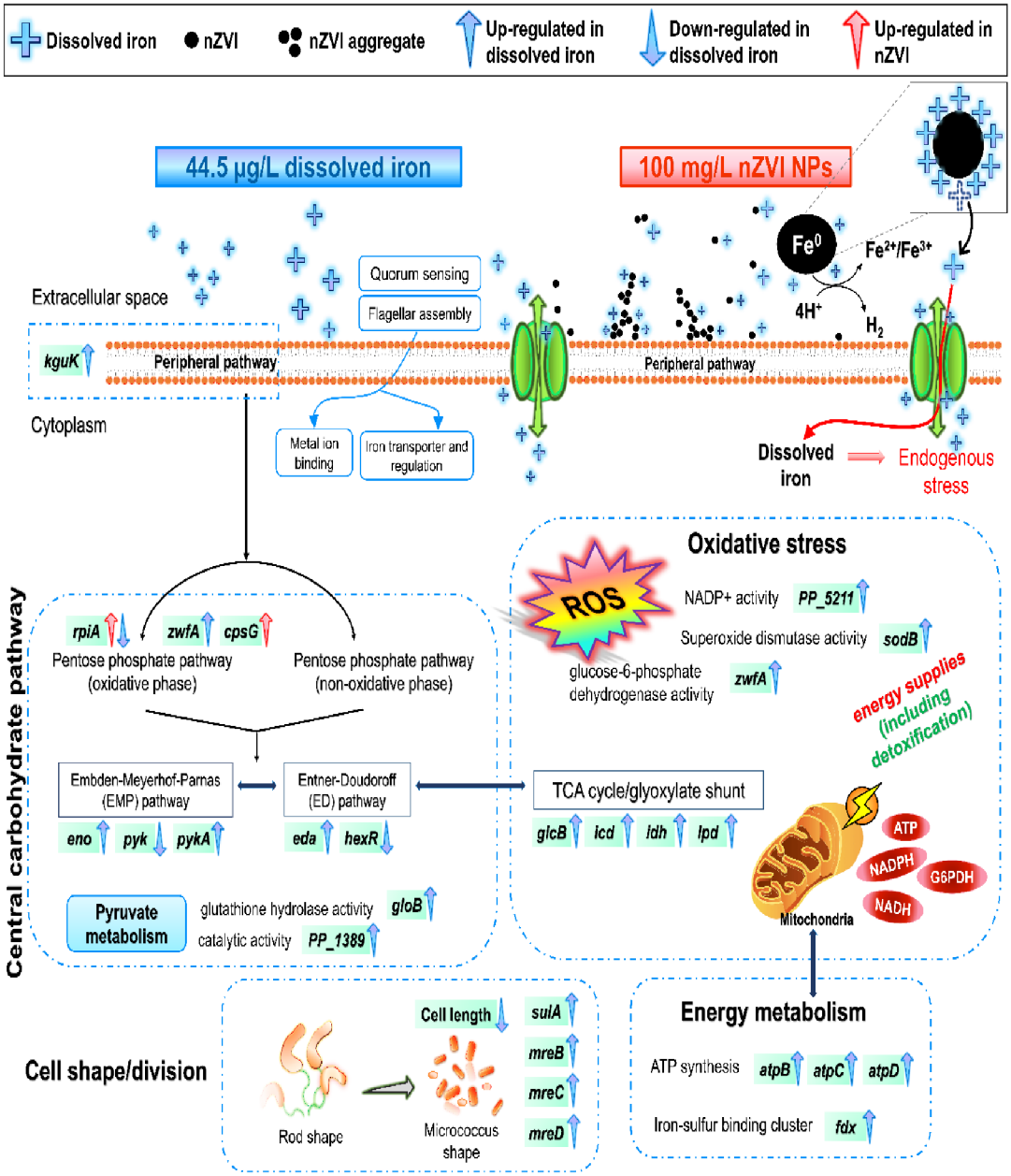

Figure 17. Metabolic pathways triggered by dissolved iron from nZVI and nZVI in *P. putida*. Colors represent different exposure conditions: (i) Blue: 44.5 µg/L dissolved iron, (ii) red:

100 mg/L nZVI. Blue and red arrows are associated with the exposed conditions. Up or down arrows indicate upregulation or downregulation of each expressed DEG.

4.4.5 Dissolved iron activates genes functioning in cell-shape determinants

All three transcripts (*mreB, mreC, and mreD*) that function in maintaining the rod shape of *P. putida* cells were highly enriched in the presence of dissolved iron (**Figure 15**, **Table 6**), resulting in the observed small phenotype of *P. putida* (**Figure 9L**) and causing the emergence of phenotypic heterogeneity. This phenomenon is a growth and survival response that occurs when *P. putida* adapts to an environment containing NPs (Chen et al., 2021; Magdanova and Goliasnaia, 2013; Schröter and Dersch, 2019). The electrostatic interactions between positively charged NPs (or their ionic forms) and negatively charged bacterial surfaces lead to their adhesion, subsequently increasing membrane fluidization and disrupting the membrane integrity (Joshi et al., 2020; Pagnout et al., 2012). In a recent study that used antibacterial bimetallic Au–Ag NPs, this phenomenon was linked to the inhibition of the *mreB* transcript in *E. coli*, which reduced the cytoskeletal strength and allowed a gradual transition from rod-shaped to spherical cells (Jena et al., 2020). However, the elevated expression of morphogenetic *mreBCD* genes observed in our study could be an adaptation strategy of *P. putida* to allow it to rebound back to its rod shape. Conversely, *P. putida* expressed a filamentous phenotype in the nZVI treatment after 6 h (**Figure 9G**). Filamentation could be caused by an inability of cells to septate during growth (Jensen and Woolfolk, 1985), which is a typical consequence of environmental stress. These phenomena have been described in previous physiological and hierarchical signaling studies (Cánovas et al., 2003; Crabbé et al., 2012; Mulakhudair et al., 2017).

4.4.6 Metabolic pathways enrichment analysis

RNA-seq has higher resolution and accuracy in identifying the low-abundance transcripts, whereas protein–protein interaction (PPI) analysis can be performed in conjunction using the co-expression data extracted from RNA-seq to predict the functional interaction of genes or proteins (Szklarczyk et al., 2018). PPI analysis

revealed a close relationship between the central carbohydrate metabolism pathway (PP shunt, glycolysis, TCA cycle) and stress-related pathways (general stress response, ROS detoxification, and glutathione metabolism) in *P. putida* (**Figure 18**). The interrelationship between *sodB*, *zwf, PP_1686*, *idh*, and *icd* may show linkages working among each of the oxidative stress challenges. Other pathways (not mentioned in **Figure 18**) are subcategorized under carbohydrate metabolism, including the ED and EMP pathways, and can be divided into oxidative and non-oxidative branches.

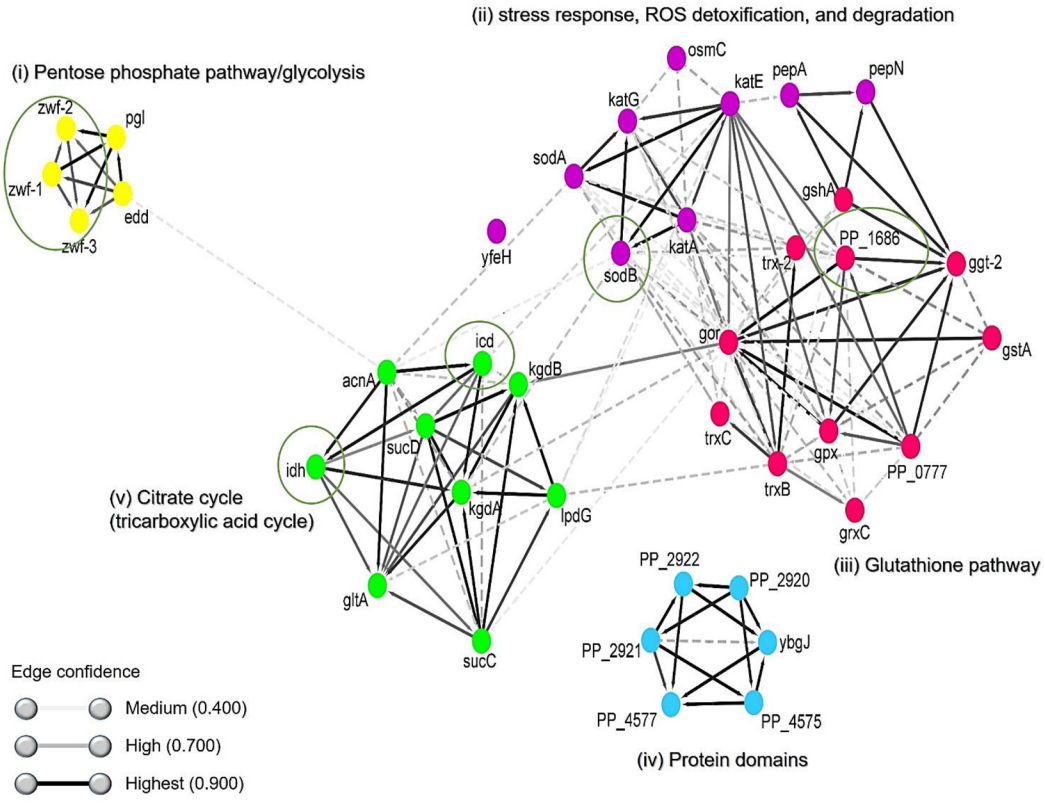

Figure 18. Co-expression analysis of DEGs for protein-protein interaction networks in *P. putida* which responded to the treatment of (*P. putida* + nZVI) and (*P. putida* + dissolved iron). Colors of the nodes represent a specific metabolic pathway or protein domain: (i) yellow nodes- Pentose phosphate pathway and glycolysis; (ii) purple nodes- stress response, detoxification, and reactive oxygen species degradation; (iii) pink nodes- glutathione pathway; (iv) blue nodes- a group of protein domains whose function is unrelated to any of the metabolic pathways in this network; (v) green nodes- citrate cycle (tricarboxylic acid cycle). The thickness of the edges/lines connecting nodes indicate the strength of the data support as shown in the legend above. The network has been expanded by an additional 10

proteins *via* the 'More' button in the STRING interface. Each node represents a protein produced by a single gene locus.

The oxidative branch converts glucose–6–phosphate into CO_2, NADPH, and ribulose 5–phosphate, whereas the non-oxidative branch maintains redox balance under stress conditions (Chavarría et al., 2013; Nikel et al., 2021). This effect was observed only in the cells exposed to dissolved iron, which can more easily enter cells than nZVI and could trigger endogenous stress in the cytoplasm (**Figure 17**) (Marsalek et al., 2012; Semerád et al., 2020; Ševců et al., 2011). It was demonstrated in the previous studies on *E. coli* and *P. putida* that the metabolic flux capacity via the *zwf* transcript in the PP pathway was increased upon the detection of H_2O_2 (Christodoulou et al., 2018; Nikel et al., 2021). It was further confirmed by the PPI analysis that *P. putida* activated gene sets that are crucial to increase energy drainage (ATP, NADPH, NADH, G6PDH), which can be coupled with the antioxidant system (i.e., glutathione). This phenomenon was more pronounced in the dissolved iron (ionic-specific) system than in the nZVI (particle-specific) system (**Figure 17**). Since saccharides processing is involved in the carbohydrate pathway to fuel glutathione metabolism, this will entail higher enzymatic activities to burn carbon to generate CO_2 and energy. This occurrence appeared similar in the dissolved iron system after 24 h of treatment, where the activation of all *atp* genes prevailed, indicating the higher demand for ATP and lower DO (**Figure 4B**) due to higher CO_2 production by cellular respiration.

4.4.7 Validation of transcriptomic data by qPCR

There was no significant difference in the expression of all analyzed ROS genes up to 3 h of exposure to either nZVI or dissolved iron (**Figure 19A**–**B**). However, the expression of certain ROS regulators was time- and treatment-dependent, such as the distinct upregulation of genes encoding SOD (*sodB*), redox sensing regulator (*oxyR*), and downregulation of a redox sensing regulator (*finR*) in dissolved iron exposure after 24 h. Comparing these qPCR gene expression data to the RNA-seq analysis performed, only the expression of the *sodB* gene was identified in both methods, whereas other genes were undetected in the RNA-seq reads. *P. putida* exposed to

dissolved iron (24 h) increased the expression of *sodB* by 1.69-fold, detected by qPCR (**Figure 19D**), and by 1.14- fold detected by RNA-seq (**Table 6**)

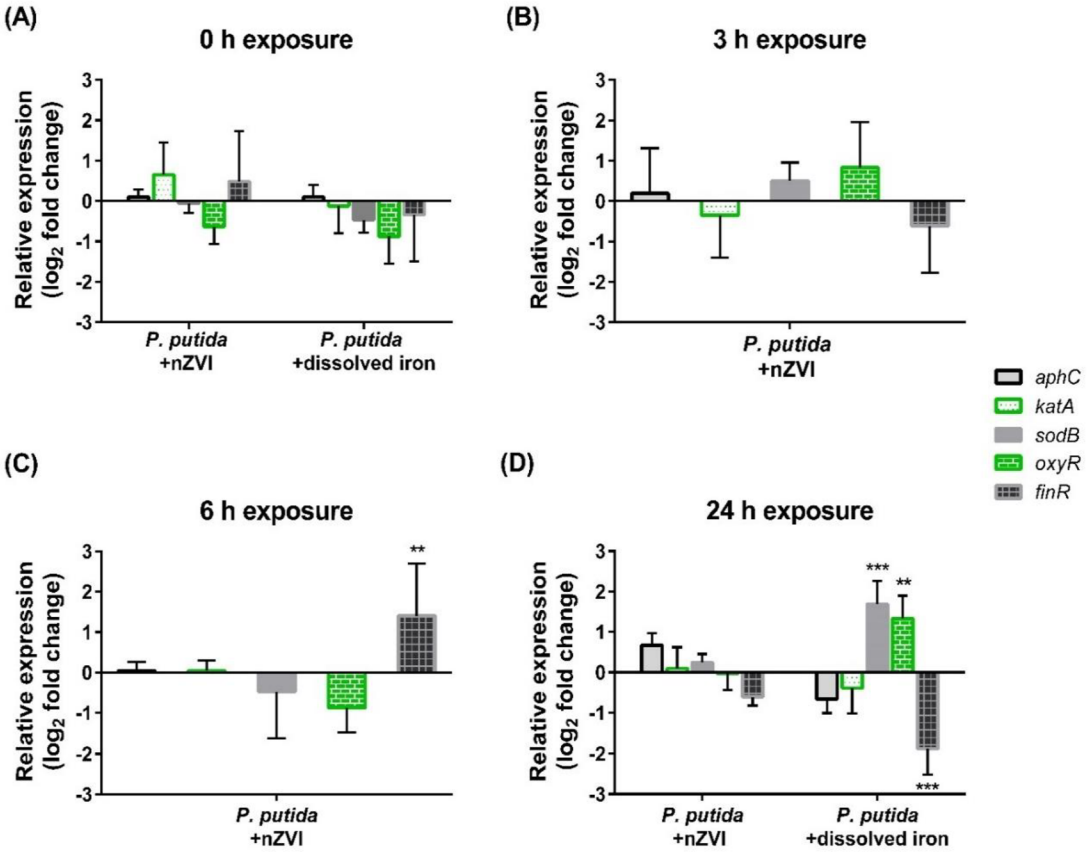

Figure 19. Relative gene expression analysis, validated by real-time PCR, on the ROS detoxifying regulators in *P. putida* exposed to nZVI and dissolved iron at 0, 3, 6, and 24 h. The internal control was *P. putida*, which set baseline zero at the *y* axis, and this was compared to *P. putida* exposed to nZVI or *P. putida* exposed to dissolved iron. Expression values are expressed in $\log_2$-fold change normalized with *gyrB* reference gene (mean ± SD; n = 3). Two-way ANOVA, Dunnett's test (0 and 24 h of exposure), and Sidak's multiple comparisons test (3 and 6 h of exposure) were used to calculate the statistical difference between treated (nZVI, dissolved iron) and untreated media with *P. putida* (*P < 0.05, **P < 0.01, ***P < 0.001).

In the present study, we set up a unique experimental system to explore the interplay between bacterial cells and nZVI or dissolved iron released directly from NPs. Although cell viability of *P. putida* was not affected by neither NPs nor dissolved iron, RNA sequencing data provided a detailed view of the stress response. Exposure

to dissolved iron (44.5 µg/L), but not to nZVI, led to an avalanche of gene expression for many metabolic activities and activation of signaling molecules involved in homeostasis of cytosolic stress level, such as energy metabolism, signal transduction, carbohydrate metabolism, and interfered with flagellar assembly proteins and two-component systems involved in external sensing. The aforementioned metabolic pathways have a direct impact on antioxidant pathways such as the glutathione-fueled energy rescue system for removing ROS. In line with these results, the *zwfA*, *icd*, *idh*, and PP5211 genes were enriched together with all *atp* genes for ATP production.

Overall, this study provides important insights into the multi-level regulations of *P. putida* when exposed to dissolved forms of iron released from nZVI. Cellular response was orchestrated within a sophisticated regulatory circuit based on the gene regulatory signaling and intercellular communication between external stimuli and cytosol. The response of these regulons represents an important tool for the future investigation of mechanistic details underlying oxidative stress in the context of ROS detoxification pathways.

II. *R. subcapitata*

In this study, the response of *R. subcapitata* to reactive nZVI and non-reactive nFe_3O_4 were compared and investigated, with respect to physico-chemical analysis, phytochrome content, cell morphology, and transcriptomics. The increased physical contact between NPs and algae (about 15% of the cells) caused changes in cell morphology and might later lead to cytosol leakage. RNA-seq was undertaken to explore the biological effects of nZVI and nFe_3O_4 on *R. subcapitata* at 1 h and 4 h, and the enriched metabolic pathways related to differentially expressed genes (DEGs) were identified.

4.5 Properties of nZVI and nFe_3O_4 in algal growth medium

This section describes the characterization of nZVI and nFe_3O_4 before exposure to *R. subcapitata* including SEM/EDS, DCS, and ICP-OES analysis. The exposure

medium used in this study was Sueoka's High Salt Medium (HSM). The summary of both iron NPs parameters in HSM is shown in **Table 7**.

Table 7. Summary of iron NPs physiochemical characteristics in HSM.

Nanoparticle	nFe_3O_4	nZVI
Product no./label	637106 *Sigma-Aldrich*	*NANOFER STAR*
Short description	- Non-reactive when dispersed in aqueous medium	- Reactive when dispersed in aqueous medium - nZVI stabilized with an oxidic layer
Form	Black nanopowder	Black nanopowder
Primary particle size (nm)	50–100 [a*]	59.8 ± 1.3 [a**] Oxide layer thickness: 4.3 ± 0.53
Size distribution in HSM (nm) [b]	765 ± 20	555 ± 19
Bulk density (kg/m^3) [a]	840	1120–1180
MW (g/mol) [a]	231.53	55.85
SSA (m^2/g) [a]	6–8	> 25
Metal purity (wt.%) [a]	97	Fe ≥ 65–80 Fe_3O_4 ≤ 35–20
Phase [a]	Fe_2O_4 Fe_3O_4	α–Fe: 74%, FeO: 8%, Fe_3O_4: 18%
Eh (mV) [c] in HSM	0.263 ± 0.001	0. 250 ± 0.001

[a] Reported by the manufacturers; [a*] Determined by Scanning electron microscopy (SEM),/ [a**] Determined by Transmission electron microscopy (TEM), [b] Measurement by DCS from immediate and up to 24 h after dispersion in HSM, [c] Measurement using SenTix® ORP-T 900 probe (WTW Inolab, Germany) immediately after spiking in HSM.

Both the iron NPs had the primary particle size below 100 nm as indicated in **Table 7**. When suspended in exposure medium, the hydrodynamic size distribution of nFe_3O_4 ranged around 765 (± 19.9) nm while nZVI was 555.3 (± 18.7) nm up to 24 h

(**Figure 20**), both iron NPs were relatively stable in the medium over 24 hours. Furthermore, nFe_3O_4 shows a bigger size distribution than nZVI, which might be due to hetero-aggregation with salts components on its surfaces (**Figure 20B**).

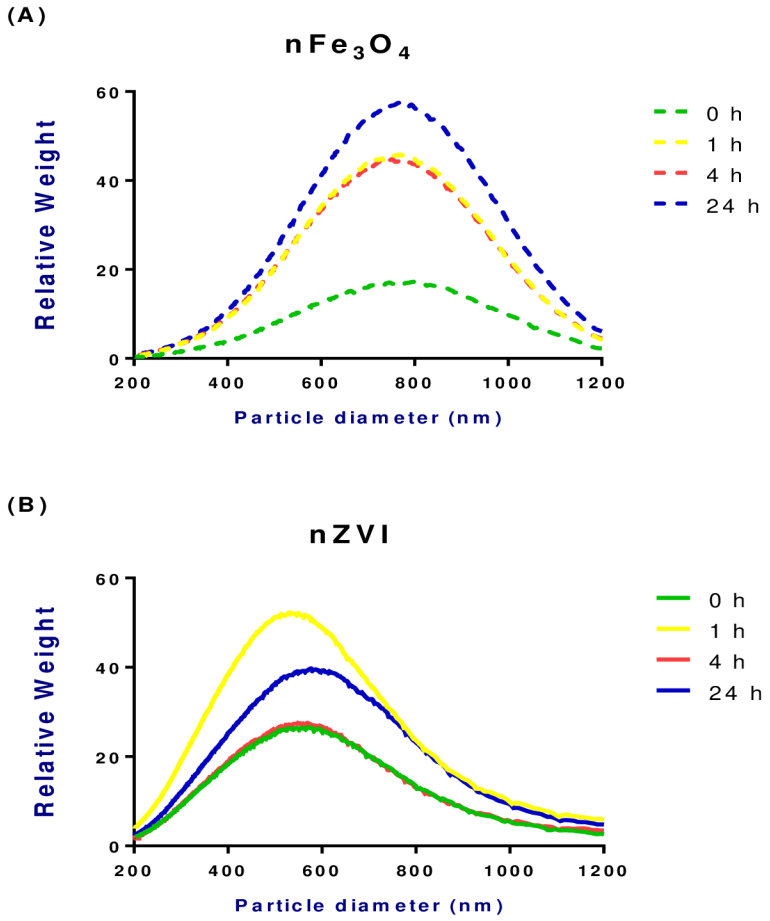

Figure 20. Hydrodynamic size distribution of 100 mg/L nFe_3O_4 and nZVI dispersed in HSM respectively up to 24 h. Values were presented in (nm) determined by differential centrifugal sedimentation (DCS). Analysis at 0 h indicated immediate exposure and instant sampling of the samples. HSM denotes Sueoka's High Salt Medium.

Furthermore, SEM and elemental mapping were performed using scanning electron microscopy and energy-dispersive X-ray spectroscopy (EDS). Surface morphology of pristine iron NPs are shown in (**Figure 21**) while SEM/EDS mapping of each iron NPs are shown in (**Figure 22** and **Figure 23**) respectively. Both the iron NPs were

aggregated into chain due to the magnetic interactions in between primary metal particles.

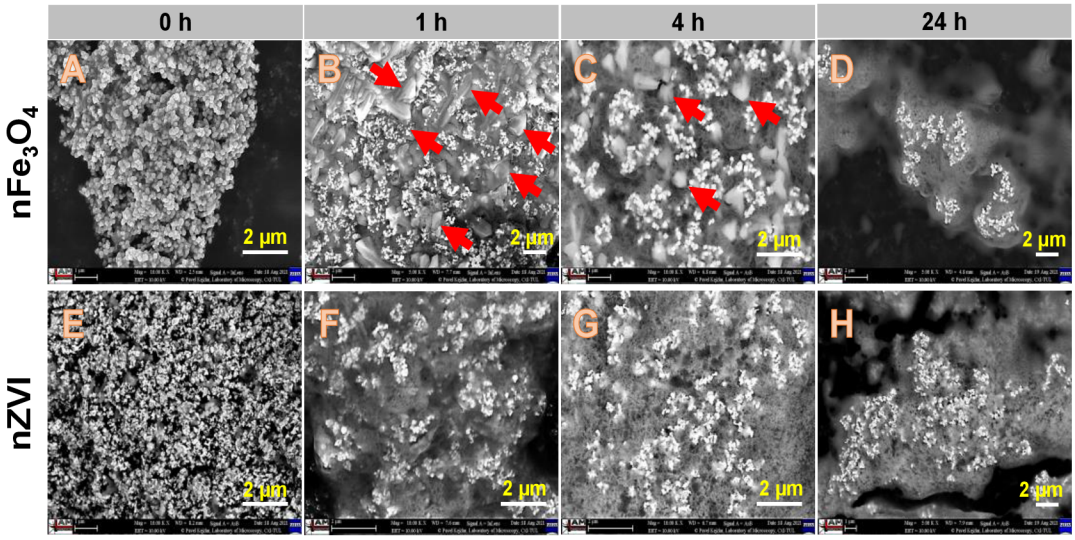

Figure 21. Scanning electron microscopy (SEM) images of pristine nFe_3O_4 and nZVI dispersed in HSM up to 24 h**.** Scale bar = as indicated in the pictures. The surface morphology of nFe_3O_4 and nZVI which determined by SEM after dispersion in exposure medium showed a rough spherical form and aggregated into chains, which could be attributed to the magnetic interaction between particles (Zhang and Manthiram, 1997).

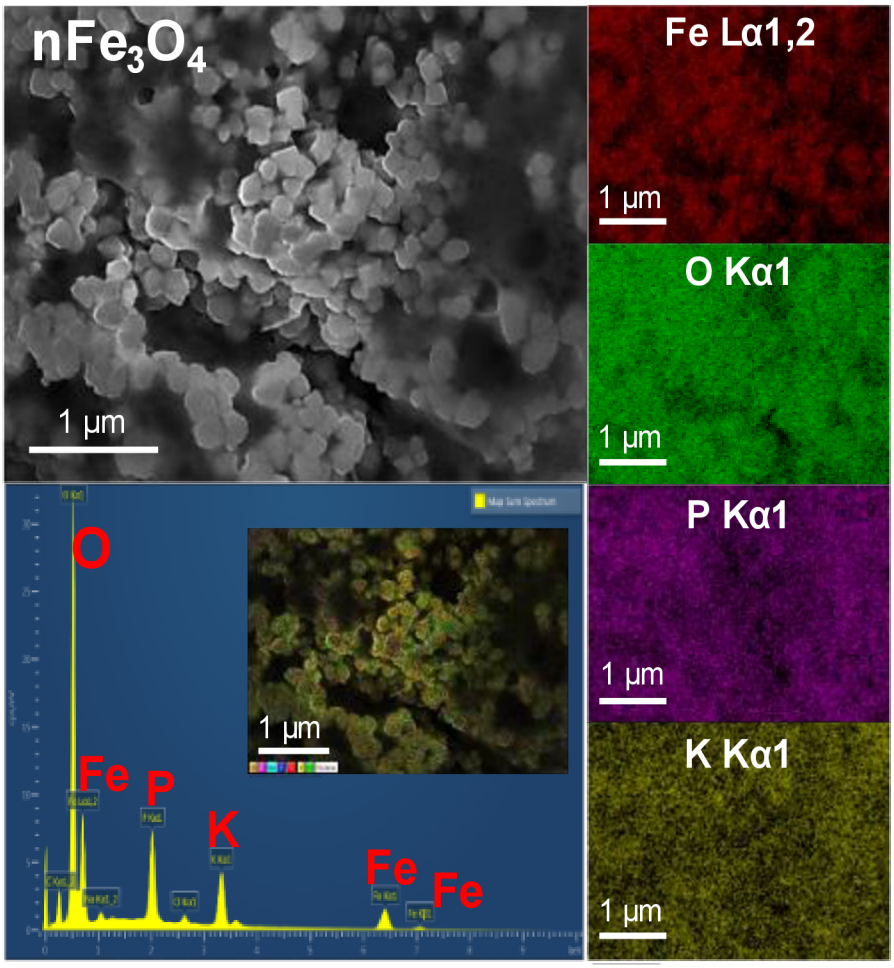

Figure 22. SEM image in selected location and corresponding EDS chemical hypermaps of pristine nFe_3O_4 dispersed in HSM at 0 h. SEM/EDX elemental overlay of iron and oxide (Fe and O) were from nFe_3O_4, phosphorus and potassium (P, K) were from HSM. The chemical mapping shows phosphorus (yellow color) was mostly absorbed to iron and oxide (cyan and green colors) on nFe_3O_4 surfaces. Scale bar = as indicated in the images.

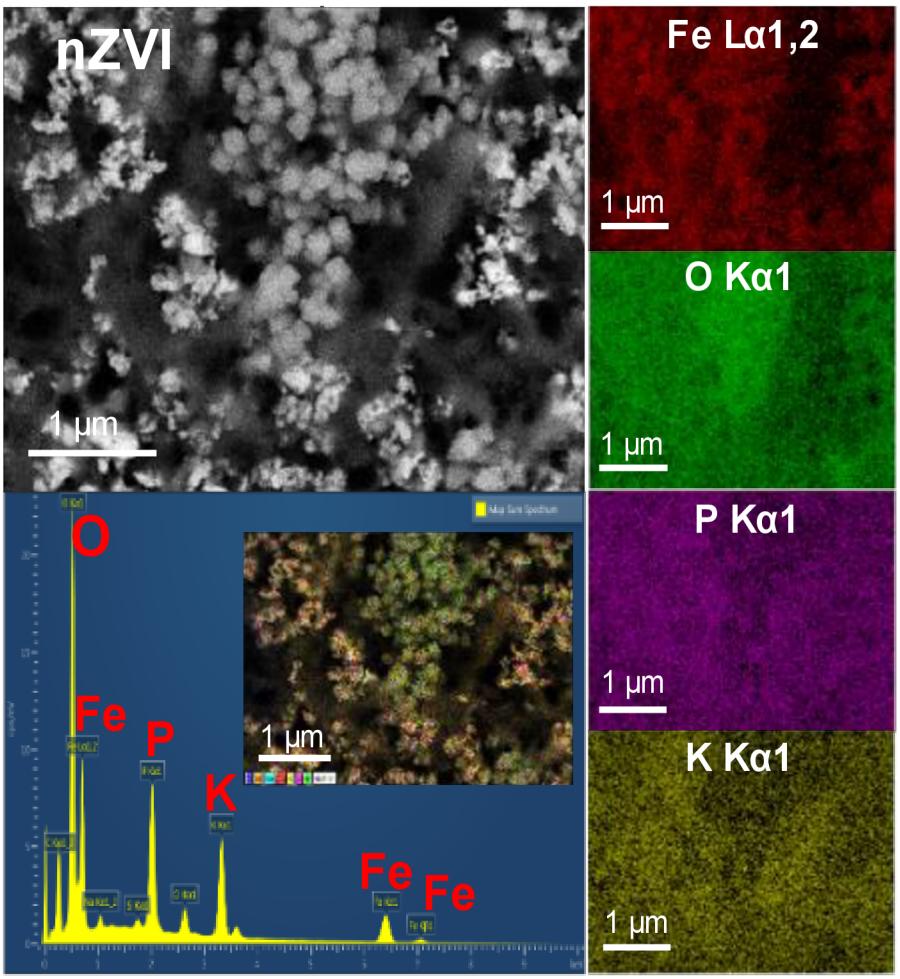

Figure 23. SEM image in selected location and corresponding EDS chemical hypermaps of pristine nZVI dispersed in HSM at 0 h. SEM/EDX elemental composition of iron and oxide (Fe and O) were from nZVI, phosphorus and potassium (P, K) were from HSM. The chemical mapping shows phosphorus (yellow color) were mostly absorbed to iron and oxide (red and green colors) on nZVI surfaces. Scale bar = as indicated in the images.

The release of dissolved iron from nFe_3O_4 and nZVI was compared after high-speed centrifugation method in section **3.2.7**. nFe_3O_4 showed a stable Fe^{2+}/Fe^{3+} concentrations approximately 1.39 mg/L throughout the dissociation in EM while the total iron released from nZVI continuously increased by 467% after 24 h, from initially 2.358 mg/L to 13.37 mg/L. The enhanced levels of Fe^{2+}/Fe^{3+} from nZVI suggesting that its higher likelihood to cause oxidative stress in cells due to the toxicity of Fe^{2+}. The concentration of total iron determined by ICP-OES is shown in **Figure 24**. The total iron from nFe_3O_4 released in HSM was consistent while the total iron from nZVI is showing an increasing trend up to 24 h.

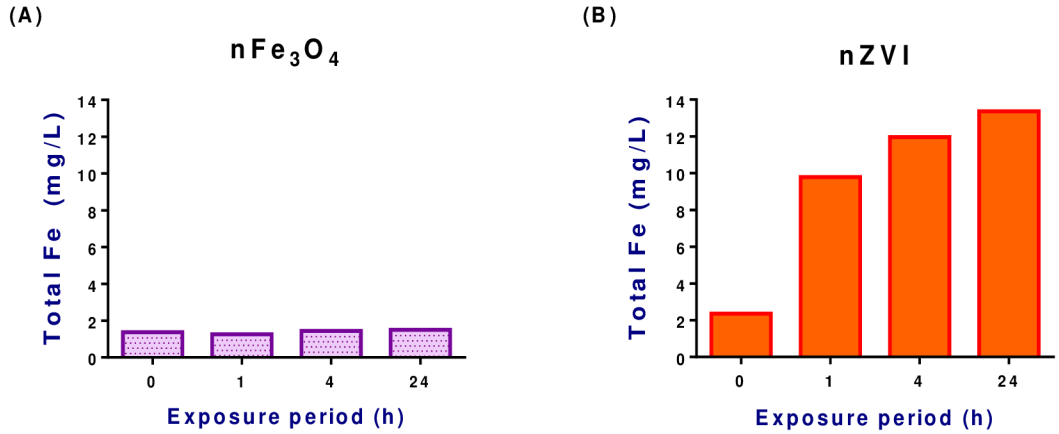

Figure 24. Total iron released in HSM from 100 mg/L of nFe_3O_4 and nZVI determined by ICP-OES. Note: analysis was performed in a condition without *R. subcapitata* and after separation of the particles of nZVI and nFe_3O_4 (two centrifugation cycles at 12,500 × *g* for 20 min).

4.6 Physicochemical parameters of nZVI and nFe_3O_4 during exposure

The physico-chemical parameters, phytochrome contents and chlorophyll fluorescence of *R. subcapitata* were evaluated over 120 hours. The overview of experimental design is depicted in **Figure 25A**. Samples with *R. subcapitata* generally had lower pH than samples without *R. subcapitata* (**Figure 25B**). Upon both nFe_3O_4 and nZVI exposure, the pH in the exposure medium was not affected by both iron NPs when comparing against control. However, the overall pH profile decreased towards the end of experiment to a pH 6.7. The initial DO and Eh before NPs addition averaged around 9.68 mg/L and 0.33 V respectively, while addition of nZVI into medium containing *R. subcapitata* resulted a sharp decrease in DO (8.1 mg/L: $P < 0.001$) and Eh (0.09 V; $P < 0.0001$) after 1 h, approximately 30% lower than control (**Figure 25B**). The decrease in DO prevailed first four hours, while Eh fluctuates from the addition of nZVI until 24 h and thereafter slowly recovering to the values similar as control condition. Previous work also showed a similar Eh recovery after 24-h exposure (Liu et al., 2017). In the previous studies by (Barnes et al., 2010; Nguyen et al., 2018) also showed an instant Eh reduction after the addition of nZVI; however, higher concentrations were applied. Furthermore, the samples containing *R. subcapitata* and nFe_3O_4 moderately lowered both DO and Eh within first four hours comparing to samples with *R. subcapitata* alone, while after 24 hours there was no significant difference in DO (**Figure 25B**). Eh values on the contrary were still significantly different to control up to 24 hours.

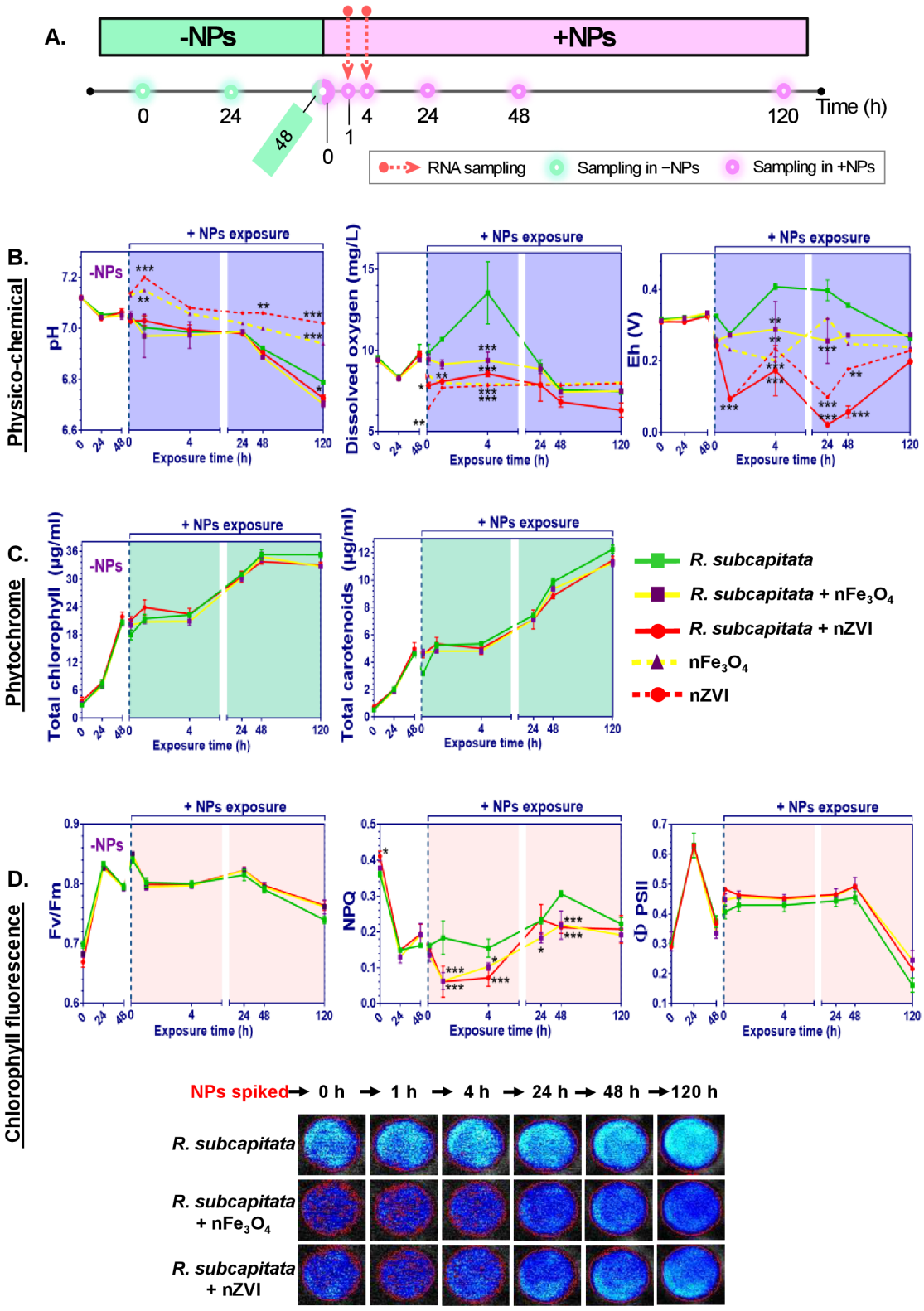

Figure 25. Experiment design and phenotypic responses of *R. subcapitata* treated with nZVI and nFe_3O_4 in Sueoka's high salt medium (HSM). (A) The sampling time points to elucidate the transcriptomics and phenotypic responses of *R. subcapitata* are depicted, the corresponding phenotypic data are shown in **Figure 20**–**Figure 29**. Samples for RNA extraction were taken after 1 and 4 h and the corresponding transcriptomic data are shown in **Figure 30**–**Figure 41**,

Table 9. (B) Physico-chemical analysis (pH, dissolved oxygen level, and Eh–pH); (C) Phytochrome content (total chlorophyll and carotenoid); (D) Chlorophyll fluorescence [maximum PSII yield (F_v/F_m), non-photochemical quenching (NPQ), effective PSII yield (Φ PSII)]; (mean ± SD; n = 3), and light intensity of chlorophyll fluorescence imaged under FluorCam FC 800-C Video Imager. Statistical analysis was computed from three independent biological replicates and triplicate technical readings by two-way ANOVA and Dunnett's test. *= level of significance changes were compared to untreated exposure medium containing only *R. subcapitata*, (*P < 0.05, **P < 0.001, ***P < 0.0001). Note: different scales of the *y*-axis. −NPs denotes before NPs exposure; +NPs denotes after NPs exposure.

The geochemical modeling showed the most probable elemental iron forms in the system under certain Eh–pH values (**Figure 26, Figure 27**). The evolution of different iron species was simulated during the experiment and predicted that insoluble iron species dominated in the system (**Figure 27**). In the presence of nZVI, the pH of the exposure medium ranged from 6.79 to 7.20, and the Eh values ranged from 0.022 to 0.250 V. The pH of the medium containing nFe_3O_4 ranged from 6.73 to 7.15, and the Eh values ranged from 0.201 to 0.320 V. According to Eh–pH diagram, nFe_3O_4 and nZVI tended to form the insoluble iron – goethite (**Figure 27**), this result is consistent with the findings of a previous study (Kumar et al., 2014; Liu et al., 2017).

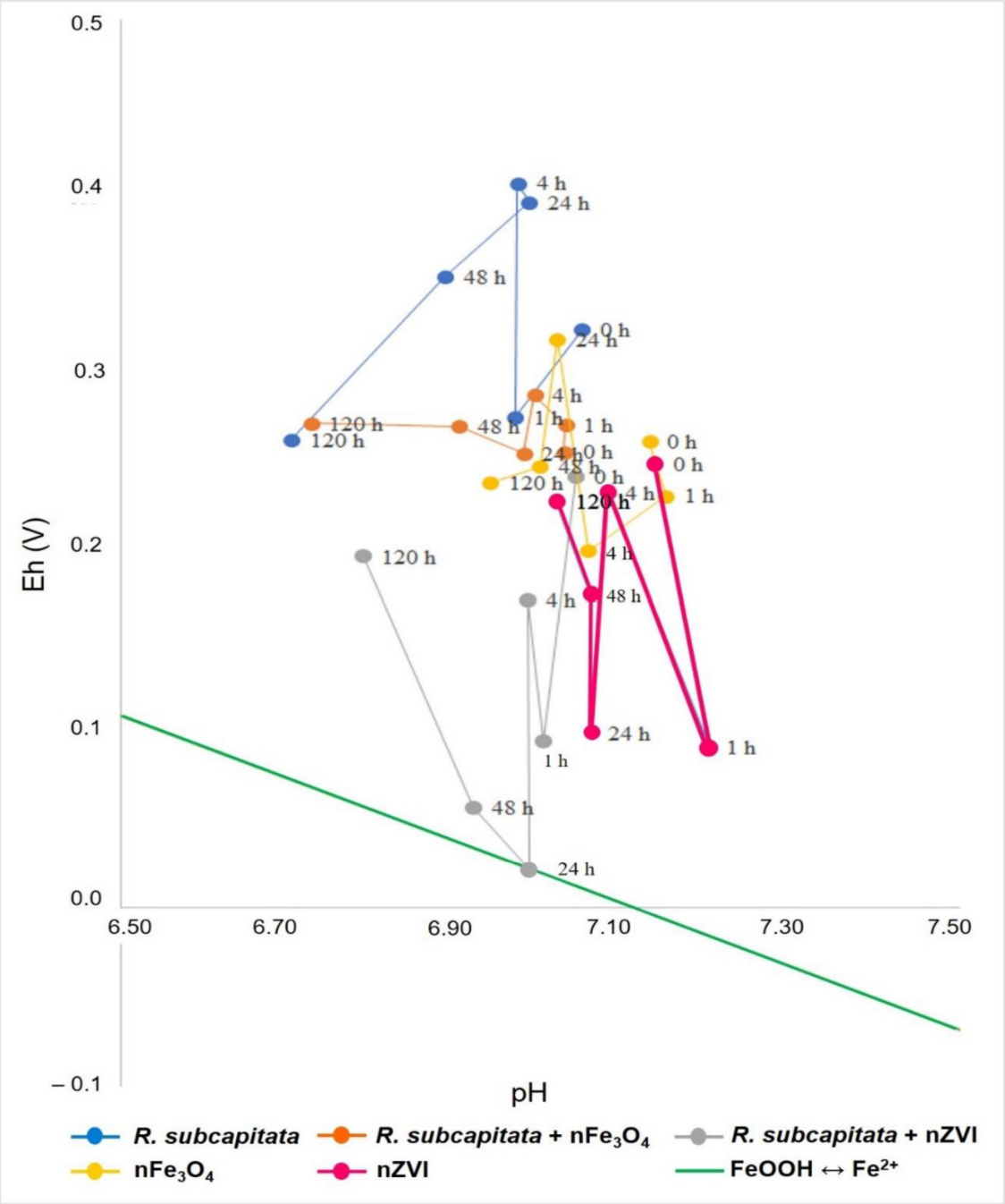

Figure 26. Overview of the Eh–pH values with all the treatments conditions plotted in the graph. Colors of the dots represent a different treatment condition. The green solid line defines the dependence of the equilibrium state in between the solid and liquid phases of goethite FeOOH crystallization and the logarithm of Fe^{2+} activity. The above concentrations correspond to the minimum solubility of chemical components with Fe. The *x* axis shows the pH values, the *y* axis as the redox potential (Eh) values presented in Volts. HSM denotes Sueoka's High Salt Medium used as exposure medium.

In all likelihood, these two iron NPs evolved quickly to goethite (**Figure 27**), with siderite evolved intermediately before goethite, shown as the equation below:

1. Fe^0 → siderite $FeCO_3$ → goethit FeOOH
2. Magnetite $Fe_3O_{4,(s)}$ → siderite $FeCO_3$ → goethite FeOOH

The state of siderite is often temporal and its shape was described as faceted-cylinder in (Joshi et al., 2018), and they were also identified in SEM images (**Figure 22**, **Figure 23**).

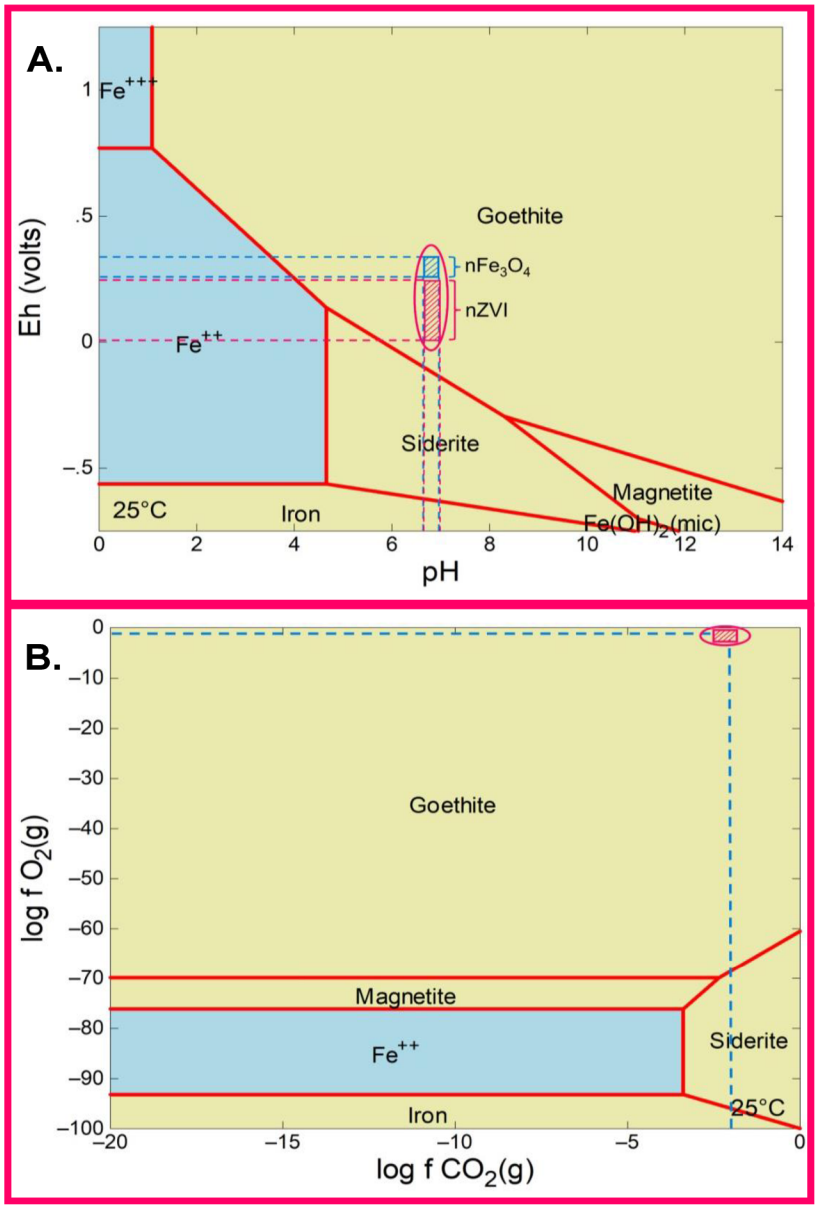

Figure 27. Geochemical modelling and stability of pristine 100 mg/L nFe_3O_4 and nZVI in the thermodynamic system Fe – CO_2(aq) – H_2O illustrating the predominance fields of Fe species and the stability fields of siderite, magnetite and goethite, (A) Eh – pH diagram: blue and red shaded regions indicate the Eh pH in the current study. (B) Stability and activity fields of $\log f_{CO_{2\,(g)}}$ – $\log f_{O_{2\,(g)}}$ indicating possible Fe phases in the thermodynamic systems of Fe –

CO_2(aq) – H_2O. Different color of the regions represents the solubility of its Fe components: brown color-solid; blue color-liquid, and gas phases; in its Fe– CO_2(aq) –H_2O thermodynamic system. The intersection of the lines (red circle) was intersected based on the calculated Eh–pH and geochemical modelling calculations of log $f(O_2)$, log f (CO_2), and log a Fe^{2+}. f_{CO_2} denotes carbon dioxide's fugacity; f_{O_2} denotes oxygen's fugacity

4.7 nZVI and nFe_3O_4 lowered NPQ

There were no significant changes in their phytochrome content (**Figure 25C**) and chlorophyll fluorescence, but the non-photochemical quenching (NPQ) decreased (**Figure 25D**), which implies high photosynthetic efficiency and low photoinhibition. NPQ is a photoinhibition process that occurs in the light-harvesting antennae photosystem II (PSII) and is activated when exposed to high light radiation, a photoprotective mechanism from photodamage to dissipate excess excitation energy into heat (Müller et al., 2001). Under high light condition, the light energy is absorbed in the light-harvesting antennae (Photosystem I or II), thereby ameliorates the light use efficiency, triggering many downstream photosynthetic mechanisms including more frequent electron transfer (high NADPH/$NADP^+$) and then increased ATP production. However, excessive accumulation of ATP/NADPH could eventually exceed the demands for the electron acceptor downstream at photosystem I (PSI) and plastoquinone pool (Allorent et al., 2013). In such event, NPQ could be induced to leverage the trade-off in between destruction and efficiency. Under darker environment containing nFe_3O_4 and nZVI, the NPQ was clearly lowered (about 55–62% reduction after 1 h comparing to time 0 and 30% lower than control) and the electron transfer of ATP/NADPH associated with carbohydrate metabolism also decreased (**Figure 25D, Figure 39**). NPs initially shadowed *R. subcapitata* and lowered several physiological endpoints, albeit *R. subcapitata* managed to recover from 4 h or 24 h onwards and regained slowly similar to control condition due to surplus of CO_2.

4.8 Physiological effect of nZVI and nFe_3O_4 on *R. subcapitata*

4.8.1 Short-term inhibition effect by nZVI and nFe_3O_4

In the control samples without NPs, *R. subcapitata* shows a typical regular sickle cell shape (**Figure 28A**–**Figure 28C**). After exposure to the NPs, there weren't any severe alteration of the cell shape (**Figure 28D**–**Figure 28I**). However, aggregated nanoparticles and their presence around the algal cells was observed.

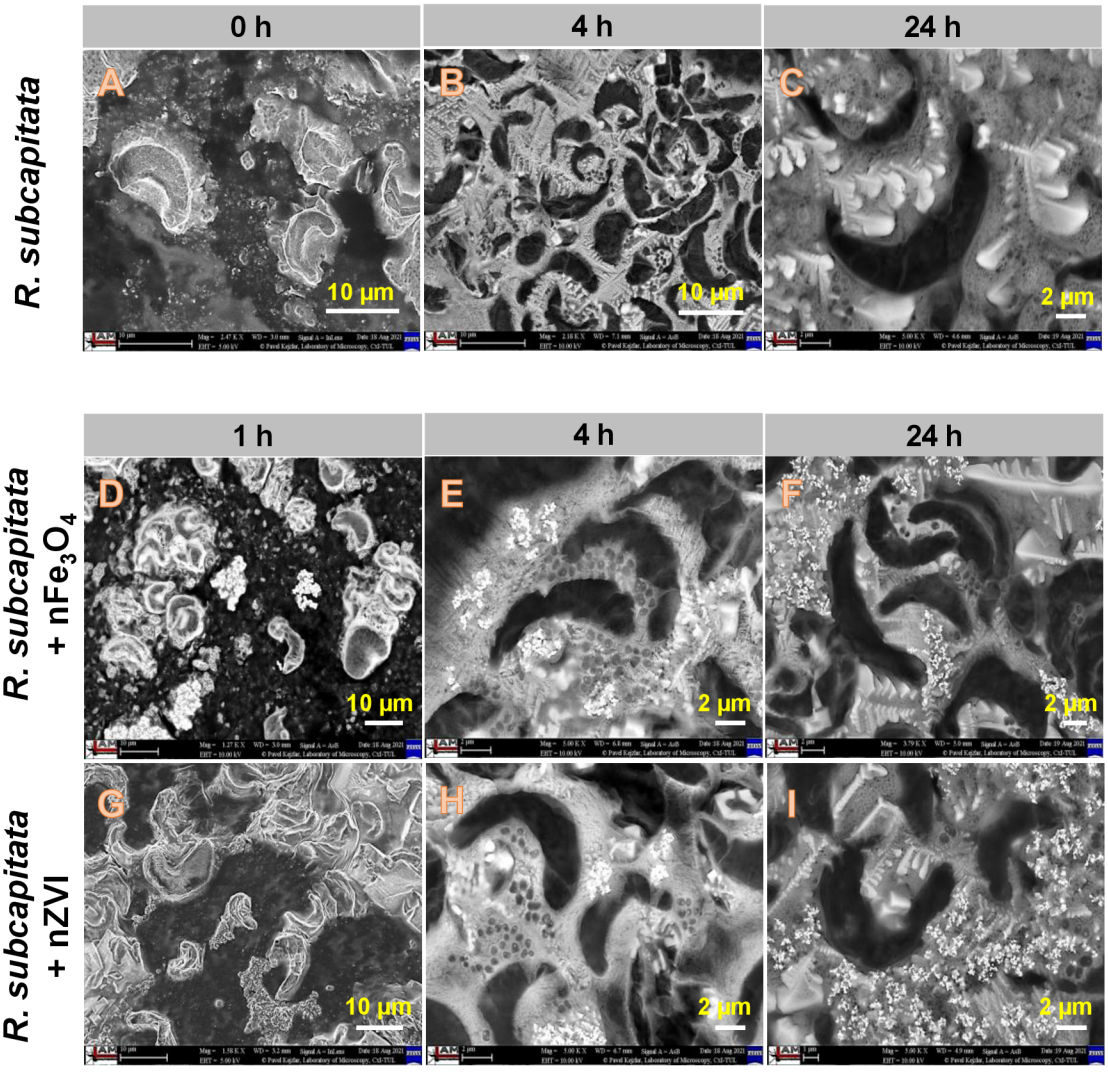

Figure 28. SEM images of *R. subcapitata* treated with nFe_3O_4 and nZVI up to 24 h in HSM. Negative control was HSM contains only *R. subcapitata* (A–C); *R. subcapitata* + nFe_3O_4 (D–F); *R. subcapitata* + nZVI (G–I). Scale bar = 2 or 10 µm.

Immediately after the NPs addition, both iron NPs weakened the autofluorescence of chlorophyll in algae as indicated by yellow arrows (**Figure 29A, B1, C1**) compared to the healthy algal cells (**Figure 29A, A1–A5**). This was further supported by the quantitative evaluation of algal autofluorescence, a slight reduction to 89.9% (nFe_3O_4) and 90.4% (nZVI) after 24 h was detected (**Figure 29B**). The chlorophyll autofluorescence was diminishing towards the end of the experiment, but this could be due to cell aging (**Figure 29A; 29B**). In addition to autofluorescence analysis, interaction between algal cells and NPs were evaluated by light microcopy. 90% of the cells in control had intact plasma membrane and cell wall during the whole experiment (**Figure 29C, 29E**). Contrary, the addition of nFe_3O_4 or nZVI immediately resulted in a NPs attachment on algal cell surface. This eventually led to complete cell deformation and lysis, or cell losing their chlorophyll pigments leaving empty cell/cell debris indicated by yellow arrows (**Figure 29C**). Both NPs could have inhibited the algal cells as observed by the reduction of cell viability number. Even such inhibition effect persisted until 24 h with highest proportion of dead cells recorded after 24 h, showing (24% and 28% reduction in viability in nFe_3O_4 and nZVI samples, respectively) (**Figure 29E**). Altogether, these cells impairment could be accompanied by the lower NPQ at 1 h, (30% lower than control) (**Figure 25D, Figure 29B, E**).

Another study showed lower growth inactivation or stimulation (< 10%) in *R. subcapitata* after treatment with nFe_3O_4 and nFe^0 (0 – 50 mg/L), however, lower concentration was applied (Llaneza et al., 2016). Furthermore, nZVI may have a stronger impact to reduce the algal activity than nFe_3O_4, which could be associated to its smaller size in our system (**Figure 20B**), but only at the beginning of the exposure up to 1 h (**Figure 29B**), showing a result which is consistent with previous comparison study when *E. coli* was exposed to nFe_3O_4 (9 mg/L) and nZVI (9 – 90mg/L) (Lee et al., 2008), or short-term inhibition in *P. putida* when exposed to nZVI (100 and 1000 mg/L) (Kotchaplai et al., 2017). nZVI was also shown to be more toxic than nFe_3O_4 when tested on the microalgae *Chlorella pyrenoidosa* or larvae of medaka fish *Oryzias latipes*, (Chen et al., 2012; Lei et al., 2016). Despite such inhibition effect, albeit *R. subcapitata* was able to recover thereafter, equivalent to values in control condition, suggesting the adaptability of algae in order to survive in an environment containing NPs or NPs may have oxidized over the time and became harmless to microorganisms (Auffan et al., 2008; Chen et al., 2012; Keller et al., 2012; Nguyen et al., 2018a). The overall end point for

autofluorescence counts showed 78.8% – 80.9% of photosynthetically active cells and viability counts ranged between 93.2% – 96.6% (4.25 – 5.31 × 10^7 cells/mL). Furthermore, nFe_3O_4 could have oxidized after 48 h, leaving a rusty color on algae surface (**Figure 29C, B5–B6); (Figure 29D**). However, study by (Diao and Yao, 2009) identified rusty iron oxides coated on the surface of microorganisms, by the aerobic exposure of nZVI (0.1 – 10 mg/L) after 5 min of reaction.

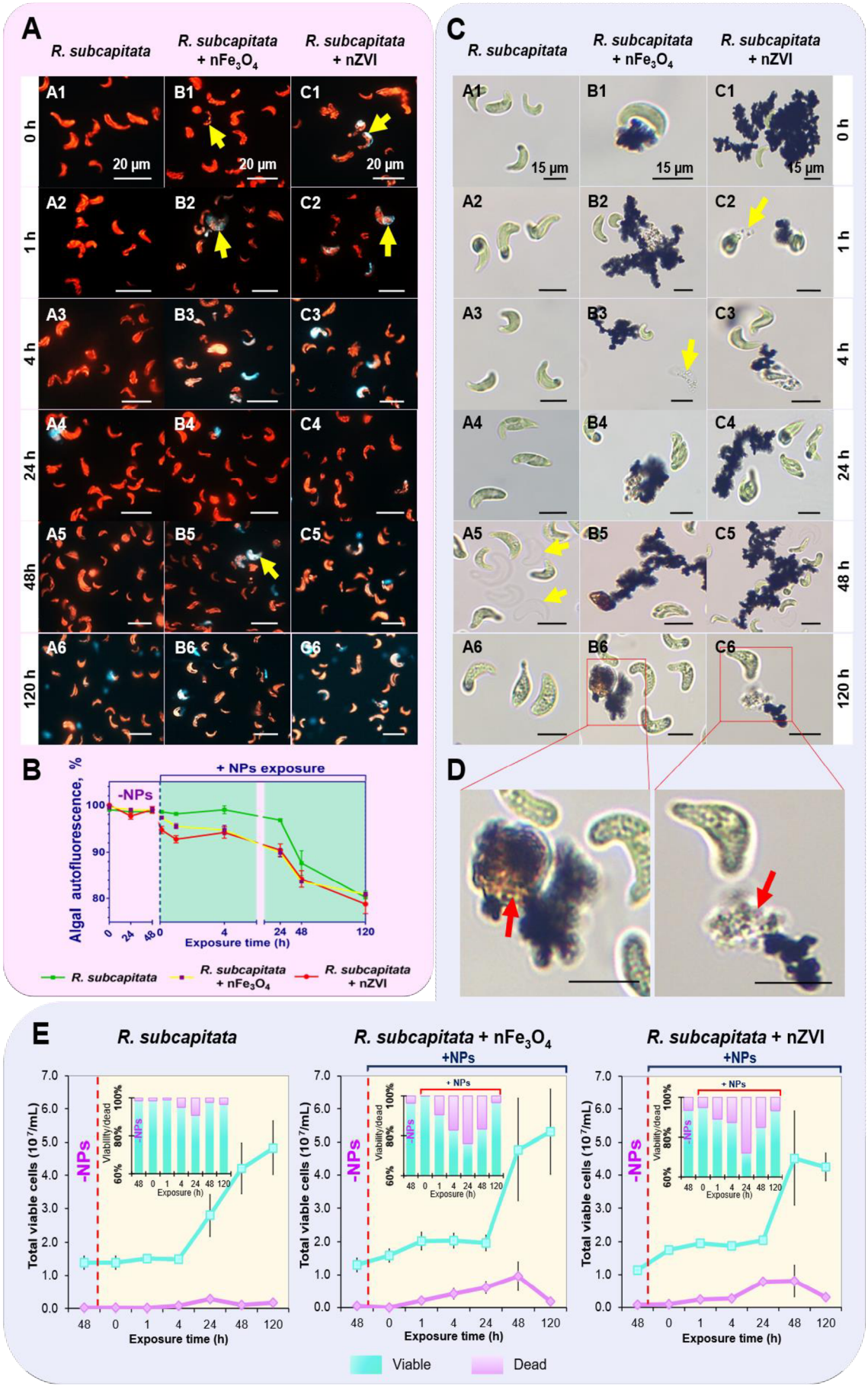
A
R. subcapitata
R. subcapitata + nFe3O4
R. subcapitata + nZVI
0 h
1 h
4 h
24 h
48h
120 h
20 μm
B
Algal autofluorescence, %
-NPs
+ NPs exposure
Exposure time (h)
R. subcapitata
R. subcapitata + nFe3O4
R. subcapitata + nZVI
C
15 μm
D
E
R. subcapitata
R. subcapitata + nFe3O4
R. subcapitata + nZVI
+NPs
-NPs
Total viable cells (10^7/mL)
Viability/dead
Exposure time (h)
Viable
Dead

Figure 29. Viability effect and morphological changes of *R. subcapitata* treated with nFe_3O_4 and nZVI exposed in HSM. (A) Cell autofluorescence and viability, healthy/live cell (red), damaged/dead cell (cyan). Scale bar = 20 µm (B) Total viable count of live cells. (C) Light microcopy images of algae indicate different cell stages and distribution. Scale bar = 15 µm. (D) Representative and enlarged image of algae at 120 h of cell indicate damaged cells and aggregation of NPs (red arrow). (E) Total viable and dead cells, determined by manual counting under light microscope, based on intact plasma membrane (live) and damaged plasma membrane (dead) cells. (B, E) Values were expressed in autofluorescence percentage, and number of cells, ($\times$ 10^7 cells/mL) respectively, (mean ± SD; n = 3). Yellow arrows indicate loss of autofluorescence intensity and chlorophyll content in algae cell. −NPs denotes before NPs exposure; +NPs denotes after NPs exposure.

Physiological analysis could serve as a baseline to indicate stress level of *R. subcapitata*, however, the lack of significant differences in some endpoints could limit its detailed investigation. Therefore, transcriptomic approach was set forth a paradigmatic mechanistic model to determine the effect of nFe_3O_4 and nZVI through evaluating the gene expression in *R. subcapitata*.

4.9 Transcriptomic response of *R. subcapitata* to nFe_3O_4 and nZVI

4.9.1 Selection of the best RNA extraction methods

The cell lysis efficiency by liquid nitrogen grinding, cell ribolization, and cell lyophilization was evaluated on *R. subcapitata* when in contact with 100 mg/L nFe_3O_4 or nZVI. Prior to that, the cells distribution were screened using a light microscope (**Figure 30**) by comparing the efficiencies of different cell lysis method used. The cells after the liquid nitrogen grinding looked very similar to those in control samples, where only a small number of cells were lysed (**Figure 30A, B**). A previous genome study of *R. subcapitata* (Suzuki et al., 2018) described successful isolation of RNA from a 100 mL culture using the same liquid nitrogen grinding method, however, it should be noted that the isolation of RNA from a 100 mL culture, by theory should yield higher RNA compared to our culture volume of 35 mL *R. subcapitata* belongs to the family *Selenastraceae*, is a robust microalga containing very rigid polysaccharide-based cell wall recalcitrance to breakage (Burczyk and Dworzanski, 1988; Suzuki et al., 2018). These polysaccharides, upon cell disruption, co-precipitates the RNA (Reis Falcão et al.,

2008) which then complicated the RNA extraction procedure and resulted low yield/quality of RNA. In our study, the RNA extraction protocol has been tailored to *R. subcapitata* using cell lysis procedure combining the overnight lyophilization of cells followed by ribolization of the cells resuspended in RNA lysis buffer resulted in the highest lysis efficiency (**Figure 30C**).

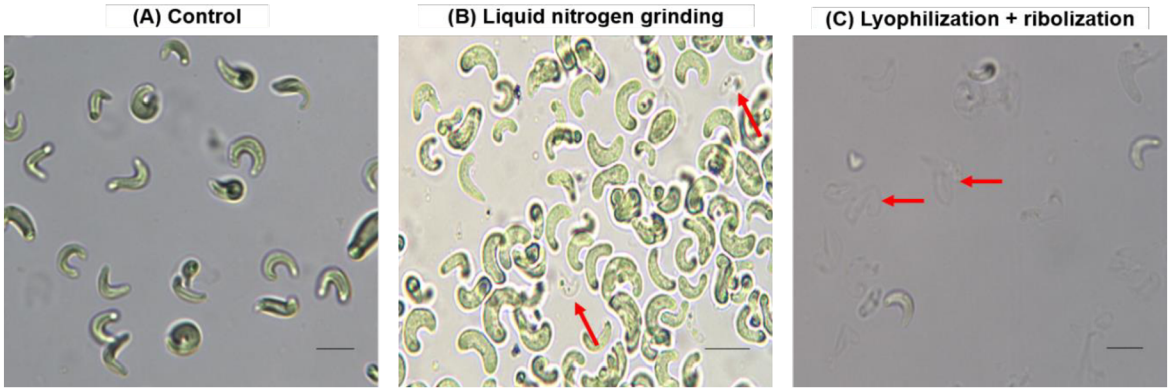

Figure 30. Light microscope images of *R. subcapitata* cell lysis before RNA extraction: (A) control cells before lysis, (B) cells after liquid nitrogen grinding, (C) overnight lyophilization of wet biomass prior to ribolyzation. Red arrows indicate the lysed empty cells. Scale bar = 15 µm.

The efficiency of different RNA extraction methods was then compared. Among the tested methods, phenol-chloroform extraction yielded the highest RIN working with the *R. subcapitata*-nanoparticles spiked samples and is shown in **Figure 31**. The representative electropherogram peaks of the experimental condition in respective to control, nFe_3O_4 and nZVI show the 18S and 28S peaks (**Figure 31B–D**).

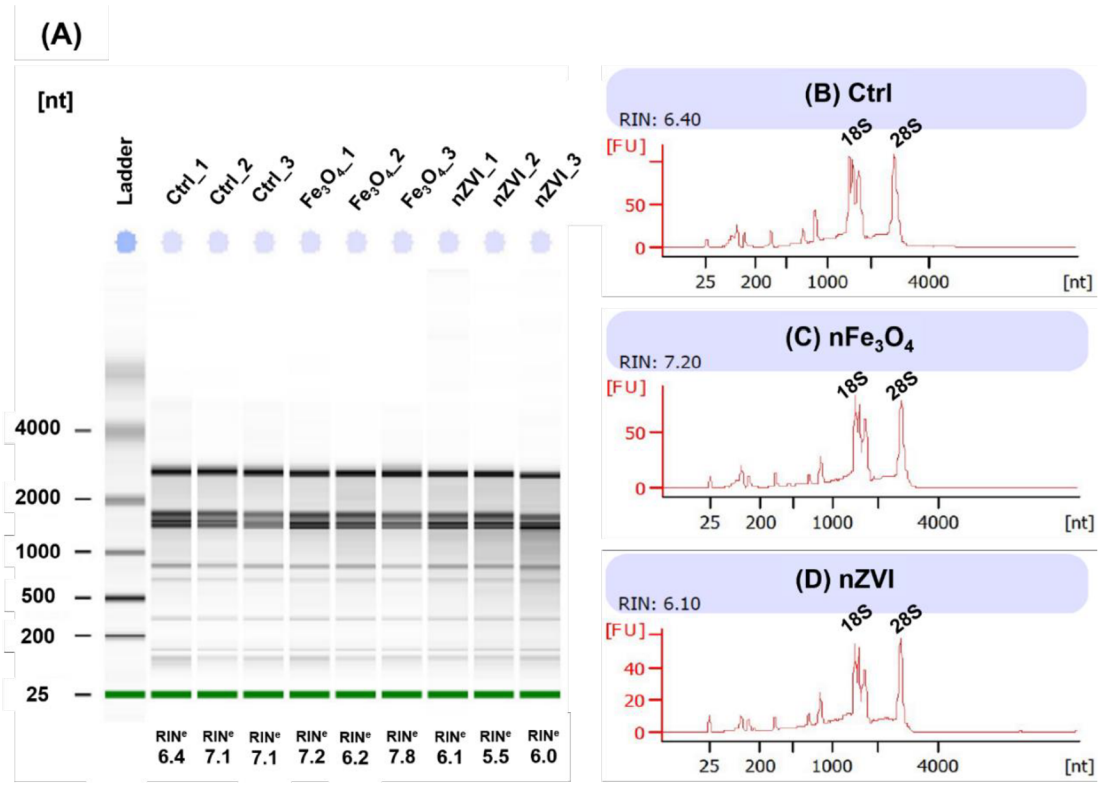

Figure 31. RNA integrity numbers of all isolated *R. subcapitata* samples compared on a bioanalyzer system (A), and electropherogram of rRNA peaks of untreated control (B), nFe3O4 (C), nZVI (D) using phenol-chloroform extraction method

Based on our data, extraction of the RNA from *P. putida*-nZVI samples was straightforward using the column-based extraction kit (Bioline ISOLATE II RNA Mini) while isolation of the RNA from freshwater microalgae *R. subcapitata* in nZVI or nFe_3O_4 spiked samples required an initial step including thorough cell lysis by combining overnight lyophilization of wet biomass, followed by ribolization of the dried biomass suspended in phenol and finally RNA isolation through phenol-based extraction. Presence of nZVI in the sample during cell lysis and RNA extraction did not considerably degraded the RNA isolated from *R. subcapitata*. In general, the column-based RNA extraction methods are recommended, except when isolation is compromised by polysaccharides or compounds which can bind to and/or co-precipitate with RNA. In such cases, phenol-based extraction methods may offer higher quality RNA obtained.

4.9.2 Assembly quality and completeness of *R. subcapitata* ATCC 22662 genome

The genome completeness of *R. subcapitata* was assessed and verified by BUSCO which detected 86.7% complete (C) and 6.4% fragmented (F) single copy genes in the assembly representing the good quality of the assembly (**Figure 32**) and the total number of RNA sequencing read count from each biological sample can be found in **Table 8**.

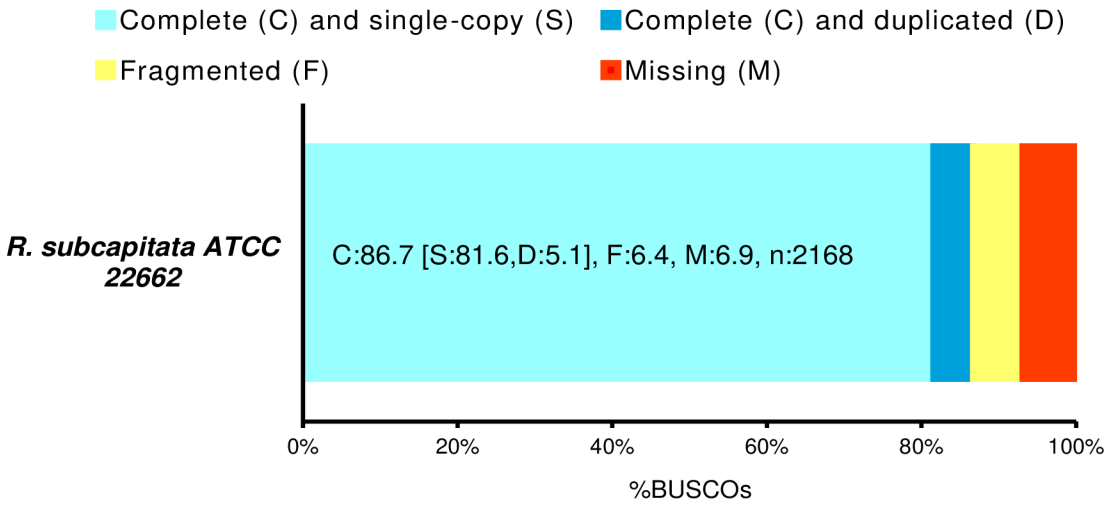

Figure 32. Assessment of *Raphidocelis subcapitata* ATCC 22662 genome assembly quality. BUSCO (Aves, n = 2168) genome completeness analysis of *R. subcapitata*.

Table 8. Total number of RNA sequencing reads obtained from respective samples

Sample, exposure period	Library	Biological Replicate	Total clean reads (million)	Total mapped reads (%)	Total mapped and properly paired (%)
R. subcapitata-nanoparticle free (1 h)	1h_control (1a)	1	4.42	88.99	79.16
	1h_control (1b)	1	4.31	89.25	79.60
	1h_control (1c)	1	4.46	89.40	80.18
	1h_control (1d)	1	4.36	89.30	79.68
	1h_control (2a)	2	4.02	94.66	89.34
	1h_control (2b)	2	3.93	94.77	89.35

	1h_control (2c)	2	4.08	94.88	89.81
	1h_control (2d)	2	3.98	94.75	89.27
	1h_control (3a)	3	4.08	93.60	87.90
	1h_control (3b)	3	3.97	93.71	87.96
	1h_control (3c)	3	4.12	93.83	88.44
	1h_control (3d)	3	4.01	93.67	87.86
R. subcapitata exposed to 100 mg/L nFe_3O_4 (1 h)	1h_nFe_3O_4 (1a)	1	4.23	92.73	86.32
	1h_nFe_3O_4 (1b)	1	4.13	92.88	86.44
	1h_nFe_3O_4 (1c)	1	4.28	93.03	86.98
	1h_nFe_3O_4 (1d)	1	4.17	92.88	86.37
	1h_nFe_3O_4 (2a)	2	3.58	94.49	89.27
	1h_nFe_3O_4 (2b)	2	3.49	94.64	89.42
	1h_nFe_3O_4 (2c)	2	3.62	94.74	89.82
	1h_nFe_3O_4 (2d)	2	3.52	94.58	89.26
	1h_nFe_3O_4 (3a)	3	4.92	94.23	88.69
	1h_nFe_3O_4 (3b)	3	4.79	94.37	88.79
	1h_nFe_3O_4 (3c)	3	4.97	94.44	89.18
	1h_nFe_3O_4 (3d)	3	4.84	94.32	88.65
R. subcapitata exposed to 100 mg/L nZVI (1 h)	1h_nZVI (1a)	1	3.35	93.79	88.36
	1h_nZVI (1b)	1	3.28	93.90	88.43
	1h_nZVI (1c)	1	3.41	94.02	88.89
	1h_nZVI (1d)	1	3.32	93.86	88.31
	1h_nZVI (2a)	2	4.26	92.94	86.11
	1h_nZVI (2b)	2	4.16	93.10	86.26
	1h_nZVI (2c)	2	4.31	93.23	86.78
	1h_nZVI (2d)	2	4.21	93.12	86.22
	1h_nZVI (3a)	3	3.90	94.49	89.82
	1h_nZVI (3b)	3	3.80	94.62	89.91
	1h_nZVI (3c)	3	3.91	94.71	90.28
	1h_nZVI (3d)	3	3.81	94.57	89.77
R. subcapitata-nanoparticle free (4 h)	4h_control (1a)	1	4.70	94.84	90.46
	4h_control (1b)	1	4.58	94.88	90.39
	4h_control (1c)	1	4.74	94.98	90.82
	4h_control (1d)	1	4.60	94.82	90.24

	4h_control (2a)	2	3.72	93.40	87.36
	4h_control (2b)	2	3.64	93.53	87.50
	4h_control (2c)	2	3.75	93.66	87.98
	4h_control (2d)	2	3.66	93.51	87.41
	4h_control (3a)	3	4.86	94.30	89.36
	4h_control (3b)	3	4.73	94.40	89.36
	4h_control (3c)	3	4.89	94.49	89.81
	4h_control (3d)	3	4.77	94.34	89.22
R. subcapitata exposed to 100 mg/L nFe_3O_4 (4 h)	4h_nFe_3O_4 (1a)	1	5.58	94.03	88.97
	4h_nFe_3O_4 (1b)	1	5.45	94.12	88.94
	4h_nFe_3O_4 (1c)	1	5.64	94.23	89.41
	4h_nFe_3O_4 (1d)	1	5.49	94.07	88.79
	4h_nFe_3O_4 (2a)	2	3.92	95.16	90.67
	4h_nFe_3O_4 (2b)	2	3.83	95.22	90.67
	4h_nFe_3O_4 (2c)	2	3.95	95.31	91.02
	4h_nFe_3O_4 (2d)	2	3.86	95.15	90.50
	4h_nFe_3O_4 (3a)	3	4.62	93.07	86.76
	4h_nFe_3O_4 (3b)	3	4.52	93.18	86.85
	4h_nFe_3O_4 (3c)	3	4.68	93.31	87.34
	4h_nFe_3O_4 (3d)	3	4.57	93.16	86.77
R. subcapitata exposed to 100 mg/L nZVI (4 h)	4h_nZVI (1a)	1	5.28	94.36	88.55
	4h_nZVI (1b)	1	5.15	94.48	88.65
	4h_nZVI (1c)	1	5.32	94.60	89.09
	4h_nZVI (1d)	1	5.19	94.46	88.54
	4h_nZVI (2a)	2	3.66	94.70	89.88
	4h_nZVI (2b)	2	3.56	94.82	89.97
	4h_nZVI (2c)	2	3.69	94.89	90.30
	4h_nZVI (2d)	2	3.58	94.77	89.84
	4h_nZVI (3a)	3	4.86	94.23	89.28
	4h_nZVI (3b)	3	4.75	94.29	89.29
	4h_nZVI (3c)	3	4.91	94.42	89.72
	4h_nZVI (3d)	3	4.80	94.27	89.19

4.9.3 nZVI triggered more pronounced transcriptomic response than nFe_3O_4

The total raw reads of each sample are depicted in **Figure 33A**. The range of CPM values covered more than five orders of magnitude and the transcript abundances for all samples were quite similar (**Figure 33B**).

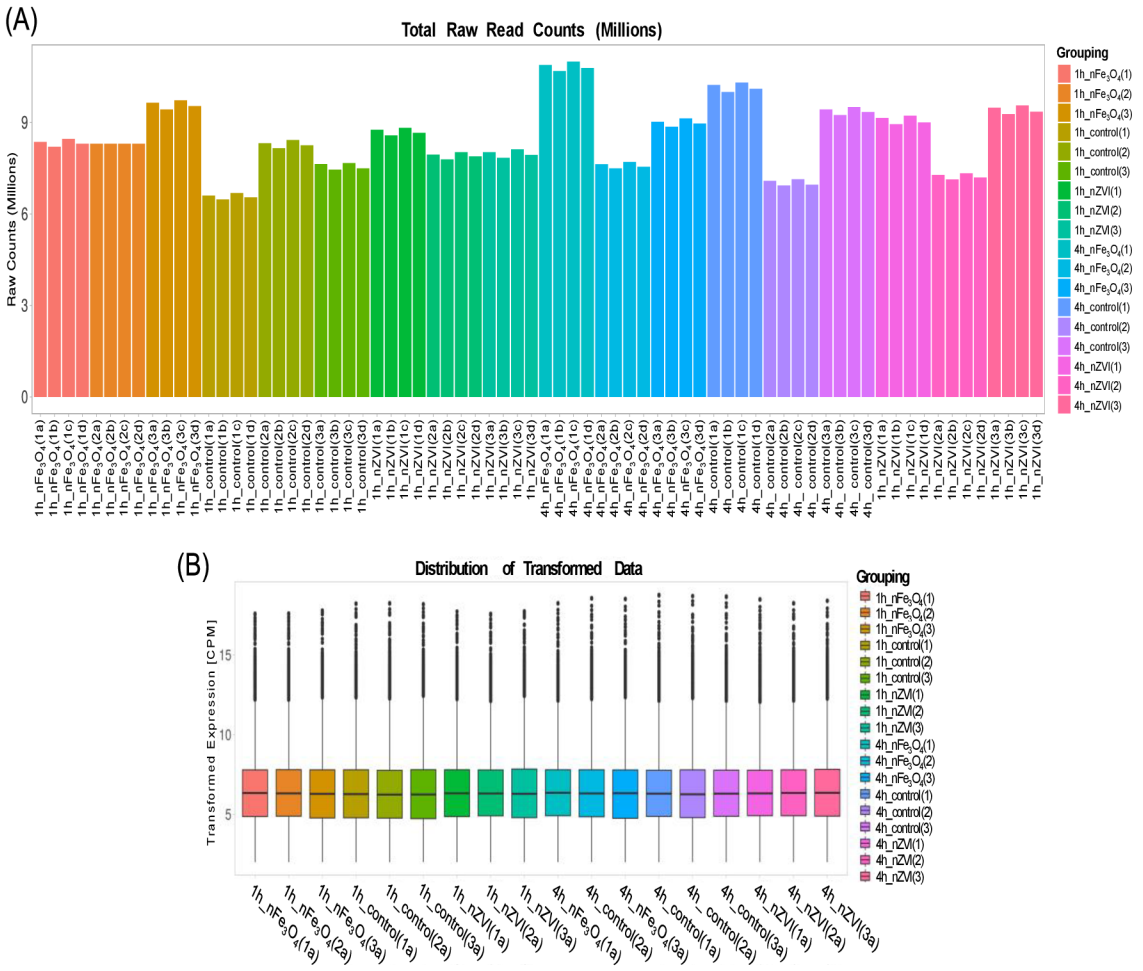

Figure 33. The transcript abundance in *Raphidocelis subcapitata* ATCC 22662 after the exposure of nFe_3O_4 and nZVI. (A) Total raw read counts (millions) from all samples. (B) Transcript abundances from all time points expressed in CPM values. The black horizontal line in the box-whisker plot represents median value, the black horizontal line separating the upper and lower box represent the interval between first and third quartiles, the two whiskers indicate 1.5× interquartile range respectively and the black dots are the outliers. NOTE: Idep makes a filtering before it starts further calculations, that represents the converted count data. CPM (Counts Per Million) are obtained by dividing counts by the library count sum and multiplying and the results by a million. Control = *R. subcapitata* without NPs exposure.

When the cells were exposed to nFe_3O_4 or nZVI, the expression profiling of *R. subcapitata* was analyzed at 1 h and 4 h (**Figure 34**–**Figure 36**). A functional enrichment analysis of the top 50 most highly expressed genes in total is shown in **Figure 34A**. Differentially expressed genes (DEGs) grouping in genetic information processing (27% genes), transmembrane signaling transport (23% genes) and carbohydrate-energy conversion associated metabolism (both sum up as 22% genes) were topped as the highest proportion in the top 50 DEGs. In addition to the most highly expressed genes in total, the DEGs between the exposure conditions and different time points were also analyzed (**Figure 34B, Figure 34C**). Due to similar transcript abundances across samples (**Figure 33B**), the pairwise comparisons were applied, whereby gene expression levels were compared between conditions. A higher number of DEGs were identified between the three exposure conditions at the earlier time point of 1 h (sharing 2,087 mutual genes). The transcriptomic response changed and declined at the later time point of 4 h (sharing 477 mutual genes), and approximately 12.5 – 65.5% DEGs reduction in all the exposure conditions was detected. Furthermore, *R. subcapitata* exposed to nZVI caused an upward trajectory of 7,380 DEGs (nZVI versus control), a distinctively more pronounced expression profile compared to when *R. subcapitata* was exposed to nFe_3O_4 affecting 4,601 DEGs (nFe_3O_4 versus control) within 1 h (**Figure 34B**). Principal component analysis (PCA) of the RNA-seq data confirmed the gene expression consistency among biological replicates and its clear dissimilarities in between treatment profiles and exposure hours (**Figure 34D**). nZVI exposure exhibited a furthest relative distance from the control and nFe_3O_4 exposure, revealing nZVI exposure triggered a distinctly different transcriptomic profile in *R. subcapitata*. Additionally, an overview of gene expression data is shown in (**Figure 35**, **Figure 36**), where large number of genes were found down-regulated in carbohydrate, energy metabolisms, while up-regulated in porphyrin metabolism. To unravel the chain of molecular details triggered in *R. subcapitata* following both the NPs exposure, their regulatory pathways is discussed in next section.

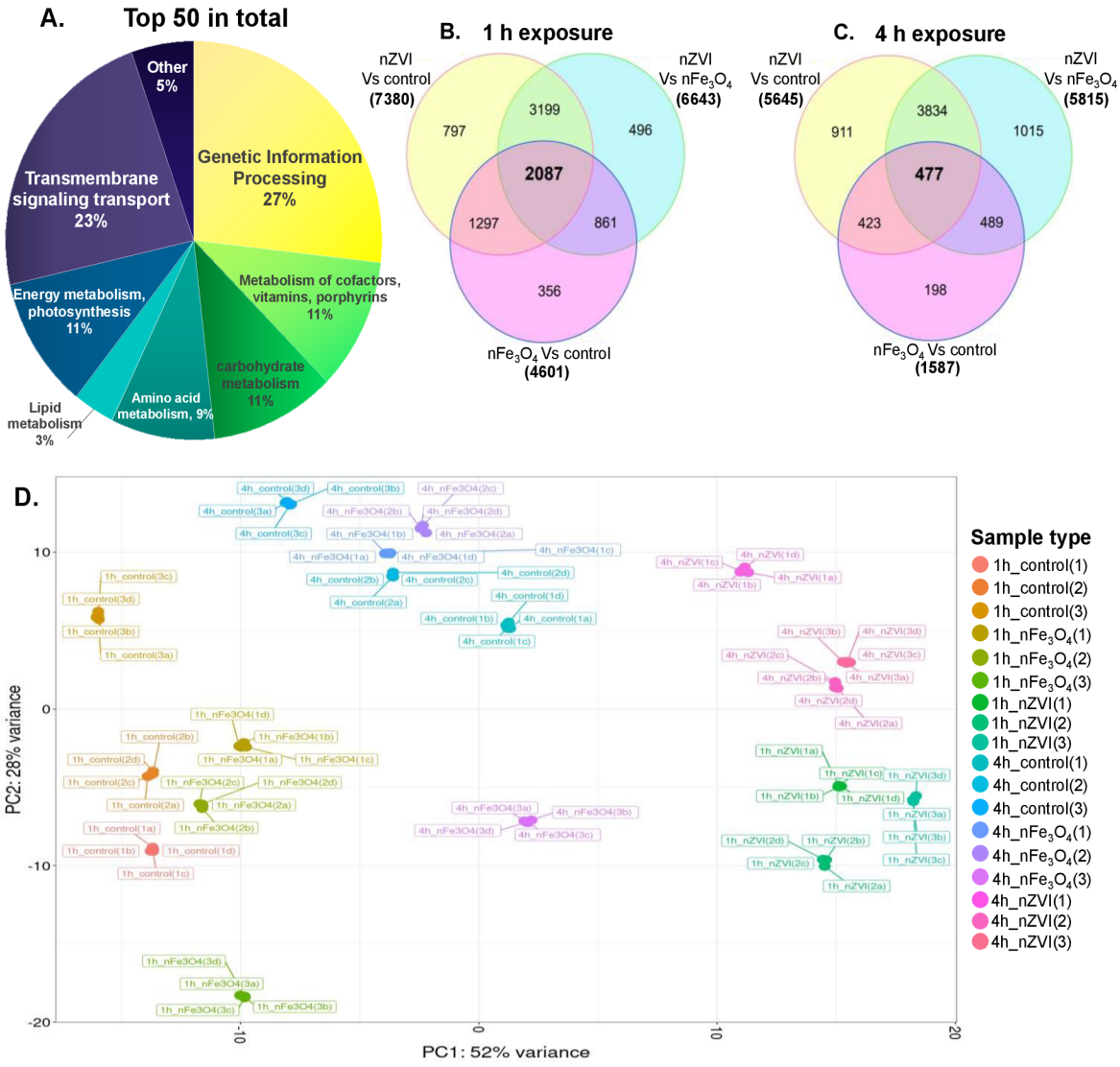

Figure 34. Gene expression profiling of *R. subcapitata* after the exposure of nFe_3O_4 and nZVI. (A) Metabolic pathways of top 50 mostly expressed genes. (B, C) Comparison of DEGs between exposure treatments and exposure time. Pairwise comparison was applied comparing the gene expression between conditions. Values within the intersecting sets represent genes that were more expressed when compared to the other conditions. (D) Principal component analysis of the RNA-seq data. The percentage in the axes represent the fraction of variance. The first principal component (PC1) is shown on the *x* axis, whereas the second principal component (PC2) is shown on the *y* axis. Treatment types and exposure hours are represented by different colors. Control = *R. subcapitata* without nanoparticle exposure.

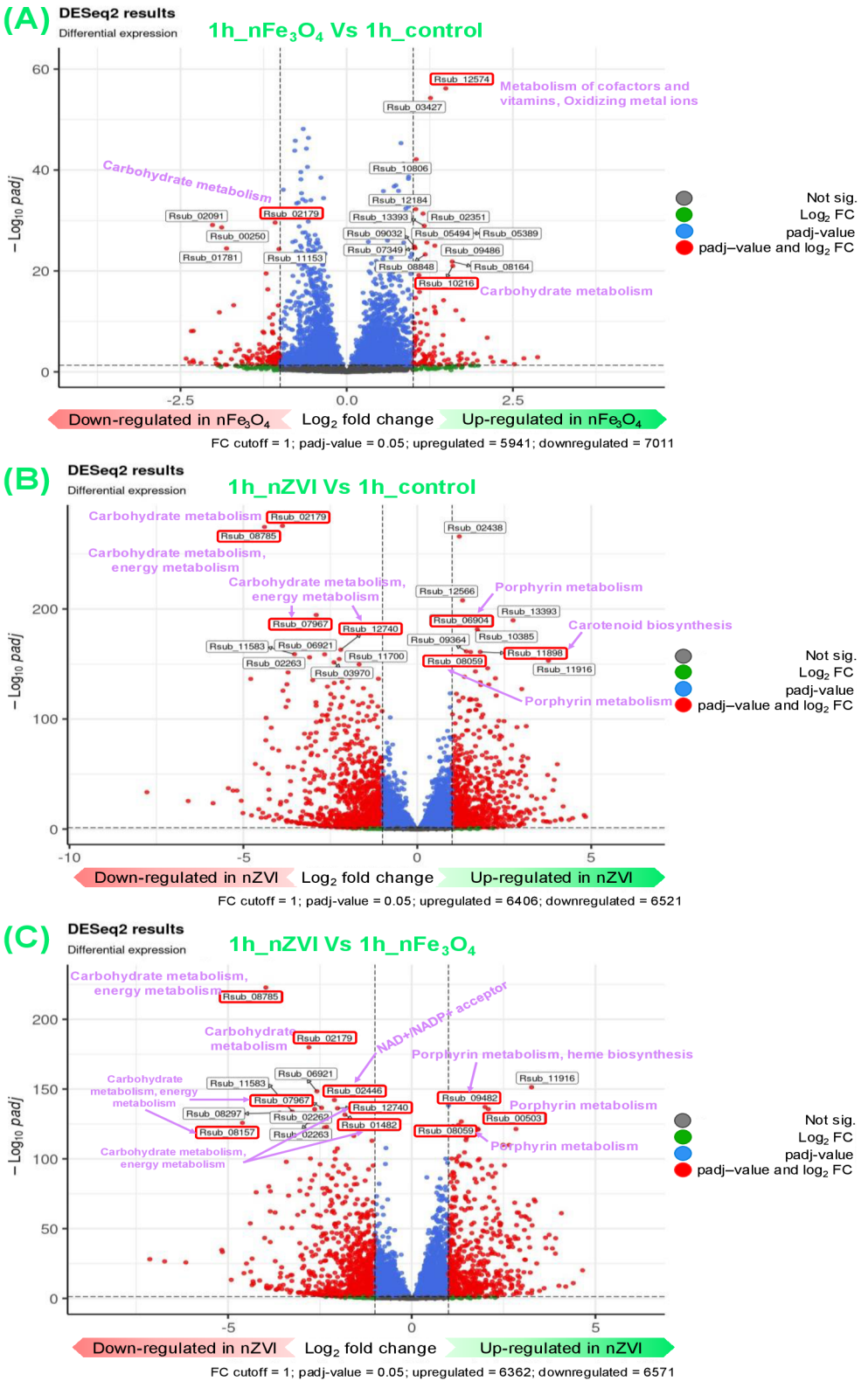

Figure 35. Volcano plots of all the expressed genes in three treatment groups after 1 h exposure. (A) nFe_3O_4 vs control (B) nZVI vs control (C) nZVI vs nFe_3O_4. *X*-axis represents the log_2(FC) for the two compared conditions, whereas – log_{10}(padj) from the gene expression analysis is shown on the *y*-axis. Red dots (Up and down-regulated) correspond to genes with significant

differences in their expression, while blue and grey dots correspond to genes with no significant differences, as indicated in the legend for each plot.

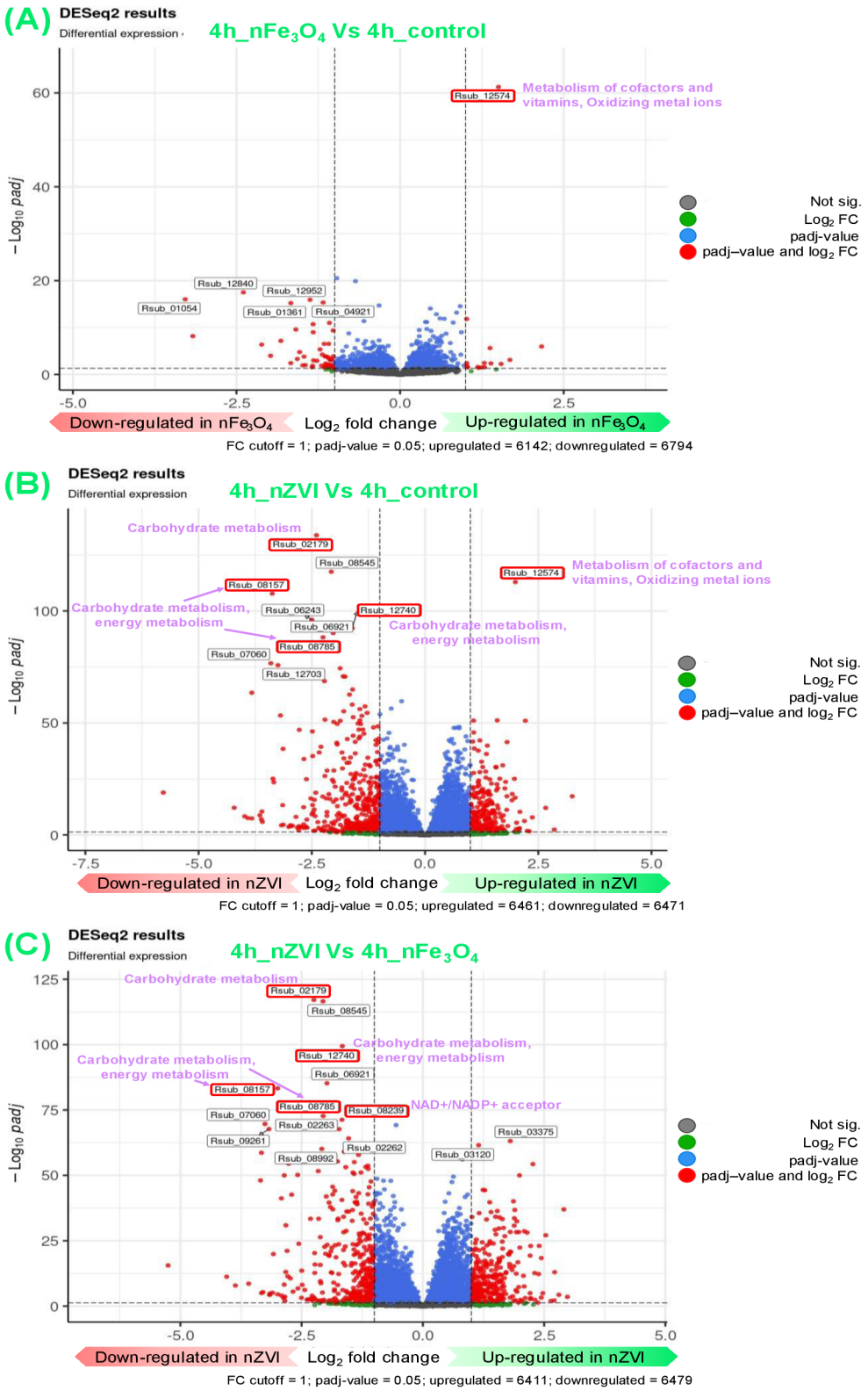

Figure 36. Volcano plots of all the expressed genes in three treatment groups after 4 h exposure. (A) nFe_3O_4 vs control (B) nZVI vs control (C) nZVI vs nFe_3O_4. *X*-axis represents the log_2(FC)

for the two compared conditions, whereas – log_{10}(padj) from the gene expression analysis is shown on the *y*-axis. Red dots (Up and down-regulated) correspond to genes with significant differences in their expression, while blue and grey dots correspond to genes with no significant differences, as indicated in the legend for each plot.

4.9.4 Overview of transcriptomic changes and pathway enrichment analysis

To support our data, enrichment analysis of metabolic pathways was performed. A high proportion of DEGs fell under unknown categories encoding hypothetical proteins (2–6% genes from 9,765 genes) (**Figure 37A**), and these were the most pronounced DEGs triggered in all exposure conditions at 1 h and 4 h, but these were mostly downregulated (> 50% genes) (**Figure 40**). Previous results also indicated a similar observation, wherein a huge number of hypothetical proteins were activated in a sulfate-reducing bacterium and eukaryotic unicellular ciliate *Tetrahymena thermophila* prior the exposure of CuO NPs (50 and 250 mg/L) and Ag NPs (10 and 20 mg/L) respectively (Chen et al., 2019; Piersanti et al., 2021)

In an agreement with the PCA map, three major clusters (C1, C2, and C3) were identified (**Figure 38**) and the corresponding top 50 DEGs are listed in **Table 9**. These DEGs function mostly as DNA repair, DNA replication, cell growth and death such as minichromosome maintenance protein (MCM 2–7), proliferating cell antigen (PCNA), or cell division cycle (CDC) (**Figure 37A, Figure 37B, Table 9**), as well as ATP/NAD^+/NADPH/NADP/pyruvate activities, porphyrin metabolism which synthesize chlorophyll (*aceA, aceB, glcB, ppdK, acs, chlI, bchI , por, pckA, hemE, hemL*) or genes function in metal ion binding regulating the redox homeostasis suggesting *R. subcapitata* may have high sensitivity to metals such as Fe(III), Fe(II), Ni(II), Zn(II), Cu(II) and others (Suzuki et al., 2018).

(A)

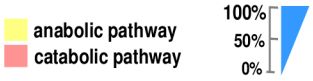

		1h_nFe3O4 Vs 1h_control	1h_nZVI Vs 1h_control	1h_nZVI Vs 1h_nFe3O4	4h_nFe3O4 Vs 4h_control	4h_nZVI Vs 4h_control	4h_nZVI Vs 4h_nFe3O4	Trend
Carbohydrate metabolism	Carbon metabolism (125) [galactose, fructose, mannose]	0	23	18	0	10	6	
	Carbohydrate metabolism (369)	1	13	12	1	5	3	
	Citrate cycle (TCA cycle) (38)	0	13	16	0	8	0	
	Glycolysis / Gluconeogenesis (61)	0	20	18	0	13	8	
	Glyoxylate and dicarboxylate metabolism (22)	0	50	45	0	23	18	
	Pentose and glucuronate interconversions (15)	0	20	7	0	0	0	
	Pentose phosphate pathway (35)	0	9	0	0	0	0	
	Propanoate metabolism (24)	0	17	13	0	13	4	
	Pyruvate metabolism (63)	0	17	17	0	14	8	
	Starch and sucrose metabolism (63)	3	11	13	0	2	2	
Energy metabolism	Carbon fixation in photosynthetic organisms (52)	0	21	15	0	15	8	
	Methane metabolism (9)	0	56	44	0	33	22	
	Mitochondrial biogenesis (134)	0	2	1	0	0	0	
	Nitrogen metabolism (18)	0	17	17	0	6	0	
	Oxidative phosphorylation (17)	0	6	6	0	0	0	
	Photorespiration (4)	0	100	75	0	50	50	
	Photosynthesis (7)	0	0	43	0	14	0	
Lipid metabolism	Fatty acid degradation (13)	0	8	0	0	0	0	
	Fatty acid metabolism (25)	0	36	0	0	0	0	
	Glycerophospholipid metabolism (46)	0	13	15	0	4	4	
	Phytosterol biosynthesis (11)	0	18	9	0	0	0	
	Steroid biosynthesis (34)	0	9	9	0	0	3	
Nucleotide metabolism	Purine metabolism (121)	1	4	3	0	1	2	
	Pyrimidine metabolism (74)	0	5	5	0	0	4	
Amino acid metabolism	Alanine, aspartate and glutamate metabolism (30)	0	13	23	0	3	3	
	Cysteine and methionine metabolism (43)	0	14	16	0	0	2	
	Valine, leucine and isoleucine degradation (23)	0	17	17	0	4	0	
	Metabolism of other amino acids (126)	0	16	16	0	5	2	
	Glutathione metabolism (57)	0	7	7	0	0	4	
Secondary metabolites	Metabolism of cofactors and vitamins (273)	0	12	10	0	1	2	
	Folate biosynthesis (22)	0	23	18	0	0	5	
	Porphyrin metabolism (58)	0	26	21	2	2	0	
	Metabolism of terpenoids and polyketides (135)	1	4	1	0	0	0	
	Carotenoid biosynthesis (63)	0	3	0	0	0	0	
	Xenobiotics biodegradation and metabolism (169)	0	3	4	0	0	2	
	Metabolism of xenobiotics by cytochrome P450 (25)	0	4	8	0	0	0	
Transport and Quorum sensing	Membrane transport (23)	4	35	22	0	13	9	
	ABC transporters (17)	24	35	29	0	12	12	
	Signaling and cellular process (679)	1	9	9	0	3	3	
	Two-component system (11)	9	27	0	0	0	0	
	MAPK signaling pathway - plant (9)	0	100	100	0	33	33	
	Sphingolipid signaling pathway (13)	0	15	8	0	8	8	
	cAMP signaling pathway (14)	0	14	21	0	7	7	
	Plant hormone signal transduction (5)	0	40	60	0	0	0	
	Environmental adaptation (93)	0	4	3	0	0	0	
Cellular Processes	Transport and catabolism (133)	2	5	5	0	2	1	
	Cell growth and death (101)	1	30	27	0	6	14	
	Cell cycle (54)	0	48	43	0	9	22	
	Cellular senescence (23)	0	17	13	0	4	4	
	Motility associated protein (160)	1	13	11	0	4	4	
Other	Hypothetical protein (9765)	0	6	5	0	2	2	
	Unclassified: metabolism (8268)	1	6	5	0	2	2	

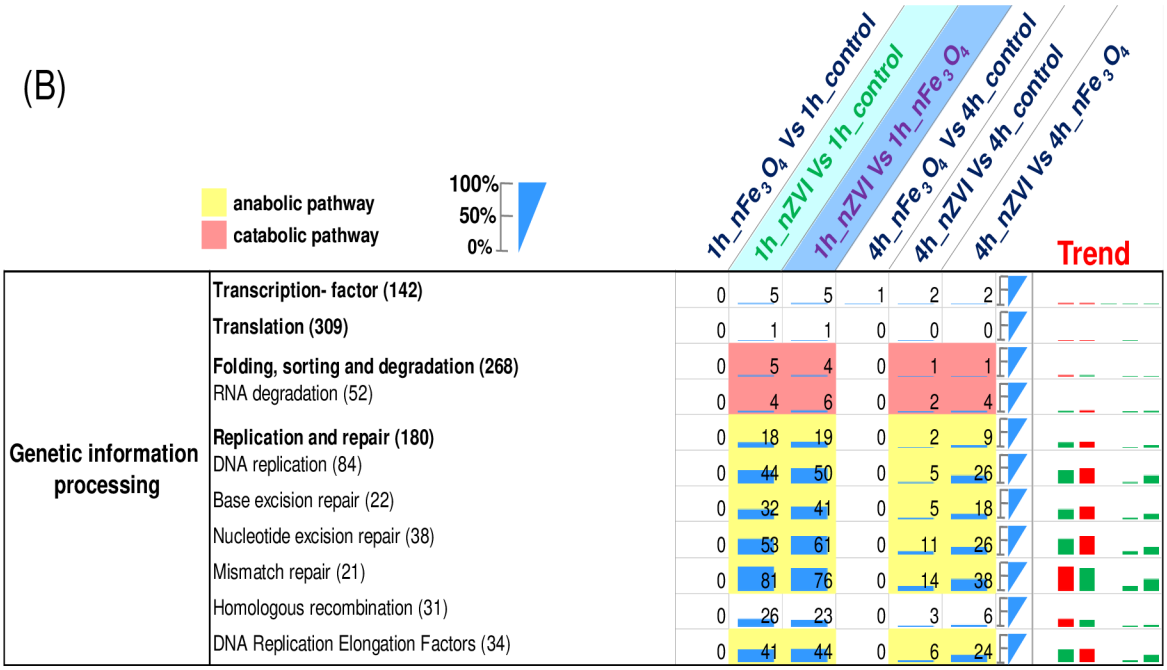

Figure 37. A summary of enriched functional categories regulated in *R. subcapitata* genome after the exposure of nFe_3O_4 and nZVI. Pairwise comparison was applied comparing the gene expression between conditions. DEGs representing the compared treatments that were up-regulated in either nZVI or nFe_3O_4 versus control or different treatment condition (down-regulation). (A) Overview abundance of functional categories triggered in *R. subcapitata*. (B) Highly regulated pathways defined by their expression in percentage abundance, genetic information processing in *R. subcapitata*. Numbers in the parentheses represent the total number of genes classified per KEGG pathway. Numbers in each individual cell represent the percentage of total number of DEGs ($\log_2$ [fold change] ≥ 1.5 and ≤ -1.5 or ≤ -1.8) ($P < 0.05$) identified in *R. subcapitata* exposed to nZVI or nFe_3O_4 versus control or different treatment condition. Control = *R. subcapitata* without NPs exposure. Red bars in the trend column represent highest point.

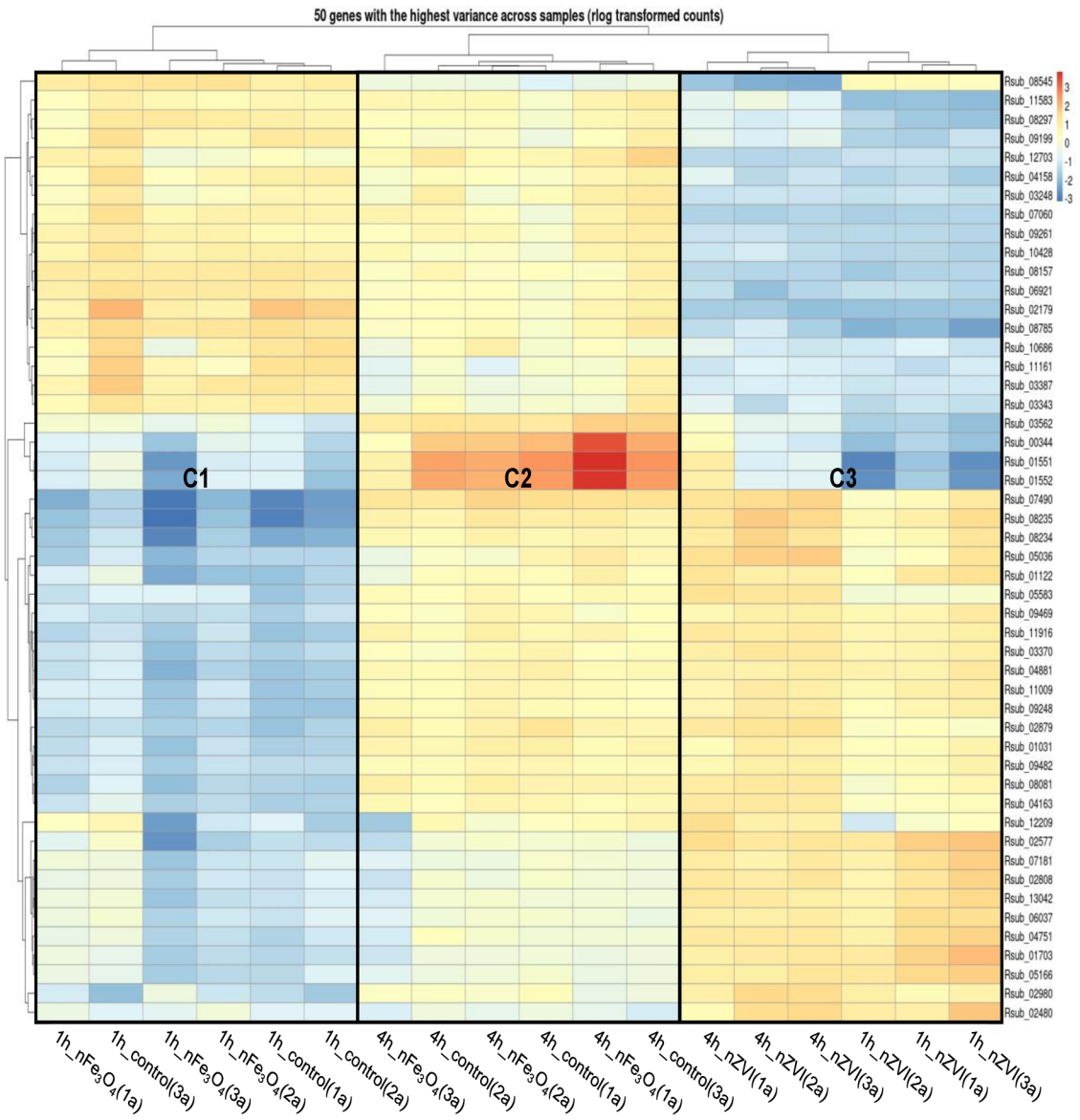

Figure 38. Heatmap of the top 50 DEGs in different exposure conditions. Hierarchical clustering of genes was based on the $\log_2$-fold change, and the adjusted P-value was based on the 95% confidence interval. Cluster C1 contained the samples from *R. subcapitata* in nFe_3O_4 treatment and control condition at 1 h; cluster C2 represented the *R. subcapitata* in nFe_3O_4 treatment and control condition at 4 h, whereas cluster C3 consisted of the samples of *R. subcapitata* in nZVI at 1 and 4 h. Relative gene expression is indicated by the color scales: elevated gene expression > 0 indicates upregulation in treatment conditions (*R. subcapitata* in nZVI or nFe_3O_4) (red), reduced gene expression, shown in blue, < 0 indicates upregulation in control. Control was *R. subcapitata* only. See **Table 9** for details.

Table 9. Top 50 DEGs in *R. subcapitata* exposed to nFe_3O_4 and nZVI after 1 and 4 hours. A summary of genes grouped by metabolic pathways and by functional classification using KEGG, PhycoCosm, PSOS alpha and UniProtKB databases. Genes that fell under unknown annotation were submitted to individual PSOS searches, and the annotation with the highest score and homology identity were used as the functional classification. (1) 1h_nFe_3O_4 Vs 1h_control; (2) 1h_nZVI Vs 1h_control; (3) 1h_nZVI Vs 1h_nFe_3O_4; (4) 4h_nFe_3O_4 Vs 4h_control; (5) 4h_nZVI Vs 4h_control (6) 4h_nZVI Vs 4h_nFe_3O_4. Same legend also corresponds to labels in (**Figure 37**, **Figure 40**).

no	Gene locus	Pathway ID	Pathway	Gen/e	Functional description	P value	log_2 (fold change) gene expression by treatment type					
							1 h			4 h		
							1	2	3	4	5	6
1	Rsub_08545	-	-	-	Chloroplast, mRNA processing, DNA binding, transcription regulation	4.97×10^{-122}					−2.07	−2.06
2	Rsub_11583	-	-	-	Hypersensitive-induced response protein (e.g.: cell death, potassium ion regulation)	6.10×10^{-34}		−3.53	−3.25			
3	Rsub_08297	-	-	-	cell redox homeostasis, catalyze NADPH-dependent reduction of coenzyme A disulfide, NADP binding	7.42×10^{-46}		−3.72	−3.60		−1.72	−1.67
4	Rsub_09199	K01638	Pyruvate metabolism, Glyoxylate and dicarboxylate metabolism, carbohydrate metabolism	*aceB, glcB*	malate synthase	6.17×10^{-19}		−3.86	−3.05			

5	Rsub_12703	-	-	-	Polyvinyl alcohol (PVA) dehydrogenase (cytochrome activity), heme binding, oxidoreductase activity	1.35×10^{-79}	−2.75	−2.43	−3.25	−2.77
6	Rsub_04158	-	Cofactor biosynthesis	-	4–hydroxythreonine–4–phosphate dehydrogenase, metal ion binding, NAD binding	1.04×10^{-53}	−3.75	−3.04	−2.02	−1.86
7	Rsub_03248	K05300	Amino acid degradation	-	Oxidoreductases activity, L–amino acid dehydrogenase, metal ion binding	4.25×10^{-67}	−4.65	−4.00	−3.83	−3.35
8	Rsub_07060	-	-	-	Keratin-associated protein	1.61×10^{-80}	−4.35	−3.89	−3.41	−3.26
9	Rsub_09261	K14944	Genetic information processing	*NOVA*	Spliceosome, RNA-binding protein Nova	2.00×10^{-75}	−4.35	−4.23	−3.26	−3.17
10	Rsub_10428	-	-	-	Regulator of chromosome condensation (RCC1) family protein, ATP binding	2.36×10^{-49}	−4.20	−3.85	−2.49	−2.58
11	Rsub_08157	K01006	Energy metabolism, Pyruvate metabolism, Carbon fixation in photosynthetic organisms, carbohydrate metabolism	*ppdK*	Phosphotransferases with paired acceptors pyruvate phosphate dikinase, metal ion binding	5.65×10^{-112}	−4.79	−4.61	−3.37	−2.99
12	Rsub_06921	-	-	-	iron ion homeostasis	4.33×10^{-94}	−2.66	−2.58	−2.03	−1.98
13	Rsub_02179	K01637	Glyoxylate and dicarboxylate metabolism, Carbon metabolism, carbohydrate metabolism	*aceA*	Carbon–carbon lyases, isocitrate lyase, metal ion binding	1.24×10^{-138}	−3.88	−2.80	−2.40	−2.25

14	Rsub_08785	K01895	energy metabolism, Pyruvate metabolism, Propanoate metabolism, Methane metabolism, Carbon fixation pathways in prokaryotes, carbohydrate metabolism	*acs*	acetyl–Coenzyme A synthetase, lipid biosynthesis proteins, Methanogenesis, acetate => methane, ATP binding	3.84×10^{-92}	−4.39	−3.97	−2.25	−2.06
15	Rsub_10686	-	-	-	ATP-dependent DNA helicase, DNA damage and repair, ATP binding and hydrolysis activity	1.99×10^{-20}	−3.06	−1.90	−1.60	−1.81
16	Rsub_11161	K01610	energy metabolism, Citrate cycle (TCA cycle), pyruvate metabolism, Carbon fixation in photosynthetic organisms, carbohydrate metabolism	*pckA*	Carbon–carbon lyases, phosphoenolpyruvate carboxykinase (ATP), oxaloacetate => fructose–6P, ATP binding	2.40×10^{-32}	−3.78	−2.59	−1.82	
17	Rsub_03387	-	Lipid metabolism	-	Lipase chaperone, ATP binding, lipid catabolic process	1.33×10^{-27}	−7.77	−7.13	−3.36	−2.50
18	Rsub_03343	-	Amino acid degradation	-	Arginine deiminase	3.24×10^{-54}	−2.91	−2.42	−1.87	
19	Rsub_03562	-	Lipid metabolism	-	Sterol regulatory element-binding protein 1	1.04×10^{-23}		−1.92	−1.63	−1.64
20	Rsub_00344	-	-	-	DNA Replication termination factor 2	7.61×10^{-12}	−2.63	−2.27	−2.48	−2.83
21	Rsub_01551	-	-	-	metallopeptidase activity, metal ion binding hemostasis	5.96×10^{-11}	−2.46	−1.97	−2.50	−2.78
22	Rsub_01552	-	-	-	metallopeptidase activity, metal ion binding hemostasis	3.95×10^{-10}	−2.34	−1.87	−2.43	−2.73

23	Rsub_07490	K01599	Porphyrin metabolism	*hemE,*	Heme biosynthesis, glutamate => heme	1.10×10^{-59}	3.04	3.36
24	Rsub_08235	K00218	Porphyrin metabolism, Metabolism of cofactors and vitamins	*por*	With NAD+ or NADP+ as acceptor, NADPH–protochlorophyllide oxidoreductase	4.66×10^{-5}	3.18	3.33
25	Rsub_08234	-	-	-	Basic proline-rich protein-like	2.07×10^{-5}	2.88	3.12
26	Rsub_05036	K00549	amino acid metabolism, Cysteine and methionine metabolism,	*metE*	amino acid synthesis, Methionine biosynthesis,	2.86×10^{-10}	1.89	2.43
27	Rsub_01122	K00558	amino acid metabolism, Cysteine and methionine metabolism	*DNMT1, dcm*	DNA Replication Termination Factors	3.67×10^{-4}	2.19	2.68
28	Rsub_05583	-	-	-	putative ion transmembrane transport, metal ion binding, ATP binding, 4 iron, 4 sulfur cluster binding, electron transfer activity	1.02×10^{-29}	1.56	
29	Rsub_09469	-	-	-	Small integral membrane protein, chloroplast	3.92×10^{-3}	3.00	2.84
30	Rsub_11916	-	-	-	Transcriptional activator Myb, ATP binding, DNA binding transcription factor activity	7.27×10^{-17}	3.77	3.26
31	Rsub_03370	-	-	-	NAD(P) domain-containing protein	2.77×10^{-11}	2.34	2.49
32	Rsub_04881	-	-	-	Uncharacterized protein, possible involved in glutamine metabolic process	3.65×10^{-3}	2.49	2.65
33	Rsub_11009	-	Porphyrin metabolism	-	Uroporphyrinogen decarboxylase	5.86×10^{-4}	2.51	2.33

34	Rsub_09248	-	-	-	ANK_REP_REGION domain-containing protein, involved in the regulation or degradation of hydrogen peroxide levels during stress. Regulates ascorbate peroxidase 3 (APX3) and peroxisome activity.	7.55×10^{-6}		2.29	2.20		
35	Rsub_02879	-	-	-	Photosystem II, photosynthesis, chloroplast thylakoid membrane	3.62×10^{-8}		1.89	1.84		
36	Rsub_01031	K03405	Porphyrin metabolism, Metabolism of cofactors and vitamins	*chlI, bchI*	magnesium chelatase, ATP binding, chlorophyll biosynthesis	3.38×10^{-75}		2.00	2.12		
37	Rsub_09482	K01845	Porphyrin metabolism,	*hemL*	Biosynthesis of cofactors, Heme biosynthesis, Siroheme biosynthesis	1.03×10^{-4}		1.80	2.00		
38	Rsub_08081	-	-	-	tRNA binding domain containing protein, ATP binding, methionine–tRNA ligase activity	1.2×10^{-4}		1.99	2.28		
39	Rsub_04163	K08901	Energy metabolism, Photosynthesis, Photosystem and electron transport system, Photosystem II (P680 chlorophyll a)	*psbQ*	photosynthesis proteins, Photosystem and electron transport system, photosystem II oxygen-evolving enhancer protein 3	5.64×10^{-10}			1.71		
40	Rsub_12209	-	-	-	HMG box domain-containing protein, DNA binding, repair	4.57×10^{-3}	−0.87			0.8	1.17
41	Rsub_02577	K04802	DNA replication and repair Base excision repair Nucleotide excision repair Mismatch repair	*PCNA*	Genetic Information Processing Cell growth and death; This protein is an auxiliary protein of DNA polymerase delta and is involved in the control of eukaryotic DNA replication by increasing the polymerase's	6.37×10^{-12}		2.38	3.18	1.53	1.71

					processibility during elongation of the leading strand					
42	Rsub_07181	K02212	DNA replication and repair Cell cycle, DNA helicase	*MCM4. CDC54*	Genetic Information Processing DNA replication licensing factor MCM4, CDC54; Cell growth and death	2.76×10^{-13}		2.54	2.85	1.51
43	Rsub_02808	K10807	nucleotide metabolism, purine metabolism, Pyrimidine metabolism, Glutathione metabolism, DNA repair and recombination proteins	*RRM1*	photosystem II oxygen-evolving enhancer protein 3, Pyrimidine deoxyribonucleotide biosynthesis, UDP => dTTP, Deoxyribonucleotide biosynthesis, Ribonucleoside–diphosphate reductase; Provides the precursors necessary for DNA synthesis. Catalyzes the biosynthesis of deoxyribonucleotides from the corresponding ribonucleotides.	2.18×10^{-14}		2.07	2.42	1.64
44	Rsub_13042	K10808	nucleotide metabolism, purine metabolism, Pyrimidine metabolism, Glutathione metabolism, DNA repair and recombination proteins	*RRM2*	Cell growth and death, ribonucleoside–diphosphate reductase subunit M2, Pyrimidine deoxyribonucleotide biosynthesis,	1.03×10^{-10}		2.09	2.75	1.55
45	Rsub_06037	K02210	DNA replication and repair Cell cycle, DNA helicase	*MCM7, CDC47*	Genetic Information Processing DNA replication licensing factor MCM7, CDC47; Cell growth and death	4.63×10^{-11}		2.33	2.82	

46	Rsub_04751	K02209	DNA replication and repair Cell cycle, DNA helicase	*MCM5, CDC46*	Genetic Information Processing DNA replication licensing factor MCM5, CDC46; Cell growth and death,	8.32×10^{-10}	2.39	2.89		1.50
47	Rsub_01703	K02540	DNA replication and repair Cell cycle, DNA helicase	*MCM2*	Genetic Information Processing DNA replication licensing factor MCM2 Cell growth and death	5.37×10^{-16}	3.03	3.08		1.81
48	Rsub_05166	K02542	DNA replication and repair Cell cycle, DNA helicase	*MCM6*	Genetic Information Processing DNA replication licensing factor MCM6 Cell growth and death,	1.63×10^{-15}	2.67	2.91		1.56
49	Rsub_02980	-	-	-	Protein transport, metal ion binding	3.68×10^{-21}	2.87	1.80		
50	Rsub_02480	K00600	amino acid metabolism, energy metabolism, carbohydrate metabolism, methane metabolism	*glyA, SHMT*	Photorespiration, glycine hydroxymethyltransferase, Interconversion of serine and glycine	1.91×10^{-44}	2.26	1.94	1.81	1.99

*DEGs representing the compared treatments that were up-regulated ($\log_2$ FC > 0) in either nZVI or nFe_3O_4 versus other treatment conditions ($\log_2$ FC < 0). NOTE: control = *R. subcapitata* without NPs exposure. Color with a darker hue indicates higher gene expression value in the treatments condition.

4.9.5 nZVI deactivate genes involved in carbohydrate metabolism, energy metabolism and transmembrane signaling

As demonstrated by previous results in section **4.4.4**, we originally expected a high capability of *R. subcapitata* to interconnect energy-fueled glutathione system in order to detoxify ROS (Yeap et al., 2022). Surprisingly, exposure to nZVI did not upregulate antioxidant regulators such as superoxide dismutase (SOD), ascorbate peroxidase (APx), catalase (kat) nor glutathione (GST, ggt) in *R. subcapitata*, but also downregulated a high number DEGs in carbohydrate-energy metabolisms including photorespiration, and transmembrane transport, partly linked to a plethora effects of energy metabolism and mitochondria signaling with their auxiliary redox partners (iron ion and NADPH) to regulate electro-chemical proton gradient across membrane (Hannemann et al., 2007; Stavropoulou et al., 2018; Wikström et al., 2018) (**Figure 37A**, **Figure 40**, **Table 9**). Within 1 h, the downregulation of carbohydrate metabolism and signaling transporters (quorum sensing) were most evident, rapidly suppressing 53 genes in nZVI when compared to control, and 54 genes in nZVI when compared to nFe_3O_4 (**Figure 40**). These signaling transporters function as metal ion binding/transportation, catalytic electron transfer for redox equivalent, or NADPH–cytochrome P450 reductase for detoxification functions (**Table 9**). Cytochrome P450 reductase is a membrane bound protein located in inner mitochondria membrane which require NADPH, iron–sulfur protein and oxygen to initiate electron transfer and detoxification mechanisms (Hannemann et al., 2007; Peter Guengerich, 2001). Therefore, the deactivation of these regulators could be an indicative of an impaired mitochondria membrane potential, lower carbohydrate burnout, decreased electron transfer and then depletion of NADPH/ATP conserves. These observations clearly demonstrated that mitochondria have a tight control over oxidative stress in the event of high Fe^{2+}/Fe^{3+} fluxes or presence of environmental stressors to ease cell stress. Hence, any number of triggers can impact the energy flow and the dysfunction of these mechanistic events will then lead to cell senescence or apoptosis (J. Niemuth et al., 2021; Peter Guengerich, 2001; Yeo and Pak, 2008; Zhao et al., 2022). Moreover, photorespiration also functions in the redox states of NADPH and NADP conserves, to mainly supply NADPH for mitochondria (Lim et al., 2020). Almost 50–100% of genes function in photorespiration were identified as

DEGs in the cells exposed to nZVI (**Figure 37A**), however, the down-regulation of mitochondria also deactivated photorespiration (**Figure 40**). The down-regulation of these pathways explained well the lower NPQ and dissolved oxygen (higher CO_2) (**Figure 25B, 25D**), pointing out the regulatory circuit in between electron transport chain in chloroplasts and mitochondria. A rapid drop of the light availability due to nZVI, therefore led to reduced photon capture capacity by the light harvesting complex (LHC), yielding lower stromal ATP/NADPH production, then impacted the downstream metabolic pathways that consume ATP/NADPH via Calvin–Benson–Bassham cycle for photosynthetic carbon fixation (Lucker and Kramer, 2013; Shameer et al., 2019). As an immediate response to the onset of deprived ATP/NADPH, NPQ was dynamically repressed which in turn increased the photosynthetic efficiency (photosystem I/II) to replenish the ATP/NADPH shortage, and within 4 h, including the activation of cytochrome 6 (**Table 9**, **Figure 39**).

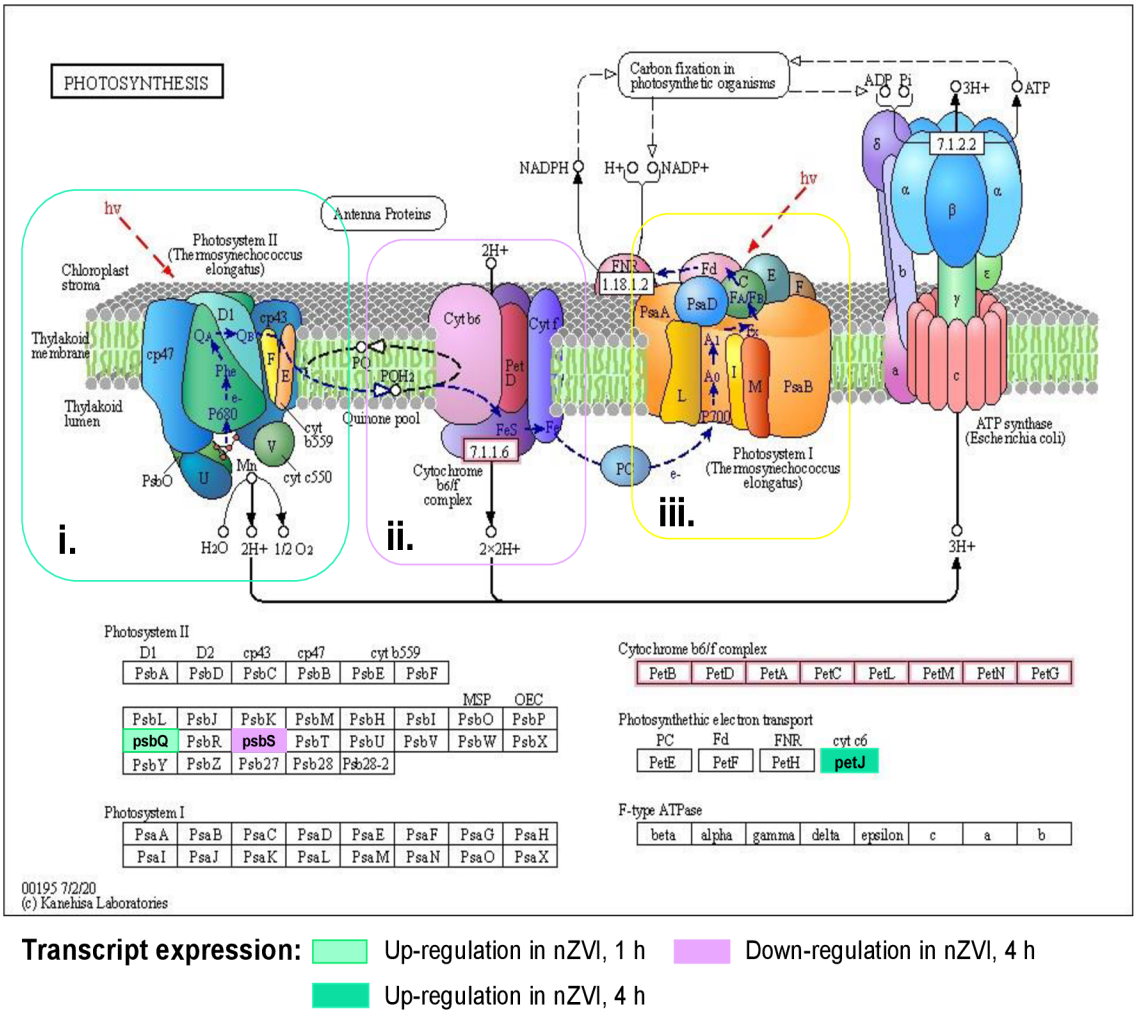

Transcript expression: Up-regulation in nZVI, 1 h Down-regulation in nZVI, 4 h Up-regulation in nZVI, 4 h

Figure 39. KEGG pathway map of photosynthesis and the electron transport chain upon 1 and 4 h exposure in nZVI condition. The map was retrieved from https://www.genome.jp/pathway/map00195. i.) photosystem II, ii) cytochrome, iii) photosystem I. The green colored boxes show the up-regulation of transcripts in nZVI treatment at 1 and 4 h, while purple colored box showed the down-regulation of transcript at 1 h. NOTE: Boxes and map without coloring are the original version retrieved from the KEGG database.

To note, nFe_3O_4 lowered the NPQ physically, but did not trigger these underlying energetic functions, which may be due to higher reactivity of nZVI to release Fe^{2+} and increase ROS, whereas nFe_3O_4 did not. This is strongly suggesting that combined effects of nZVI (shading and the release of Fe^{2+}) disrupted the electron flow and deactivated various energetics events. Recent studies showed the activation of the carbohydrate-energetic metabolism such as TCA cycle in bacteria by dissolved iron from nZVI (44.5 µg/mL) (Yeap et al., 2022) and in earthworm by the nZVI exposure (10g/kg) (Zhang et

al., 2021), however, they were activated at a later time after 1 day and 28 days respectively.

4.9.6 nZVI activates genes involved in DNA replication and repair

After 1 h of exposure to nZVI (but not to nFe_3O_4), a number of DEGs function in genetic information processing and a myriad effect of DNA repairs were triggered (**Figure 37B**, **Table 9**), suggesting these repair pathways could function as a sentinel protective response from the onset of any stress detected (Wang et al., 2022). These repair pathways predominate the DNA replication (44–50%), nucleotide excision repair (53–61%), mismatch repair (76–81%), DNA replication elongation factors (41–44%) and others (**Figure 37B**). Taken together, the total number of DEGs in repair pathways that were activated within 1 h by nZVI included: 121 genes (116 upregulated, 5 downregulated) in the group nZVI versus control; 132 genes (129 upregulated, 3 downregulated) in the group nZVI versus nFe_3O_4 (**Figure 40**). Within a few hours later (4 h), these activated DEGs reduced to a staggering level (~51–85% reduction), only 18 and 64 DEGs were detected in the same treatments. DNA damage is an instant threat as DNA could be susceptible to attack by various environmental factors, such as UV-radiation, ROS, pathogen infection, DNA replication error, carcinogenic compounds (Xie et al., 2020; Yousefzadeh et al., 2021). Once detected, if not repaired immediately, could interfered with cascade signaling of regulatory circuit, if necessary, energy metabolism could be reprogrammed to signal cell apoptosis (Milanese et al., 2019). To arm against attack and maintain genome integrity, organisms developed different spectrum of DNA repairs tailored to different types of stressors. They include base excision repair (BER), nucleotide excision repair (NER), mismatch repair (MMR), homologous recombination (HR) (Chatterjee and Walker, 2017). BER is considered to be the dominating approach targeting the DNA single strand break from ROS (David et al., 2007) while NER is mainly function to remove bulky DNA lesion/adducts caused by various chemical agents such as polycyclic aromatic hydrocarbons (Schärer, 2013). In all likelihood, nFe_3O_4 did not lead to these repair pathways, whereas the reactive iron species released from nZVI could be the causal agent leading DNA damage, then eventually resulted a pronounced effect of DNA repair. Of note, the energy costs for maintenance overrides its supply during severe stress. Hence, boosting the cellular ATP

/NADPH has protective effects in the event of DNA damage due to enhancement of antioxidant activity (James et al., 2015; Kitabatake et al., 2020; Zhao et al., 2022). Although our data demonstrated a huge deactivation of energetics signaling at 1 h, this could indicate the dynamic shift of the energy demand which controls prooxidant-antioxidant balance since transcriptional activation could change quickly even within minutes (Blifernez-Klassen et al., 2021).

Another explanation for these down-regulation of energetics events in the nZVI exposure could also be due to the NADPH consumption accompanied by the elevation of p53 protein during oxidative stress-induced DNA damage (Cucchi et al., 2021; Shi et al., 2021). p53 which is also a NADPH suppressor, is known to be the checkpoint which detects DNA damage and is often involved in DNA damage response, was up-regulated at 1 h (data not shown), including the prevailing expression of DNA replication proteins (MCMs) (**Table 9**). When the DNA damage intensity is mild, p53 could signal DNA repair, cell survival and replication. However, when the damage is beyond repair, p53 could signal for apoptosis (Surjana et al., 2010). Given that, persistent activation of p53 protein depletes ATP/NADPH, down-regulates a series of carbohydrate metabolisms such as pentose phosphate pathway (PPP), glycolysis and then lower carbohydrate assimilation (Jiang et al., 2011). As a consequence, carbohydrate-energy metabolism could progressively be linked to DNA repair in order to reduce the stigma around oxidative stress, DNA damage, and then signal to boost ATP/NADPH production for DNA repair.

To support the notion of our data, protein–protein interaction (PPI) analysis was performed in conjunction using the co-expression data extracted from RNA-seq to predict the functional interaction of genes or proteins (Szklarczyk et al., 2018). PPI analysis revealed the interconnection between the central carbohydrate metabolism pathway (PPP, glycolysis, TCA cycle, pyruvate), DNA replication repair activity and porphyrin metabolism (**Figure 41**). The interrelationship between the replication proteins (MCMs, PCNA) and reducing equivalents (ATP, NAD^+, NADPH) may show linkages working among each during the oxidative stress challenges.

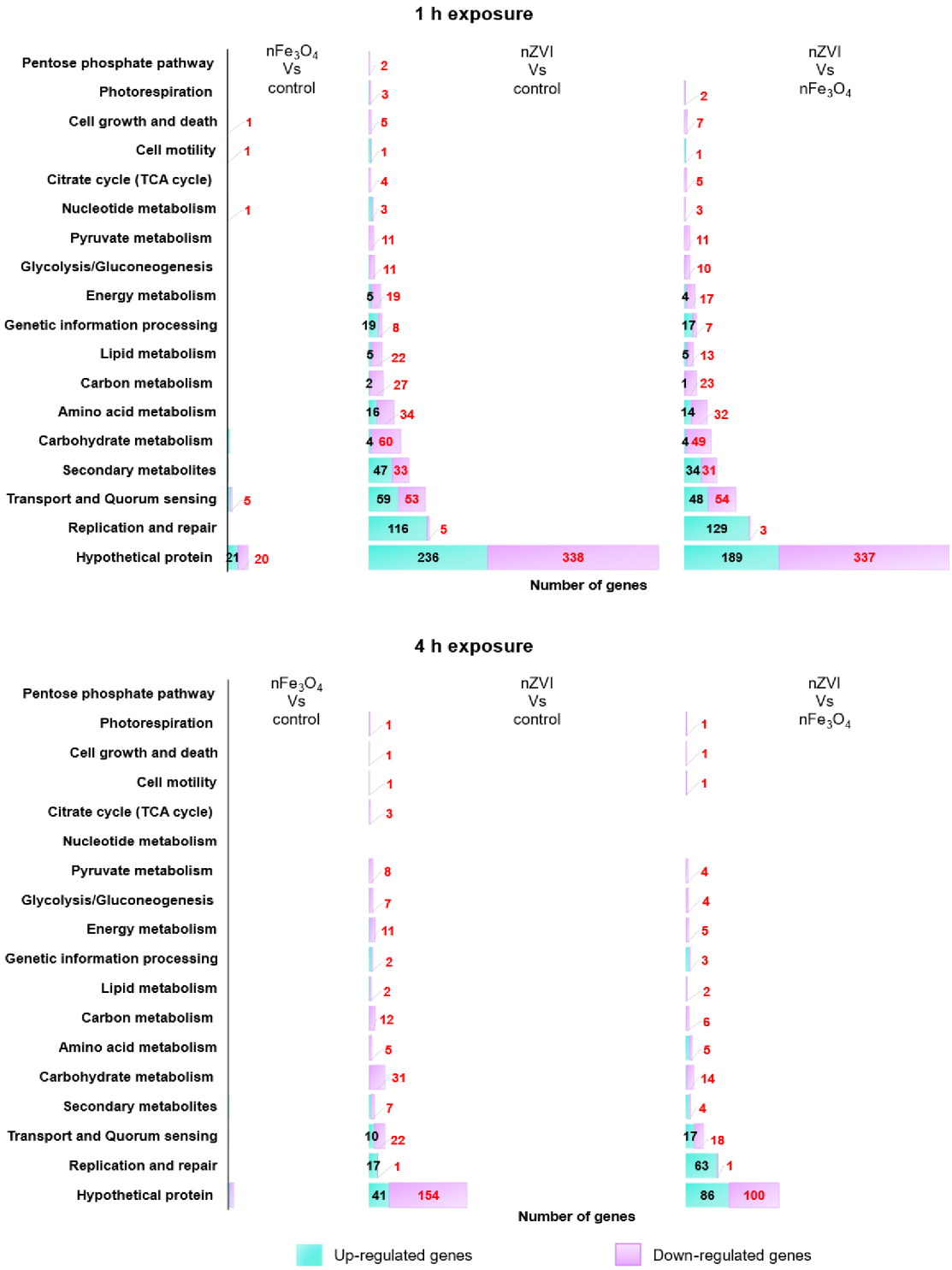

Figure 40. An overview numbers of differentially expressed genes ($\log_2$ [fold change] ≥1.5 and ≤ −1.5 or ≤ −1.8) ($P < 0.05$) in *R. subcapitata* exposed to nZVI or nFe_3O_4 versus different treatment condition classified by metabolic pathways and functional groups using KEGG, PhycoCosm and UniProtKB databases. DEGs representing the compared treatments that were up-regulated in either nZVI or nFe_3O_4 versus other treatment conditions. Control = *R.*

subcapitata without nanoparticle exposure. Fonts in red represent the number of down-regulated genes while fonts in black represent number of up-regulated genes.

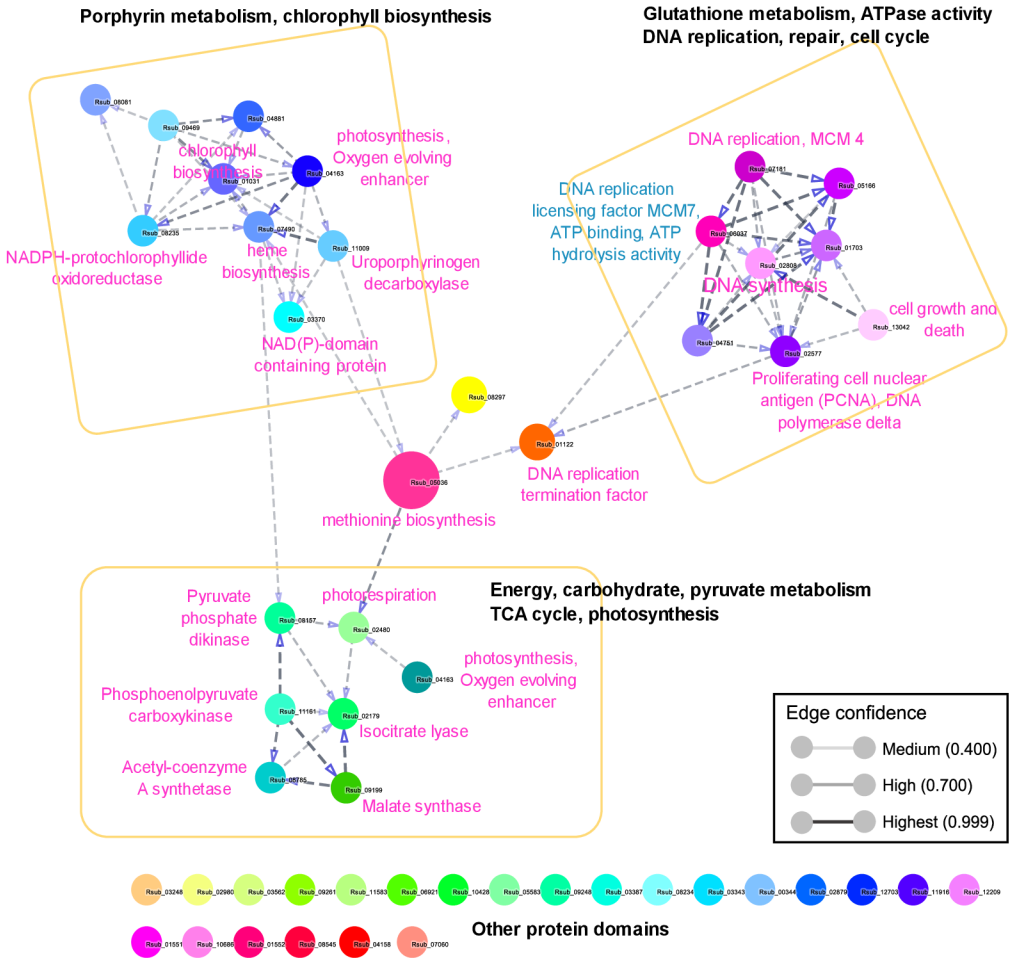

Figure 41. Co-expression analysis of top 50 DEGs for protein-protein interaction networks in *R. subcapitata* which responded to the treatment of nFe_3O_4 and nZVI. Colors of the nodes represent a specific metabolic pathway or single protein domain: (i) blue nodes- Porphyrin metabolism, chlorophyll biosynthesis; (ii) purple nodes- glutathione metabolism, ATPase activity, DNA replication, repair and cell cycle; (iii) green nodes- energy, carbohydrate, pyruvate metabolism, TCA cycle, photosynthesis; (iv) multiple colors/nodes in a line- a group of protein domains whose function is unrelated to any of the metabolic pathways in this network. The thickness of the edges/lines connecting nodes indicate the strength of the data support as shown in the legend above. Each node represents a protein produced by a single gene locus. TCA cycle- tricarboxylic acid cycle

In the present study, we have set up a system to explore the toxicity difference between reactive nZVI and non-reactive nFe_3O_4 following their exposure to microalgae. The results provide a comprehensive view on the stress response in *R. subcapitata* and

support the knowledge on circuit-wide adaptation on cytosolic stress. nZVI, but not nFe_3O_4, showed to posed higher inhibition effect in *R. subcapitata* in its viability earlier in the exposure, accompanied by the massive regulations of DNA rescue within 1 h, while interfered various central carbohydrate metabolisms and transmembrane signaling involved in external sensing. This circuit implicated the sentinel response in *R. subcapitata* to trigger a spectrum of DNA repair response within 1 h, revealing the role of energy homeostasis and associated trade-offs in survival and stress tolerance. Therefore, the level of energy conserves (ATP/NADPH/NAD^+) in microorganisms is expected to reflect the toxicity of nZVI in a straightforward manner.

III. *C. reinhardtii*

Study on *C. reinhardtii* focused only on the physiological endpoints such as cell morphology, chlorophyll fluorescence, total viable cell count, and phytochrome content. Transcriptomic analysis was not included, because the main focus was on *R. subcapitata* that is considered as model organism in OECD ecotoxicity studies (TG 201).

4.10 Morphology changes of cells upon NPs exposure

The light microcopy images (**Figure 42**) show different cell stages and interaction between algal cells and NPs. The cells in the control had intact plasma membrane and the cell wall with two flagellar (**Figure 42, A1–A3**), and new cells started to divide after 24 h (**Figure 42, A4**). A strong NPs attachment on algae was observed from time zero (**Figure 42, B1, C1**), and cells were slightly deformed or lysed which was observed from 48 h (**Figure 42, B5, C5**) or cell lost their chlorophyll leaving empty cells/cell debris behind (**Figure 42, C2**). Such a cell alteration also appeared in a previous study (Lei et al., 2016). At immediate exposure, there was small degree of chlorophyll lost in nFe_3O_4 indicated by the yellow arrows which was not seen in nZVI exposure.

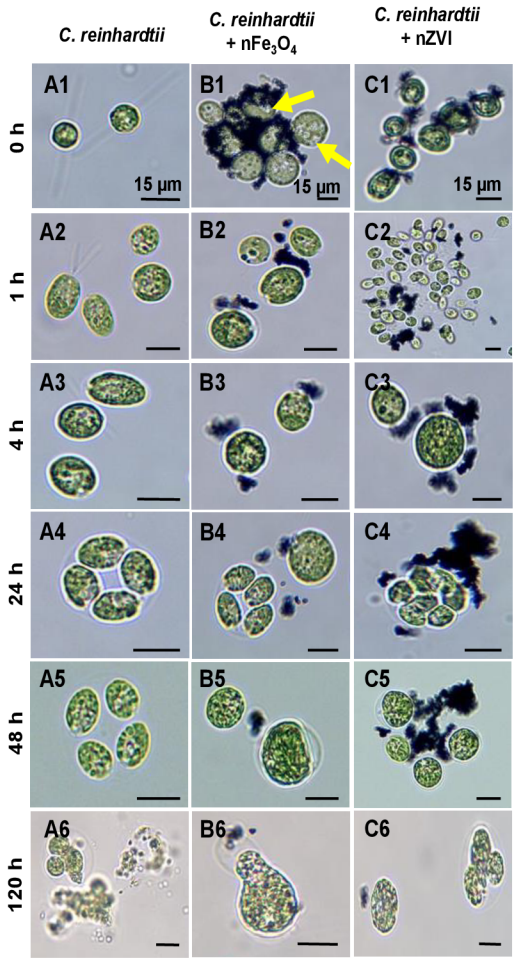

Figure 42. Microscopic image of *C. reinhardtii* exposed to nFe_3O_4 and nZVI up to 120 h. (A) Untreated *C. reinhardtii*; (B) *C. reinhardtii* exposed to 100 mg/L nFe_3O_4 (C) *C. reinhardtii* exposed to 100 mg/L nZVI. Scale bar = as indicated in the pictures (15 µm).

4.11 Phenotype responses

The overall phenotypic responses of *C. reinhardtii* was not statistically significant until 24 h (**Figure 43A–2D**), except NPQ (**Figure 43E**). In the nZVI samples, the NPQ value was the lowest comparing three exposure conditions and was significantly affected within 1 h, and these NPQ values continued to decrease until 48 h, and thereafter increased sharply by 120 h, suggesting that cells may be under stress from the initial NPs exposure while were able to recover after several days. Phenotypic results summarized in (**Figure 43**) display almost no detrimental effect of NPs to *C. reinhardtii*, as their values are similar to control condition. Furthermore, the lower fluorescence intensity of photosystem II observed in both NPs treatments could be partly due to the shading effect of NPs (**Figure 43F**), whereas *C. reinhardtii* almost regained its

photosystem II activity after 120 h. Exposure to NPs would also caused oxidative stress or DNA damage in cells, due to the oxidation of nZVI and generation of hydroxyl radical (Ševců et al., 2011). Standard toxicity endpoints are depending mostly on the phenotypic responses of microorganisms such as growth inhibition, or oxidative stress formation. To comprehend the underlying stress beneath the cell membrane on how the cell would defend oxidative insults, more toxicity endpoints are needed for evaluation, such as transcriptomic analysis to better reveal hidden pattern of cell defense (Guo et al., 2020; Yeap et al., 2022).

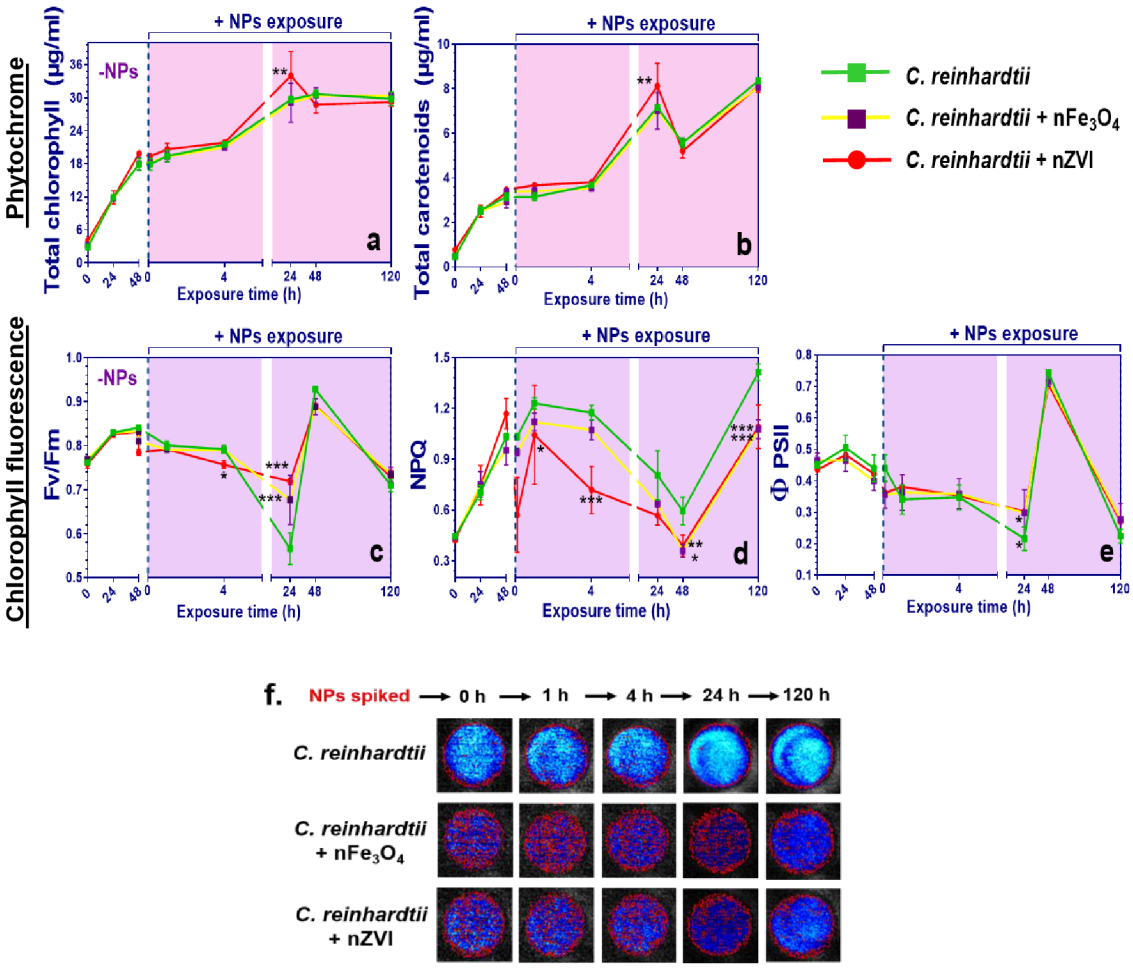

Figure 43. Phenotypic responses of *C. reinhardtii* exposed with nZVI and nFe_3O_4 in HSM. (A, B) Phytochrome content (Total chlorophyll and carotenoid); (C, D, E) Chlorophyll fluorescence [Maximum PSII yield (F_v/F_m), non-photochemical quenching (NPQ), effective PSII yield (Φ PSII)] (mean ± SD; n = 3); (F) Light intensity of chlorophyll fluorescence imaged under FluorCam FC 800-C Video Imager. *= level of significance changes were compared to untreated

exposure medium containing only *C. reinhardtii* (*C. reinhardtii,* solid green line), (*P< 0.05, **P < 0.001, ***P < 0.0001). Note: different scales for the *y*-axis.

4.12 Cell viability

The effect of both NPs on *C. reinhardtii* cells was assessed by counting the viable cell (intact cell) and dead cell (cell lost its pigment/plasmolyzed cells) and the results are shown in (**Figure 44**). Both NPs inhibited the algae cell as observed by the reduction of cell viability, however, in a different mode of action. The cell viability in the control was stable with more than 80% viable cells during the whole experiment (**Figure 44A**). nFe_3O_4 caused a decrease in viability by 10% comparing to the control, approximately 69% viable cells were recorded after one hour and this proportion persisted until the end of the study (**Figure 44B**). Effect of nZVI was rather slow and the highest proportion of dead cells occurred after 48 h – 30% decrease in viability comparing to control (**Figure 44C**).

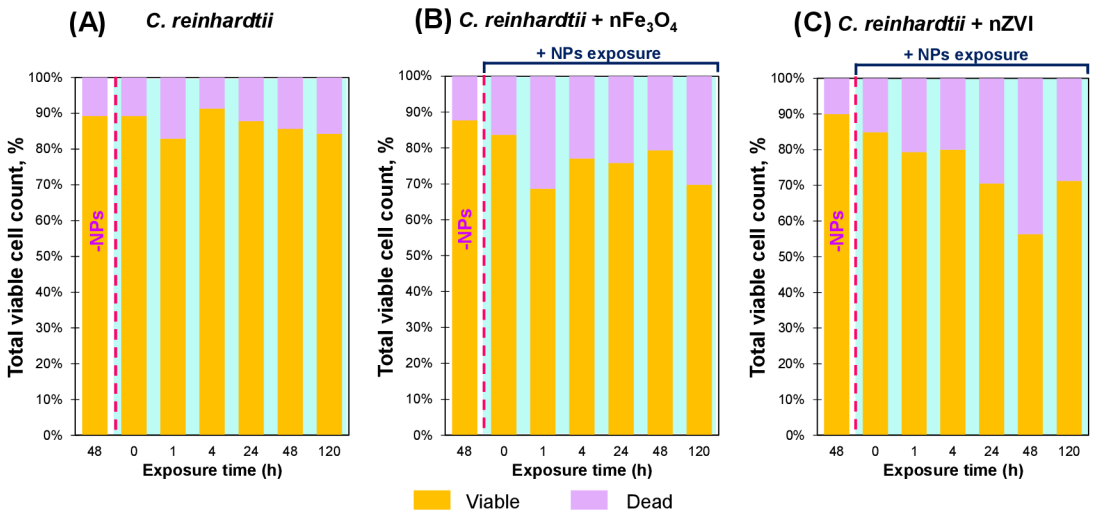

Figure 44. Total viable intact cells and dead cells, determined by manual counting using hemocytometer under light microscope. Values were expressed in percentage, (mean; n = 3).

Iron NPs caused minor negative effect to *C. reinhardtii* during the initial hours of exposure, while the culture was able to recover towards to the end of the study, probably due to nZVI oxidation, which turned in harmless iron oxides and unaffected new cell generations. This study amends the current knowledge about the potential risks of nZVI application in the environment.

5. Conclusion

A unique experimental system was set up to explore the interplay between bacterial and algal cells and nZVI, nFe_3O_4, or dissolved iron released directly from NPs. Although cell viability of *P. putida* was not affected by neither NPs nor dissolved iron, RNA sequencing data provided a detailed view of the stress response. Exposure to dissolved iron (44.5 µg/L), but not to nZVI, led to an avalanche of gene expression for many metabolic activities and activation of signaling molecules involved in homeostasis of cytosolic stress level, such as energy metabolism, signal transduction, carbohydrate metabolism, and interfered with flagellar assembly proteins and two component systems involved in external sensing. The aforementioned metabolic pathways have a direct impact on antioxidant pathways such as the glutathione-fueled energy rescue system for removing ROS. In line with these results, the *zwfA*, *icd*, *idh*, and PP5211 genes were enriched together with all *atp* genes for ATP production.

Both nFe_3O_4 and nZVI temporarily decreased the cell viability of *R. subcapitata* and the shadow effect of these NPs lowered the non-photochemical quenching of cells. Exposure to nZVI, but not to nFe_3O_4, caused a more pronounced gene expression profile with highly upregulated pathways such as DNA repair which could then be linked to upregulation of carbohydrate-energy metabolism. The repair pathways that were triggered within 1 h probably function as a sentinel protective response in *R. subcapitata*, which then enable the quick adaptive response of *R. subcapitata*.

Overall, this study provides important insights into the multi-level gene expression regulation in *P. putida* and *R. subcapitata* when exposed to nZVI, nFe_3O_4, and dissolved forms of iron released from nZVI. RNA-seq revealed the hidden patterns of cellular response that was orchestrated within sophisticated regulatory circuit based on the gene regulatory signaling and external stimuli. The defense system was very effectively activated right after the exposure, to environmentally relevant concentrations of NPs leading to mitigation of oxidative stress.

6. References

Abdal Dayem, A., Hossain, M.K., Lee, S. bin, Kim, K., Saha, S.K., Yang, G.-M., Choi, H.Y., Cho, S.-G., 2017. The Role of Reactive Oxygen Species (ROS) in the Biological Activities of Metallic Nanoparticles. Int J Mol Sci 18, 120. https://doi.org/10.3390/ijms18010120

Allorent, G., Tokutsu, R., Roach, T., Peers, G., Cardol, P., Girard-Bascou, J., Seigneurin-Berny, D., Petroutsos, D., Kuntz, M., Breyton, C., Franck, F., Wollman, F.-A., Niyogi, K.K., Krieger-Liszkay, A., Minagawa, J., Finazzi, G., 2013. A Dual Strategy to Cope with High Light in Chlamydomonas reinhardtii Plant Cell 25, 545–557. https://doi.org/10.1105/tpc.112.108274

Arnér, E.S.J., Holmgren, A., 2000. Physiological functions of thioredoxin and thioredoxin reductase. Eur J Biochem 267, 6102–6109.

Auffan, M., Achouak, W., Rose, J., Roncato, M.-A., Chanéac, C., T. Waite, D., Masion, A., C. Woicik, J., R. Wiesner, M., Bottero, J.-Y., 2008. Relation between the Redox State of Iron-Based Nanoparticles and Their Cytotoxicity toward Escherichia coli. Environmental Science & Technology 42, 6730–6735. https://doi.org/10.1021/es800086f

Bae, S., Collins, R.N., Waite, T.D., Hanna, K., 2018. Advances in Surface Passivation of Nanoscale Zerovalent Iron: A Critical Review. Environ Sci Technol 52, 12010–12025. https://doi.org/10.1021/acs.est.8b01734

Bateman, A., Martin, M.-J., Orchard, S., Magrane, M., Ahmad, S., Alpi, E., Bowler-Barnett, E.H., Britto, R., Bye-A-Jee, H., Cukura, A., 2022. UniProt: the Universal Protein Knowledgebase in 2023. Nucleic Acids Res.

Benjamini, Y., Hochberg, Y., 1995. Controlling the False Discovery Rate: A Practical and Powerful Approach to Multiple Testing. Journal of the Royal Statistical Society. Series B (Methodological) 57, 289–300.

Bethke, C.M., 2007. Geochemical and biogeochemical reaction modeling. Cambridge University Press.

Bethke, C.M., Farrell, B., Sharifi, M., 2021. The Geochemist's Workbench® Release 15 (five volumes).

Blifernez-Klassen, O., Berger, H., Mittmann, B.G.K., Klassen, V., Schelletter, L., Buchholz, T., Baier, T., Soleimani, M., Wobbe, L., Kruse, O., 2021. A gene regulatory network for antenna size control in carbon dioxide-deprived Chlamydomonas reinhardtii cells. Plant Cell 33, 1303–1318. https://doi.org/10.1093/plcell/koab012

Bolger, A.M., Lohse, M., Usadel, B., 2014. Trimmomatic: a flexible trimmer for Illumina sequence data. Bioinformatics 30, 2114–2120. https://doi.org/10.1093/bioinformatics/btu170

Burczyk, J., Dworzanski, J., 1988. Comparison of sporopollenin-like algal resistant polymer from cell wall of Botryococcus, scenedesmus and lycopodium clavatum by GC-pyrolysis. Phytochemistry 27, 2151–2153. https://doi.org/10.1016/0031-9422(88)80115-8

Cánovas, D., Cases, I., de Lorenzo, V., 2003. Heavy metal tolerance and metal homeostasis in Pseudomonas putida as revealed by complete genome analysis. Environ Microbiol 5, 1242–1256. https://doi.org/10.1111/j.1462-2920.2003.00463.x

Chaithawiwat, K., Vangnai, A., McEvoy, J.M., Pruess, B., Krajangpan, S., Khan, E., 2016. Impact of nanoscale zero valent iron on bacteria is growth phase dependent. Chemosphere 144, 352–359. https://doi.org/https://doi.org/10.1016/j.chemosphere.2015.09.025

Chatterjee, N., Walker, G.C., 2017. Mechanisms of DNA damage, repair, and mutagenesis. Environ Mol Mutagen 58, 235–263. https://doi.org/https://doi.org/10.1002/em.22087

Chavarría, M., Nikel, P.I., Pérez-Pantoja, D., de Lorenzo, V., 2013. The Entner-Doudoroff pathway empowers Pseudomonas putidaKT2440 with a high tolerance to oxidative stress. Environ Microbiol 15, 1772–1785. https://doi.org/10.1111/1462-2920.12069

Chen, F., Wang, C., Yue, L., Zhu, L., Tang, J., Yu, X., Cao, X., Schröder, P., Wang, Z., 2021. Cell Walls Are Remodeled to Alleviate nY2O3 Cytotoxicity by Elaborate Regulation of de Novo Synthesis and Vesicular Transport. ACS Nano 15, 13166–13177. https://doi.org/10.1021/acsnano.1c02715

Chen, H., Boutros, P.C., 2011. VennDiagram: a package for the generation of highly-customizable Venn and Euler diagrams in R. BMC Bioinformatics 12, 35. https://doi.org/10.1186/1471-2105-12-35

Chen, P.-J., Tan, S.-W., Wu, W.-L., 2012. Stabilization or Oxidation of Nanoscale Zerovalent Iron at Environmentally Relevant Exposure Changes Bioavailability and Toxicity in Medaka Fish. Environmental Science & Technology 46, 8431–8439. https://doi.org/10.1021/es3006783

Chen, Z., Gao, S., Jin, M., Sun, S., Lu, J., Yang, P., Bond, P.L., Yuan, Z., Guo, J., 2019. Physiological and transcriptomic analyses reveal CuO nanoparticle inhibition of anabolic and catabolic activities of sulfate-reducing bacterium. Environ Int 125, 65–74. https://doi.org/https://doi.org/10.1016/j.envint.2019.01.058

Chomczynski, P., Sacchi, N., 2006. The single-step method of RNA isolation by acid guanidinium thiocyanate–phenol–chloroform extraction: twenty-something years on. Nat Protoc 1, 581–585. https://doi.org/10.1038/nprot.2006.83

Christodoulou, D., Link, H., Fuhrer, T., Kochanowski, K., Gerosa, L., Sauer, U., 2018. Reserve Flux Capacity in the Pentose Phosphate Pathway Enables Escherichia coli's Rapid Response to Oxidative Stress. Cell Syst 6, 569-578.e7. https://doi.org/10.1016/j.cels.2018.04.009

Crabbé, A., Leroy, B., Wattiez, R., Aertsen, A., Leys, N., Cornelis, P., van Houdt, R., 2012. Differential proteomics and physiology of Pseudomonas putida KT2440 under filament-inducing conditions. BMC Microbiol 12. https://doi.org/10.1186/1471-2180-12-282

Crampon, M., Joulian, C., Ollivier, P., Charron, M., Hellal, J., 2019. Shift in natural groundwater bacterial community structure due to zero-valent iron nanoparticles (nZVI). Front Microbiol 10, 1–14. https://doi.org/10.3389/fmicb.2019.00533

Crane, R.A., Dickinson, M., Popescu, I.C., Scott, T.B., 2011. Magnetite and zero-valent iron nanoparticles for the remediation of uranium contaminated environmental water. Water Res 45, 2931–2942. https://doi.org/10.1016/J.WATRES.2011.03.012

Cucchi, D., Gibson, A., Martin, S. a, 2021. The emerging relationship between metabolism and DNA repair. Cell Cycle 20, 943–959. https://doi.org/10.1080/15384101.2021.1912889

Czinnerová, M., Vološčuková, O., Marková, K., Ševců, A., Černík, M., Nosek, J., 2020. Combining nanoscale zero-valent iron with electrokinetic treatment for remediation of chlorinated ethenes and promoting biodegradation: A long-term field study. Water Res 175, 115692. https://doi.org/https://doi.org/10.1016/j.watres.2020.115692

Danecek, P., Bonfield, J.K., Liddle, J., Marshall, J., Ohan, V., Pollard, M.O., Whitwham, A., Keane, T., McCarthy, S.A., Davies, R.M., Li, H., 2021. Twelve years of SAMtools and BCFtools. Gigascience 10, giab008. https://doi.org/10.1093/gigascience/giab008

David, S.S., O'Shea, V.L., Kundu, S., 2007. Base-excision repair of oxidative DNA damage. Nature 447, 941–950. https://doi.org/10.1038/nature05978

Diao, M., Yao, M., 2009. Use of zero-valent iron nanoparticles in inactivating microbes. Water Res 43, 5243–5251. https://doi.org/10.1016/j.watres.2009.08.051

Dobin, A., Davis, C.A., Schlesinger, F., Drenkow, J., Zaleski, C., Jha, S., Batut, P., Chaisson, M., Gingeras, T.R., 2013. STAR: Ultrafast universal RNA-seq aligner. Bioinformatics 29, 15–21. https://doi.org/10.1093/bioinformatics/bts635

Doncheva, N.T., Morris, J.H., Holze, H., Kirsch, R., Nastou, K.C., Cuesta-Astroz, Y., Rattei, T., Szklarczyk, D., von Mering, C., Jensen, L.J., 2022. Cytoscape string App 2.0: Analysis and Visualization of Heterogeneous Biological Networks. J Proteome Res. https://doi.org/10.1021/acs.jproteome.2c00651

El-Temsah, Y.S., Sevcu, A., Bobcikova, K., Cernik, M., Joner, E.J., 2016. DDT degradation efficiency and ecotoxicological effects of two types of nano-sized zero-valent iron (nZVI) in water and soil. Chemosphere 144, 2221–2228. https://doi.org/10.1016/j.chemosphere.2015.10.122

Fajardo, C., Ortíz, L.T., Rodríguez-Membibre, M.L., Nande, M., Lobo, M.C., Martin, M., 2012. Assessing the impact of zero-valent iron (ZVI) nanotechnology on soil microbial structure and functionality: A molecular approach. Chemosphere 86, 802–808. https://doi.org/10.1016/j.chemosphere.2011.11.041

Fajardo, Saccà, M.L., Martinez-Gomariz, M., Costa, G., Nande, M., Martin, M., 2013. Transcriptional and proteomic stress responses of a soil bacterium Bacillus cereus to nanosized zero-valent iron (nZVI) particles. Chemosphere 93, 1077–1083. https://doi.org/https://doi.org/10.1016/j.chemosphere.2013.05.082

Fernández-Piñar, R., Ramos, J.L., Rodríguez-Herva, J.J., Espinosa-Urgel, M., 2008. A Two-Component Regulatory System Integrates Redox State and Population Density Sensing in Pseudomonas putida; J Bacteriol 190, 7666 LP – 7674. https://doi.org/10.1128/JB.00868-08

Ge, S.X., Son, E.W., Yao, R., 2018. iDEP: an integrated web application for differential expression and pathway analysis of RNA-Seq data. BMC Bioinformatics 19, 534. https://doi.org/10.1186/s12859-018-2486-6

Gonzalo, S., Llaneza, V., Pulido-Reyes, G., Fernández-Piñas, F., Bonzongo, J.C., Leganes, F., Rosal, R., García-Calvo, E., Rodea-Palomares, I., 2014. A Colloidal Singularity Reveals the Crucial Role of Colloidal Stability for Nanomaterials In-Vitro Toxicity Testing: nZVI-Microalgae Colloidal System as a Case Study. PLoS One 9, e109645. https://doi.org/10.1371/journal.pone.0109645

Grigoriev, I. v, Hayes, R.D., Calhoun, S., Kamel, B., Wang, A., Ahrendt, S., Dusheyko, S., Nikitin, R., Mondo, S.J., Salamov, A., Shabalov, I., Kuo, A., 2021. PhycoCosm, a comparative algal genomics resource. Nucleic Acids Res 49, D1004–D1011. https://doi.org/10.1093/nar/gkaa898

Guo, Z., Luo, Y., Zhang, P., Chetwynd, A.J., Qunhui Xie, H., Abdolahpur Monikh, F., Tao, W., Xie, C., Liu, Y., Xu, L., Zhang, Z., Valsami-Jones, E., Lynch, I., Zhao, B., 2020. Deciphering the particle specific effects on metabolism in rat liver and plasma from ZnO nanoparticles versus ionic Zn exposure. Environ Int 136, 105437. https://doi.org/https://doi.org/10.1016/j.envint.2019.105437

Hannemann, F., Bichet, A., Ewen, K.M., Bernhardt, R., 2007. Cytochrome P450 systems—biological variations of electron transport chains. Biochimica et Biophysica Acta (BBA) - General Subjects 1770, 330–344. https://doi.org/https://doi.org/10.1016/j.bbagen.2006.07.017

Harris, E.H., Stern, D., Witman, G., 2009. The Chlamydomonas Sourcebook: Second Edition, Second Edition. ed. Academic press.

Hund-Rinke, K., Schlinkert, R., Schlich, K., 2022. Testing particles using the algal growth inhibition test (OECD 201): the suitability of in vivo chlorophyll fluorescence measurements. Environ Sci Eur 34, 41. https://doi.org/10.1186/s12302-022-00623-1

Hurtado-Gallego, J., Pulido-Reyes, G., González-Pleiter, M., Salas, G., Leganés, F., Rosal, R., Fernández-Piñas, F., 2020. Toxicity of superparamagnetic iron oxide nanoparticles to the microalga Chlamydomonas reinhardtii. Chemosphere 238, 124562. https://doi.org/https://doi.org/10.1016/j.chemosphere.2019.124562

J. Miller, R., S. Lenihan, H., B. Muller, E., Tseng, N., K. Hanna, S., A. Keller, A., 2010. Impacts of Metal Oxide Nanoparticles on Marine Phytoplankton. Environmental Science & Technology 44, 7329–7334. https://doi.org/10.1021/es100247x

J. Niemuth, N., J. Curtis, B., D. Laudadio, E., Sostare, E., A. Bennett, E., J. Neureuther, N., A. Mohaimani, A., Schmoldt, A., D. Ostovich, E., R. Viant, M., J. Hamers, R., D. Klaper, R., 2021. Energy Starvation in Daphnia magna from Exposure to a Lithium Cobalt Oxide Nanomaterial. Chem Res Toxicol 34, 2287–2297. https://doi.org/10.1021/acs.chemrestox.1c00189

James, E.L., Michalek, R.D., Pitiyage, G.N., de Castro, A.M., Vignola, K.S., Jones, J., Mohney, R.P., Karoly, E.D., Prime, S.S., Parkinson, E.K., 2015. Senescent human fibroblasts show increased glycolysis and redox homeostasis with extracellular metabolomes that overlap with those of irreparable DNA damage, aging, and disease. J Proteome Res 14, 1854–1871.

Jena, P., Bhattacharya, M., Bhattacharjee, G., Satpati, B., Mukherjee, P., Senapati, D., Srinivasan, R., 2020. Bimetallic gold–silver nanoparticles mediate bacterial killing by disrupting the actin cytoskeleton MreB. Nanoscale 12, 3731–3749. https://doi.org/10.1039/C9NR10700B

Jiang, P., Du, W., Wang, X., Mancuso, A., Gao, X., Wu, M., Yang, X., 2011. p53 regulates biosynthesis through direct inactivation of glucose-6-phosphate dehydrogenase. Nat Cell Biol 13, 310–316. https://doi.org/10.1038/ncb2172

Jin, C., Liu, Y., Sun, L., Chen, T., Zhang, Y., Zhao, A., Wang, X., Cristau, M., Wang, K., Jia, W., 2013. Metabolic profiling reveals disorder of carbohydrate metabolism in mouse fibroblast cells induced by titanium dioxide nanoparticles. Journal of Applied Toxicology 33, 1442–1450. https://doi.org/https://doi.org/10.1002/jat.2808

Joshi, A.S., Singh, P., Mijakovic, I., 2020. Interactions of Gold and Silver Nanoparticles with Bacterial Biofilms: Molecular Interactions behind Inhibition and Resistance. Int J Mol Sci 21, 7658. https://doi.org/10.3390/ijms21207658

Joshi, G.R., Cooper, K., Zhong, X., Cook, A.B., Ahmad, E.A., Harrison, N.M., Engelberg, D.L., Lindsay, R., 2018. Temporal evolution of sweet oilfield corrosion scale: Phases, morphologies, habits, and protection. Corros Sci 142, 110–118. https://doi.org/https://doi.org/10.1016/j.corsci.2018.07.009

Kanehisa, M., Goto, S., 2000. KEGG: kyoto encyclopedia of genes and genomes. Nucleic Acids Res 28, 27–30. https://doi.org/10.1093/nar/28.1.27

Karp, P.D., Billington, R., Caspi, R., Fulcher, C.A., Latendresse, M., Kothari, A., Keseler, I.M., Krummenacker, M., Midford, P.E., Ong, Q., Ong, W.K., Paley, S.M., Subhraveti, P., 2019. The BioCyc collection of microbial genomes and metabolic pathways. Brief Bioinform 20, 1085—1093. https://doi.org/10.1093/bib/bbx085

Keller, A.A., Garner, K., Miller, R.J., Lenihan, H.S., 2012. Toxicity of Nano-Zero Valent Iron to Freshwater and Marine Organisms. PLoS One 7, e43983-.

Kim, D., Paggi, J.M., Park, C., Bennett, C., Salzberg, S.L., 2019. Graph-based genome alignment and genotyping with HISAT2 and HISAT-genotype. Nat Biotechnol 37, 907–915. https://doi.org/10.1038/s41587-019-0201-4

Kitabatake, K., Kaji, T., Tsukimoto, M., 2020. ATP and ADP enhance DNA damage repair in γ-irradiated BEAS-2B human bronchial epithelial cells through activation of P2X7 and P2Y12 receptors. Toxicol Appl Pharmacol 407, 115240. https://doi.org/https://doi.org/10.1016/j.taap.2020.115240

Kittler, S., Greulich, C., Diendorf, J., Köller, M., Epple, M., 2010. Toxicity of Silver Nanoparticles Increases during Storage Because of Slow Dissolution under Release of Silver Ions. Chemistry of Materials 22, 4548–4554. https://doi.org/10.1021/cm100023p

Kotchaplai, P., Khan, E., S. Vangnai, A., 2017. Membrane Alterations in Pseudomonas putida F1 Exposed to Nanoscale Zerovalent Iron: Effects of Short-Term and Repetitive nZVI Exposure. Environmental Science & Technology 51, 7804–7813. https://doi.org/10.1021/acs.est.7b00736

Kumar, N., Auffan, M., Gattacceca, J., Rose, J., Olivi, L., Borschneck, D., Kvapil, P., Jublot, M., Kaifas, D., Malleret, L., Doumenq, P., Bottero, J.-Y., 2014. Molecular Insights of Oxidation Process of Iron Nanoparticles: Spectroscopic, Magnetic, and Microscopic Evidence. Environmental Science & Technology 48, 13888–13894. https://doi.org/10.1021/es503154q

L. Kirschling, T., B. Gregory, K., G. Minkley, Jr., E., v. Lowry, G., D. Tilton, R., 2010. Impact of Nanoscale Zero Valent Iron on Geochemistry and Microbial Populations in

Trichloroethylene Contaminated Aquifer Materials. Environmental Science & Technology 44, 3474–3480. https://doi.org/10.1021/es903744f

Lawrence, M., Huber, W., Pagès, H., Aboyoun, P., Carlson, M., Gentleman, R., Morgan, M.T., Carey, V.J., 2013. Software for Computing and Annotating Genomic Ranges. PLoS Comput Biol 9, e1003118-.

Lee, C., Jee, Y.K., Won, I.L., Nelson, K.L., Yoon, J., Sedlak, D.L., 2008. Bactericidal effect of zero-valent iron nanoparticles on Escherichia coli. Environ Sci Technol 42, 4927–4933. https://doi.org/10.1021/es800408u

Lefevre, E., Bossa, N., Wiesner, M.R., Gunsch, C.K., 2015. A review of the environmental implications of in situ remediation by nanoscale zero valent iron (nZVI): Behavior, transport and impacts on microbial communities. Science of the Total Environment 565, 889–901. https://doi.org/10.1016/j.scitotenv.2016.02.003

Lei, C., Zhang, L., Yang, K., Zhu, L., Lin, D., 2016. Toxicity of iron-based nanoparticles to green algae: Effects of particle size, crystal phase, oxidation state and environmental aging. Environmental Pollution 218, 505–512. https://doi.org/https://doi.org/10.1016/j.envpol.2016.07.030

Li, H., Durbin, R., 2009. Fast and accurate short read alignment with Burrows–Wheeler transform. Bioinformatics 25, 1754–1760. https://doi.org/10.1093/bioinformatics/btp324

Li, S., Wang, W., Liang, F., Zhang, W.X., 2017. Heavy metal removal using nanoscale zero-valent iron (nZVI): Theory and application. J Hazard Mater 322, 163–171. https://doi.org/10.1016/J.JHAZMAT.2016.01.032

Liang, L., Li, X., Guo, Y., Lin, Z., Su, X., Liu, B., 2021. The removal of heavy metal cations by sulfidated nanoscale zero-valent iron (S-nZVI): The reaction mechanisms and the role of sulfur. J Hazard Mater 404, 124057. https://doi.org/10.1016/J.JHAZMAT.2020.124057

Liang, W., Dai, C., Zhou, X., Zhang, Y., 2014. Application of zero-valent iron nanoparticles for the removal of aqueous zinc ions under various experimental conditions. PLoS One 9. https://doi.org/10.1371/journal.pone.0085686

Lichtenthaler, H.K., 1987. [34] Chlorophylls and carotenoids: Pigments of photosynthetic biomembranes. Methods Enzymol 148, 350–382. https://doi.org/https://doi.org/10.1016/0076-6879(87)48036-1

Lim, S.-L., Voon, C.P., Guan, X., Yang, Y., Gardeström, P., Lim, B.L., 2020. In planta study of photosynthesis and photorespiration using NADPH and NADH/NAD+ fluorescent protein sensors. Nat Commun 11, 3238. https://doi.org/10.1038/s41467-020-17056-0

Liu, A., Liu, J., Han, J., Zhang, W., 2017. Evolution of nanoscale zero-valent iron (nZVI) in water: Microscopic and spectroscopic evidence on the formation of nano- and micro-structured iron oxides. J Hazard Mater 322, 129–135. https://doi.org/https://doi.org/10.1016/j.jhazmat.2015.12.070

Liu, P., Chen, X., Huang, Q., Chen, W., 2015. The Role of CzcRS Two-Component Systems in the Heavy Metal Resistance of Pseudomonas putida X4. Int J Mol Sci 16, 17005–17017. https://doi.org/10.3390/ijms160817005

Livak, K.J., Schmittgen, T.D., 2001. Analysis of relative gene expression data using real-time quantitative PCR and the 2(-Delta Delta C(T)) Method. Methods 25, 402–408. https://doi.org/10.1006/meth.2001.1262

Llaneza, V., Rodea-Palomares, I., Zhou, Z., Rosal, R., Fernández-Pina, F., Bonzongo, J.-C.J., 2016. Polyvinylpyrrolidone and arsenic-induced changes in biological responses of model aquatic organisms exposed to iron-based nanoparticles. Journal of Nanoparticle Research 18, 235. https://doi.org/10.1007/s11051-016-3541-8

Long, Q., Liu, F., Yuan, Y., Dai, Y., Wang, C., Li, X., Zhang, J., 2020. Enhanced degradation performance of p-chlorophenol in photo-Fenton reaction activated by nano-Fe0 encapsulated in hydrothermal carbon: Improved Fe(III)/Fe(II) cycle. Colloids Surf A Physicochem Eng Asp 594, 124650. https://doi.org/10.1016/j.colsurfa.2020.124650

Love, M.I., Huber, W., Anders, S., 2014. Moderated estimation of fold change and dispersion for RNA-seq data with DESeq2. Genome Biol 15, 550. https://doi.org/10.1186/s13059-014-0550-8

Lucker, B., Kramer, D.M., 2013. Regulation of cyclic electron flow in Chlamydomonas reinhardtii under fluctuating carbon availability. Photosynth Res 117, 449–459.

Lv, Y., Niu, Z., Chen, Y., Hu, Y., 2017. Bacterial effects and interfacial inactivation mechanism of nZVI/Pd on Pseudomonas putida strain. Water Res 115, 297–308. https://doi.org/https://doi.org/10.1016/j.watres.2017.03.012

Ma, J., Lü, X., Huang, Y., 2011. Genomic analysis of cytotoxicity response to nanosilver in human dermal fibroblasts. J Biomed Nanotechnol 7, 263–275. https://doi.org/10.1166/jbn.2011.1286

MacLean, A., Bley, A.M., Appanna, V.P., Appanna, V.D., 2020. Metabolic manipulation by Pseudomonas fluorescens: A powerful stratagem against oxidative and metal stress. J Med Microbiol. https://doi.org/10.1099/JMM.0.001139

Magdanova, L.A., Goliasnaia, N. v, 2013. [Heterogeneity as an adaptive trait of the bacterial community]. Mikrobiologiia 82, 3–13. https://doi.org/10.7868/s0026365613010072

Marsalek, B., Jancula, D., Marsalkova, E., Mashlan, M., Safarova, K., Tucek, J., Zboril, R., 2012. Multimodal Action and Selective Toxicity of Zerovalent Iron Nanoparticles against Cyanobacteria. Environmental Science & Technology 46, 2316–2323. https://doi.org/10.1021/es2031483

Maxwell, K., Johnson, G.N., 2000. Chlorophyll fluorescence—a practical guide. J Exp Bot 51, 659–668. https://doi.org/10.1093/jexbot/51.345.659

McCarter, L.L., 2006. Regulation of flagella. Curr Opin Microbiol. https://doi.org/10.1016/j.mib.2006.02.001

Meister, A., 1988. Glutathione metabolism and its selective modification. Journal of Biological Chemistry. https://doi.org/10.1016/S0021-9258(19)77815-6

Metsalu, T., Vilo, J., 2015. ClustVis: a web tool for visualizing clustering of multivariate data using Principal Component Analysis and heatmap. Nucleic Acids Res 43, W566–W570. https://doi.org/10.1093/nar/gkv468

Milanese, C., Bombardieri, C.R., Sepe, S., Barnhoorn, S., Payán-Goméz, C., Caruso, D., Audano, M., Pedretti, S., Vermeij, W.P., Brandt, R.M.C., Gyenis, A., Wamelink, M.M., de Wit, A.S., Janssens, R.C., Leen, R., van Kuilenburg, A.B.P., Mitro, N., Hoeijmakers, J.H.J., Mastroberardino, P.G., 2019. DNA damage and transcription stress cause ATP-mediated redesign of metabolism and potentiation of anti-oxidant buffering. Nat Commun 10, 4887. https://doi.org/10.1038/s41467-019-12640-5

Moore, J.D., Avellan, A., Noack, C.W., Guo, Y., Lowry, G. v, Gregory, K.B., 2017. Time-dependent bacterial transcriptional response to CuO nanoparticles differs from that of Cu2+ and provides insights into CuO nanoparticle toxicity mechanisms. Environ Sci Nano 4, 2321–2335. https://doi.org/10.1039/C7EN00600D

Morgan, M., Pagès, H., Obenchain, V., Hayden, N., 2022. Binary alignment (BAM), FASTA, variant call (BCF), and tabix file import. https://doi.org/10.18129/B9.bioc.Rsamtools

Mueller, N.C., Braun, J., Bruns, J., Černík, M., Rissing, P., Rickerby, D., Nowack, B., 2012. Application of nanoscale zero valent iron (NZVI) for groundwater remediation in Europe. Environmental Science and Pollution Research 19, 550–558. https://doi.org/10.1007/s11356-011-0576-3

Mulakhudair, A.R., Al-Mashhadani, M., Hanotu, J., Zimmerman, W., 2017. Inactivation combined with cell lysis of Pseudomonas putida using a low pressure carbon dioxide microbubble technology. Journal of Chemical Technology and Biotechnology 92, 1961–1969. https://doi.org/10.1002/jctb.5299

Müller, P., Li, X.-P., Niyogi, K.K., 2001. Non-Photochemical Quenching. A Response to Excess Light Energy1. Plant Physiol 125, 1558–1566. https://doi.org/10.1104/pp.125.4.1558

Murchie, E.H., Lawson, T., 2013. Chlorophyll fluorescence analysis: a guide to good practice and understanding some new applications. J Exp Bot 64, 3983–3998. https://doi.org/10.1093/jxb/ert208

Nano Iron, n.d. Manual for preparation of an aqueous suspension from dry stabilized iron powder NANOFER STAR [WWW Document]. https://doi.org/https://nanoiron.cz/getattachment/7aa3e8c5-5701-4a47-b05c-b91f87279aae/NANOFER-STAR-processing-activation-manual.aspx

Nel, A., Xia, T., Mädler, L., Li, N., 2006. Toxic potential of materials at the nanolevel. Science 311, 622–627. https://doi.org/10.1126/science.1114397

Němeček, J., Pokorný, P., Lacinová, L., Černík, M., Masopustová, Z., Lhotský, O., Filipová, A., Cajthaml, T., 2015. Combined abiotic and biotic in-situ reduction of hexavalent chromium in groundwater using nZVI and whey: A remedial pilot test. J Hazard Mater 300, 670–679. https://doi.org/https://doi.org/10.1016/j.jhazmat.2015.07.056

Nguyen, N.H.A., Špánek, R., Falagan-Lotsch, P., Ševců, A., 2021. Impact of Zero-Valent Iron on Freshwater Bacterioplankton Metabolism as Predicted from 16S rRNA Gene Sequence Libraries. Curr Microbiol 78, 979–991. https://doi.org/10.1007/s00284-021-02362-7

Nguyen, N.H.A., Špánek, R., Kasalický, V., Ribas, D., Vlková, D., Řeháková, H., Kejzlar, P., Ševců, A., 2018a. Different effects of nano-scale and micro-scale zero-valent iron

particles on planktonic microorganisms from natural reservoir water. Environ Sci Nano 5, 1117–1129. https://doi.org/10.1039/c7en01120b

Nguyen, N.H.A., Von Moos, N.R., Slaveykova, V.I., Mackenzie, K., Meckenstock, R.U., Thűmmler, S., Bosch, J., Ševců, A., 2018b. Biological effects of four iron-containing nanoremediation materials on the green alga Chlamydomonas sp. Ecotoxicol Environ Saf 154, 36–44. https://doi.org/https://doi.org/10.1016/j.ecoenv.2018.02.027

Nikel, P.I., Fuhrer, T., Chavarría, M., Sánchez-Pascuala, A., Sauer, U., de Lorenzo, V., 2021. Reconfiguration of metabolic fluxes in Pseudomonas putida as a response to sub-lethal oxidative stress. ISME J. https://doi.org/10.1038/s41396-020-00884-9

Nordberg, H., Cantor, M., Dusheyko, S., Hua, S., Poliakov, A., Shabalov, I., Smirnova, T., Grigoriev, I. v, Dubchak, I., 2014. The genome portal of the Department of Energy Joint Genome Institute: 2014 updates. Nucleic Acids Res 42, D26–D31. https://doi.org/10.1093/nar/gkt1069

Ortega-Calvo, J.-J., Jimenez-Sanchez, C., Pratarolo, P., Pullin, H., Scott, T.B., Thompson, I.P., 2016. Tactic response of bacteria to zero-valent iron nanoparticles. Environmental Pollution 213, 438–445. https://doi.org/https://doi.org/10.1016/j.envpol.2016.01.093

Pagnout, C., Jomini, S., Dadhwal, M., Caillet, C., Thomas, F., Bauda, P., 2012. Role of electrostatic interactions in the toxicity of titanium dioxide nanoparticles toward Escherichia coli. Colloids Surf B Biointerfaces 92, 315–321. https://doi.org/10.1016/j.colsurfb.2011.12.012

Parkhurst, D.L., Appelo, C.A.J., 2013. Description of Input and Examples for PHREEQC Version 3 — A Computer Program for Speciation, Batch-Reaction, One-Dimensional Transport, and Inverse Geochemical Calculations. U.S. Geological Survey Techniques and Methods, book 6, chapter A43.

Peter Guengerich, F., 2001. Common and Uncommon Cytochrome P450 Reactions Related to Metabolism and Chemical Toxicity. Chem Res Toxicol 14, 611–650. https://doi.org/10.1021/tx0002583

Piersanti, A., Juganson, K., Mozzicafreddo, M., Wei, W., Zhang, J., Zhao, K., Ballarini, P., Mortimer, M., Pucciarelli, S., Miao, W., Miceli, C., 2021. Transcriptomic responses to silver nanoparticles in the freshwater unicellular eukaryote Tetrahymena thermophila. Environmental Pollution 269, 115965. https://doi.org/https://doi.org/10.1016/j.envpol.2020.115965

Planchon, M., Leger, T., Spalla, O., Huber, G., Ferrari, R., 2017. Metabolomic and proteomic investigations of impacts of titanium dioxide nanoparticles on Escherichia coli. PLoS One 12, e0178437. https://doi.org/10.1371/journal.pone.0178437

Polle, A., 2001. Dissecting the superoxide dismutase-ascorbate-glutathione-pathway in chloroplasts by metabolic modeling. Computer simulations as a step towards flux analysis. Plant Physiol 126, 445–462. https://doi.org/10.1104/pp.126.1.445

Quinlan, A.R., Hall, I.M., 2010. BEDTools: a flexible suite of utilities for comparing genomic features. Bioinformatics 26, 841–842. https://doi.org/10.1093/bioinformatics/btq033

R. Keenan, C., L. Sedlak, D., 2008. Factors Affecting the Yield of Oxidants from the Reaction of Nanoparticulate Zero-Valent Iron and Oxygen. Environmental Science & Technology 42, 1262–1267. https://doi.org/10.1021/es7025664

Reis Falcão, V., Pedroso Tonon, A., Cabral Oliveira, M., Colepicolo, P., 2008. RNA isolation method for polysaccharide rich algae: Agar producing Gracilaria tenuistipitata (Rhodophyta). J Appl Phycol 20, 9–12. https://doi.org/10.1007/s10811-007-9174-7

Rivera-Araya, J., Pollender, A., Huynh, D., Schlömann, M., Chávez, R., Levicán, G., 2019. Osmotic Imbalance, Cytoplasm Acidification and Oxidative Stress Induction Support the High Toxicity of Chloride in Acidophilic Bacteria Frontiers in Microbiology.

Rutkowski, R., Pancewicz, S.A., Rutkowski, K., Rutkowska, J., 2007. [Reactive oxygen and nitrogen species in inflammatory process]. Pol Merkur Lekarski 23, 131–136.

Saccà, M.L., Fajardo, C., Martinez-Gomariz, M., Costa, G., Nande, M., Martin, M., 2014. Molecular Stress Responses to Nano-Sized Zero-Valent Iron (nZVI) Particles in the Soil Bacterium Pseudomonas stutzeri. PLoS One 9, e89677. https://doi.org/10.1371/journal.pone.0089677

Schärer, O.D., 2013. Nucleotide excision repair in eukaryotes. Cold Spring Harb Perspect Biol 5, a012609.

Schmid, D., Micić, V., Laumann, S., Hofmann, T., 2014. Measuring the reactivity of commercially available zero-valent iron nanoparticles used for environmental remediation with iopromide. J Contam Hydrol 181, 36–45. https://doi.org/10.1016/j.jconhyd.2015.01.006

Schröter, L., Dersch, P., 2019. Phenotypic Diversification of Microbial Pathogens—Cooperating and Preparing for the Future. J Mol Biol. https://doi.org/10.1016/j.jmb.2019.06.024

Semerád, J., Filip, J., Ševců, A., Brumovský, M., Nguyen, N.H.A., Mikšíček, J., Lederer, T., Filipová, A., Boháčková, J., Cajthaml, T., 2020. Environmental fate of sulfidated nZVI particles: the interplay of nanoparticle corrosion and toxicity during aging. Environ Sci Nano 7, 1794–1806. https://doi.org/10.1039/D0EN00075B

Semerád, J., Moeder, M., Filip, J., Pivokonský, M., Filipová, A., Cajthaml, T., 2019. Oxidative stress in microbes after exposure to iron nanoparticles: analysis of aldehydes as oxidative damage products of lipids and proteins. Environ Sci Pollut Res Int 26, 33670–33682. https://doi.org/10.1007/s11356-019-06370-w

Semerád, J., Ševců, A., Nguyen, N.H.A., Hrabák, P., Špánek, R., Bobčíková, K., Pospíšková, K., Filip, J., Medřík, I., Kašlík, J., Šafařík, I., Filipová, A., Nosek, J., Pivokonský, M., Cajthaml, T., 2021. Discovering the potential of an nZVI-biochar composite as a material for the nanobioremediation of chlorinated solvents in groundwater: Degradation efficiency and effect on resident microorganisms. Chemosphere 281, 130915. https://doi.org/https://doi.org/10.1016/j.chemosphere.2021.130915

Ševců, A., El-Temsah, Y.S., Joner, E.J., Černík, M., 2011. Oxidative stress induced in microorganisms by zero-valent iron nanoparticles. Microbes Environ 26, 271–281. https://doi.org/10.1264/jsme2.me11126

Shameer, S., Ratcliffe, R.G., Sweetlove, L.J., 2019. Leaf Energy Balance Requires Mitochondrial Respiration and Export of Chloroplast NADPH in the Light. Plant Physiol 180, 1947–1961. https://doi.org/10.1104/pp.19.00624

Shanbhogue, S.S., Bezbaruah, A., Simsek, S., Khan, E., 2017. Trichloroethene removal by separately encapsulated and co-encapsulated bacterial degraders and nanoscale zero-

valent iron. Int Biodeterior Biodegradation 125, 269–276. https://doi.org/https://doi.org/10.1016/j.ibiod.2017.08.005

Shannon, P., Markiel, A., Ozier, O., Baliga, N.S., Wang, J.T., Ramage, D., Amin, N., Schwikowski, B., Ideker, T., 2003. Cytoscape: A software Environment for integrated models of biomolecular interaction networks. Genome Res 13, 2498–2504. https://doi.org/10.1101/gr.1239303

Shi, T., van Soest, D.M.K., Polderman, P.E., Burgering, B.M.T., Dansen, T.B., 2021. DNA damage and oxidant stress activate p53 through differential upstream signaling pathways. Free Radic Biol Med 172, 298–311. https://doi.org/https://doi.org/10.1016/j.freeradbiomed.2021.06.013

Simão, F.A., Waterhouse, R.M., Ioannidis, P., Kriventseva, E. v, Zdobnov, E.M., 2015. BUSCO: assessing genome assembly and annotation completeness with single-copy orthologs. Bioinformatics 31, 3210–3212. https://doi.org/10.1093/bioinformatics/btv351

Simon, D.F., Domingos, R.F., Hauser, C., Hutchins, C.M., Zerges, W., Wilkinson, K.J., 2013. Transcriptome sequencing (RNA-seq) analysis of the effects of metal nanoparticle exposure on the transcriptome of Chlamydomonas reinhardtii. Appl Environ Microbiol 79, 4774–4785. https://doi.org/10.1128/AEM.00998-13

Singh, N., Paknikar, K.M., Rajwade, J., 2019. RNA-sequencing reveals a multitude of effects of silver nanoparticles on Pseudomonas aeruginosa biofilms. Environ Sci Nano 6, 1812–1828. https://doi.org/10.1039/c8en01286e

Starkov, A.A., 2008. The role of mitochondria in reactive oxygen species metabolism and signaling. Ann N Y Acad Sci 1147, 37–52. https://doi.org/10.1196/annals.1427.015

Stavropoulou, E., Pircalabioru, G.G., Bezirtzoglou, E., 2018. The Role of Cytochromes P450 in Infection. Front Immunol 9.

Stincone, A., Prigione, A., Cramer, T., Wamelink, M.M.C., Campbell, K., Cheung, E., Olin-Sandoval, V., Grüning, N.M., Krüger, A., Tauqeer Alam, M., Keller, M.A., Breitenbach, M., Brindle, K.M., Rabinowitz, J.D., Ralser, M., 2015. The return of metabolism: Biochemistry and physiology of the pentose phosphate pathway. Biological Reviews 90, 927–963. https://doi.org/10.1111/brv.12140

Sueoka, N., 1960. Mitotic Replication of Deoxyribonucleic acid in Chlamydomonas reinhardi. Proceedings of the National Academy of Sciences 46, 83–91. https://doi.org/10.1073/pnas.46.1.83

Surjana, D., Halliday, G.M., Damian, D.L., 2010. Role of Nicotinamide in DNA Damage, Mutagenesis, and DNA Repair. J Nucleic Acids 2010, 157591. https://doi.org/10.4061/2010/157591

Suzuki, S., Yamaguchi, H., Nakajima, N., Kawachi, M., 2018. Raphidocelis subcapitata (=Pseudokirchneriella subcapitata) provides an insight into genome evolution and environmental adaptations in the Sphaeropleales. Sci Rep 8, 1–13. https://doi.org/10.1038/s41598-018-26331-6

Szklarczyk, D., Gable, A.L., Lyon, D., Junge, A., Wyder, S., Huerta-Cepas, J., Simonovic, M., Doncheva, N.T., Morris, J.H., Jensen, L.J., von Mering, C., 2018. STRING v11: protein-protein association networks with increased coverage, supporting functional discovery in

genome-wide experimental datasets. Nucleic Acids Res 47, 607–613. https://doi.org/10.1093/nar/gky1131

Szklarczyk, D., Gable, A.L., Nastou, K.C., Lyon, D., Kirsch, R., Pyysalo, S., Doncheva, N.T., Legeay, M., Fang, T., Bork, P., Jensen, L.J., von Mering, C., 2021. The STRING database in 2021: customizable protein–protein networks, and functional characterization of user-uploaded gene/measurement sets. Nucleic Acids Res 49, D605. https://doi.org/10.1093/NAR/GKAA1074

Tratnyek, P.G., Johnson, R.L., 2006. Nanotechnologies for environmental cleanup. Nano Today 1, 44–48. https://doi.org/10.1016/S1748-0132(06)70048-2

Volke, D.C., Olavarría, K., Nikel, P.I., 2021. Cofactor Specificity of Glucose-6-Phosphate Dehydrogenase Isozymes in Pseudomonas putida Reveals a General Principle Underlying Glycolytic Strategies in Bacteria mSystems 6. https://doi.org/10.1128/msystems.00014-21

Wang, B., Ye, T., Li, C., Li, X., Chen, L., Wang, G., 2022. Cell damage repair mechanism in a desert green algae Chlorella sp. against UV-B radiation. Ecotoxicol Environ Saf 242, 113916. https://doi.org/https://doi.org/10.1016/j.ecoenv.2022.113916

Wang, S., Zhao, M., Zhou, M., Li, Y.C., Wang, J., Gao, B., Sato, S., Feng, K., Yin, W., Igalavithana, A.D., Oleszczuk, P., Wang, X., Ok, Y.S., 2019. Biochar-supported nZVI (nZVI/BC) for contaminant removal from soil and water: A critical review. J Hazard Mater 373, 820–834. https://doi.org/10.1016/J.JHAZMAT.2019.03.080

Wellburn, A.R., 1994. The spectral determination of chlorophylls a and b, as well as total carotenoids, using various solvents with spectrophotometers of different resolution. J Plant Physiol 144, 307–313.

Wikström, M., Krab, K., Sharma, V., 2018. Oxygen Activation and Energy Conservation by Cytochrome c Oxidase. Chem Rev 118, 2469–2490. https://doi.org/10.1021/acs.chemrev.7b00664

Winsor, G.L., Griffiths, E.J., Lo, R., Dhillon, B.K., Shay, J.A., Brinkman, F.S.L., 2016. Enhanced annotations and features for comparing thousands of Pseudomonas genomes in the Pseudomonas genome database. Nucleic Acids Res 44, D646-53. https://doi.org/10.1093/nar/gkv1227

Xia, T., Kovochich, M., Liong, M., Mädler, L., Gilbert, B., Shi, H., Yeh, J.I., Zink, J.I., Nel, A.E., 2008. Comparison of the mechanism of toxicity of zinc oxide and cerium oxide nanoparticles based on dissolution and oxidative stress properties. ACS Nano 2, 2121–2134. https://doi.org/10.1021/nn800511k

Xiaoxiao, C., Xing, Z., Rui, L., Hanchao, Y., Zhisong, L., Xu, Y., 2012. Photosynthetic toxicity and oxidative damage induced by nano-Fe3O4 on Chlorella vulgaris in aquatic environment. Open J Ecol 2012.

Xie, N., Zhang, L., Gao, W., Huang, C., Huber, P.E., Zhou, X., Li, C., Shen, G., Zou, B., 2020. NAD+ metabolism: pathophysiologic mechanisms and therapeutic potential. Signal Transduct Target Ther 5, 227. https://doi.org/10.1038/s41392-020-00311-7

Yan, Y., Wang, W., Wu, M., Jetten, M.S.M., Guo, J., Ma, J., Wang, H., Dai, X., Wang, Y., 2020. Transcriptomics Uncovers the Response of Anammox Bacteria to Dissolved

Oxygen Inhibition and the Subsequent Recovery Mechanism. Environ Sci Technol 54, 14674–14685. https://doi.org/10.1021/acs.est.0c02842

Yeap, Cheryl S.Y., Nguyen, N.H.A., Blifernez-Klassen, O., Mussgnug, J.H., Busche, T., Kruse, O., Sevcu, A., 2022. Phenotypic Responses of Green alga Chlamydomonas reinhardtii to nanoscale zero valent iron, in: NANOCON Conference Proceedings - International Conference on Nanomaterials. TANGER Ltd., pp. 236–241. https://doi.org/10.37904/nanocon.2022.4614

Yeap, Cheryl S.Y., Nguyen, N.H.A., Blifernez-KLASSEN, O., Mussgnug, J.H., Busche, T., Kruse, O., Sevcu, A., 2021. RNA extraction from soil bacterium pseudomonas putida and green alga Raphidocelis subcapitata after exposure to nanoscale zero valent iron. NANOCON Conference Proceedings - International Conference on Nanomaterials 2021-October, 477–482. https://doi.org/10.37904/NANOCON.2020.3764

Yeap, Cheryl S.Y., Nguyen, N.H.A., Spanek, R., Too, C.C., Benes, V., Provaznik, J., Cernik, M., Sevcu, A., 2022. Dissolved iron released from nanoscale zero-valent iron (nZVI) activates the defense system in bacterium Pseudomonas putida, leading to high tolerance to oxidative stress. J Hazard Mater 439, 129627. https://doi.org/https://doi.org/10.1016/j.jhazmat.2022.129627

Yeo, M.-K., Pak, S.-W., 2008. Exposing zebrafish to silver nanoparticles during caudal fin regeneration disrupts caudal fin growth and p53 signaling. Mol Cell Toxicol 4, 311–317.

Yeon Kim, J., Park, H.-J., Lee, C., Nelson, K.L., Sedlak, D.L., Yoon, J., 2010. Inactivation of Escherichia coli by Nanoparticulate Zerovalent Iron and Ferrous Ion. Appl Environ Microbiol 76, 7668–7670. https://doi.org/10.1128/AEM.01009-10

Yousefzadeh, M., Henpita, C., Vyas, R., Soto-Palma, C., Robbins, P., Niedernhofer, L., 2021. DNA damage—how and why we age? Elife 10, e62852. https://doi.org/10.7554/eLife.62852

Yuan, Y., Wei, X., Yin, H., Zhu, M., Luo, H., Dang, Z., 2022. Synergistic removal of Cr(VI) by S-nZVI and organic acids: The enhanced electron selectivity and pH-dependent promotion mechanisms. J Hazard Mater 423, 127240. https://doi.org/10.1016/J.JHAZMAT.2021.127240

Zhang, F., He, M., Zhang, C., Lin, D., Zhang, J., 2021. Combined toxic effects of dioxin-like PCB77 with Fe-based nanoparticles in earthworm Eisenia fetida. Science of The Total Environment 766, 144347. https://doi.org/https://doi.org/10.1016/j.scitotenv.2020.144347

Zhang, L., Manthiram, A., 1997. Chains composed of nanosize metal particles and identifying the factors driving their formation. Appl Phys Lett 70, 2469–2471. https://doi.org/10.1063/1.118859

Zhang, W., M. C. Lo, I., Hu, L., Pao Voon, C., Leong Lim, B., K. Versaw, W., 2018. Environmental Risks of Nano Zerovalent Iron for Arsenate Remediation: Impacts on Cytosolic Levels of Inorganic Phosphate and MgATP2– in Arabidopsis thaliana. Environmental Science & Technology 52, 4385–4392. https://doi.org/10.1021/acs.est.7b06697

Zhao, X., Chen, B., Wu, L., Zhao, G., 2022. Role of mitochondria in nuclear DNA damage response. Genome Instab Dis 3, 285–294. https://doi.org/10.1007/s42764-022-00088-9

Zheng, M., Lu, J., Zhao, D., 2018. Toxicity and Transcriptome Sequencing (RNA-seq) Analyses of Adult Zebrafish in Response to Exposure Carboxymethyl Cellulose Stabilized Iron Sulfide Nanoparticles. Sci Rep 8, 8083. https://doi.org/10.1038/s41598-018-26499-x